Title

Lumped Macroelement Modeling of Earth-Retaining Structures under Seismic Loading for Nonlinear Time-History Analyses

Author

Dasmeh, Arastoo

Publication Date

2019

Peer reviewed|Thesis/dissertation

UNIVERSITY OF CALIFORNIA

Los Angeles

Lumped Macroelement Modeling of Earth-Retaining Structures under Seismic Loading for Nonlinear Time-History Analyses

A dissertation submitted in partial satisfaction

of the requirements for the degree

Doctor of Philosophy in Civil and Environmental Engineering

by

Arastoo Dasmeh

2019

ABSTRACT OF THE DISSERTATION

Lumped Macroelement Modeling of Earth-Retaining Structures under Seismic Loading for Nonlinear Time-History Analyses

by

Arastoo Dasmeh
Doctor of Philosophy in Civil and Environmental Engineering
University of California, Los Angeles, 2019
Professor Ertugrul Taciroglu, Chair

This dissertation addresses various engineering problems involving the seismic response modeling of earth-retaining structures. These are namely, (*i*) lateral passive seismic behavior of ordinary skew-angled bridge abutments, (*ii*) lateral passive seismic behavior of high-speed rail transition abutments (with no skew), and finally (*iii*) active and passive seismic behavior of (cantilevered) earth-retaining walls. The approach adopted for each problems is the same, which is to devise a macroelement model with physics-based parameters (e.g., soil density, shear strength, wall height, etc.) that captures salient response features. These models are able to predict the lateral capacity of the retained soil and residual displacements with a modest computational effort—as compared to, for example, predictive simulations carried out with three-dimensional finite element models—, which renders them to be amenable for repeated nonlinear time-history analyses required for performance-based seismic assessment and design. The three aforementioned problems are briefly described below:

I. Presence of skew-angled abutments complicates the seismic behavior of ordinary bridges, primary driver of which is the passive lateral resistance of the engineered backfill behind the abutment. The eccentricity of the soil reaction relative to the bridge's center of stiffness or mass causes a skew bridge to rotate under seismic excitations, and a nonuniform soil pressure distribution develops behind the abutment backwall. A distributed nonlinear spring model is devised here to represent the lateral passive reaction of the backfill soil. To that end, a mod-

ification factor is devised so that Log-Spiral Hyperbolic (LSH) backbone curves –which had been developed in prior research and were validated for backfills of straight abutment–can be used to generate the backbone curves of the said springs. This new modeling approach is verified against three-dimensional finite element model simulations and is validated with data from large-scale experiments conducted at Brigham Young University that had produced direct measurements of load-deformation backbone curves for several skew angles. In the final step, the validated modified-LSH model is used in parametric studies to devise a simple bilinear load-deformation relationship that is parameterized with respect to the backwall height, abutment skew angle, and the backfill soil properties. This simple relationship is intended for routine use in the capacity-based seismic design and analysis of skew bridges.

II. California's High-Speed Rail (HSR) System is slated to traverse nearly the entire length of the state, and thus it will be exposed seismic risks from almost every known major tectonic fault there. The present study deals with the seismic responses of bridge-abutment transition backfills (BATBs), which are essential components of HSR bridges. BATBs provide a gradual variation of vertical stiffness between the bridge deck and the engineered backfill zone, enabling smooth operations for trains traveling at high speeds. All prior investigations focused on this vertical stiffness in order to better characterize the localized vertical differential movements around BATBs under periodic high axial loads from train sets. Lateral behavior of BATBs, which are important under seismic loads, have not been previously investigated. The present study offers a parametric nonlinear lateral force-displacement backbone curve for BATBs that is verified against three-dimensional finite element models and validated against data from large-scale tests conducted at Brigham Young University. The parametric curve takes backwall height as well as abutment skew angle into account.

III. Performance-based seismic assessment (PBSA) of earth retaining structures requires the use of accurate yet computationally efficient analysis models. To date, limit equilibrium models offered the most computationally efficient results, but they only produce estimates of peak lateral seismic forces and cannot be used in nonlinear time-history analyses. While detailed finite element models can possibly fill this need, they are not amenable for repeated

simulations required for quantifying the uncertainties associated with estimated ground motions within the PBSA framework. A novel Lumped Impedance Model (LIM) is developed in this study that generates as accurate solutions as detailed FE models, with trivial computational effort. The model is able to also reproduce lateral passive load-deformation backbone curves as predicted by a state-of-the art limit equilibrium model, by its design. The computational saving offered by LIM is due to lumping of mass and stiffness of the retained soil, and the strategic placement of elastoplastic macroelements along pre-calculated active and passive failure hyperplanes. LIM is verified against analytical solutions in frequency-domain for linear response regimes—wherein it is shown that LIM can accurately capture the frequency-dependent responses of the retained soil—as well as other previous studies for inelastic conditions. LIM is also verified against detailed FEM simulations of cantilevered retaining wall subjected to both narrow- and broadband excitations, and it is shown that both elastic and inelastic responses of the retained soil (including residual wall displacements and rotations) are adequately captured. Finally, a framework for PBSA of earth-retaining structures using LIM as the predictive model is proposed and its use is demonstrated through an example seismic assessment application wherein a fragility curve is computed.

The dissertation of Arastoo Dasmeh is approved.

Joseph M Teran

Jian Zhang

Scott Joseph Brandenberg

Ertugrul Taciroglu, Committee Chair

University of California, Los Angeles

2019

TABLE OF CONTENTS

LIST OF FIGURES

LIST OF TABLES

CHAPTER 1

A Validated Lateral Passive Capacity Model for Skew-Angled Seat-Type Ordinary Highway Bridge Abutments

1.1 Introduction

State-of-the-art in previous modeling of the passive lateral response of highway bridge abutments can be traced back to the original work by Shamsabadi and co-workers [Shamsabadi et al., 2007] who utilized an assumed Log-Spiral Rankine failure surface endowed with a modified stress-strain backbone curve, which was a modified version of the model by Duncan and Chang [Duncan and Chang, 1970]. A method of slices was then used for estimating the passive capacity of the backfill using soil strength parameters along with soil cohesion and interface friction angle of the wall-soil interface, which then produced lateral load-displacement data pairs. The model was dubbed as the "Log-Spiral (denoting the dominant shape of the soil failure surface) Hyperbolic (denoting the shape of the stress-strain curve)" or simply the LSH model by the authors. This work was later extended in [Shamsabadi et al., 2010] wherein two Hyperbolic Force-Displacement (HFD) backbone curves were devised—one each for typical granular and cohesive backfill soil types—using the LSH model predictions wherein the wall height was considered as an explicit parameter in the provided formula. More recently, Khalili-Tehrani and co-workers [Khalili-Tehrani et al., 2016] further extended this approach to a Generalized HFD (GHFD) model, which was parameterized using soil strength and cohesion as well as wall height, so that it could be used for broader range backfill characteristics rather then only two.

All of the aforementioned models were extensively verified and validated against both centrifuge and large-scale field test data. While useful, these prior models are confined to predicting the behavior of straight abutments. However, bridges with skew-angled abutments are very common worldwide. Indeed, data from the US National Bridge Inventory indicates, for example, that more than half of California's nearly 25,000 bridges have skewed abutments, with angles occasionally reaching above 60 degrees [Nojoumi, 2016, NBI, 2018]

Post-event reconnaissance reports form recent earthquakes indicate that the in-plane rotation and subsequent unseating of the superstructure is the primary mode of damage for this bridge type [Yashinsky et al., 2010, Kawashima et al., 2011]. The superstructure of a skewed bridge tends to rotate away from the acute corner of the abutment due to the eccentricity of its abutment's passive lateral response relative to its the center of stiffness in the horizontal plane.

As part of a pooled-fund seismic safety research program supported by the Federal Highway Administration (FHWA) and various state departments of transportation, four large-scale tests were carried out at Brigham Young University (BYU) to investigate the passive lateral behavior of skewed abutments. The specimens had skew angles of 0, 15, 30 and 45 degrees and had identical and typical densely compacted backfills. The measurements indicated that the lateral force-deformation backbone relationship has a near-hyperbolic shape, which is similar to what is observed for non-skew abutments [Shamsabadi et al., 2007, Shamsabadi et al., 2010]. However, there were significant reductions in both lateral stiffness and capacity. Specifically, the measurements suggested that the entire backbone curve scales down with increasing skew angle.

The purpose of the present effort is then to develop an appropriate model to represent the lateral passive behavior of skew abutments using the LSH model (for a straight abutment) as a basis. This model is then verified against prediction made with detailed three-dimensional continuum finite element simulations validated against BYU's large-scale tests. The validated backbone curves are ultimately packaged in the form of a fiber-based model (here distributed nonlinear springs), which enables the analysis of backwalls that both rotate and translate under seismic motions. The resulting model is simply referred as the Skew LSH

(or SLSH) model henceforth.

1.2 Seismic Behavior of a Bridge with Skew-Angled Abutments

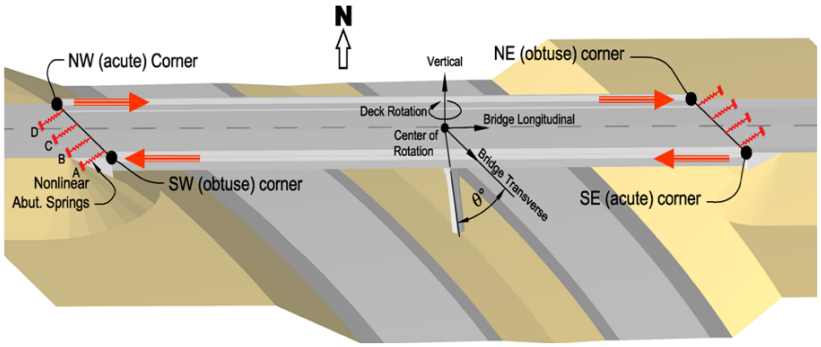

Figure 1.1: Deck rotation during a seismic Event [Shamsabadi and Rollins, 2014].

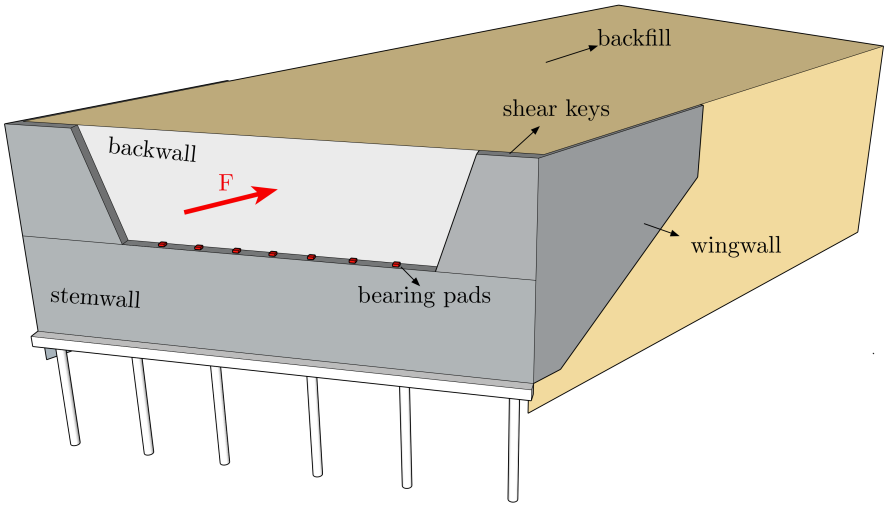

Figure 1.2: Plunging action of seat-type abutment system during a seismic event.

During a seismic event, the superstructure of a skew bridge will experience longitudinal and transverse displacement as well as significant in-plane rotations about its vertical axis, as shown in Figure 1.1.

As a result the bridge deck "collides" with the abutment backwall-backfill system. The

backwall is one of the main bridge sacrificial elements that is typically designed to disengage during a seismic event in order to limit seismic forces transferred to the abutment foundation which is capacity protected elements within the bridge system. The collision continues for some time and then the rotation of the deck ensues about the centroid of the bridge superstructure which can result in the separation of the deck at the acute corner of the abutment.

As a result of deck rotation, the abutment backwalls tend to be pushed primarily in the obtuse corners of the deck, causing asymmetric passive wedges to form behind the abutment backwall. In skewed abutments, the eccentric loading of the abutment backwall can result in a reduced mobilized soil passive capacity as compared to ordinary non-skewed abutments. The ground heave at the far half of the backwall width in Figure 1.2 illustrates the formation of the asymmetric passive wedge across the backwall resulting in a reduction of soil resistance normal to the abutment backwall. For very high skew angles, the passive capacity can significantly drop. This is a result of separation of the superstructure at the acute corners and disintegration of the passive wedge after significant plastic ground deformation and heave has occurred only near the obtuse corners of the deck. These findings raise the possibility that due to unavoidable rotation, a skew abutment may develop a considerably reduced soil resistance in comparison to a non-skewed abutment, affecting overall bridge response.

1.3 Definitions

Prior to describing the model, it is important to establish the definitions of various quantities and terms that will appears throughout this Chapter, and elsewhere in this dissertation. It's particularly important for the reader to distinguish between the passive force from the total force and transverse shear force mobilized behind the backwall. Also, realizing the differences between different displacement-rotation scenarios is crucial, and it will be discussed later how the SLSH model treats them differently.

The distribution of forces at the interface between a skewed bridge and the adjacent backfill soil is illustrated in 1.3 [Burke, 1994]. The longitudinal force F can be induced

by thermal expansion or seismic forces. For static or simplified pseudo-static analyses, the components of the longitudinal force normal and transverse to the abutment must be resisted by the passive force F_N normal to the abutment backwall and the shear resistance F_T on the backwall.

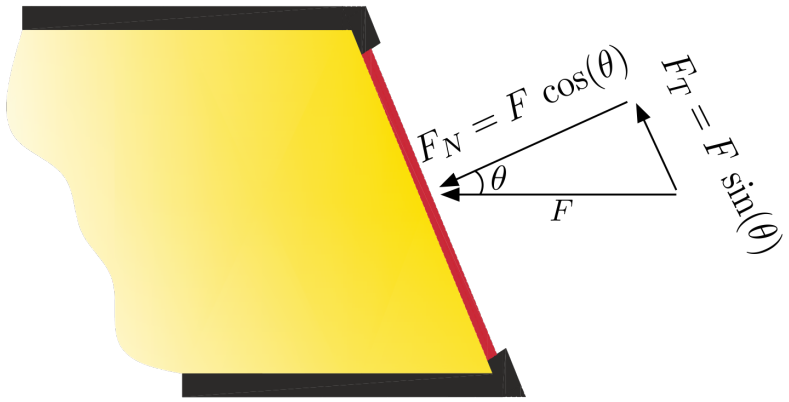

Figure 1.3: Longitudinal component F_N resisted by passive force and transverse component F_T resisted by shear resistance

As it will be discussed later, rotation adds more complexity to this problem, therefore the problem of skew abutments is categorized into two subcategories based on the presence/absence of the rotation. The simpler case happens when the rotation degree of freedom is fixed, henceforth called the pure/straight push. Any rotating wall scenarios fall into displacement-rotation push category which is divided to displacement-rotation. In this study we just consider the case that the rotation increases linearly with displacement.

1.4 Log-Spiral Hyperbolic Model for a Straight Abutment

The Skew Log-Spiral Hyperbolic model presented in this chapter is essentially an extension of LSH model [Shamsabadi et al., 2007] that incorporates effects of skew. The LSH model employs a limit equilibrium approach, and by assuming log-spiral failure surfaces and using modified hyperbolic soil stress-strain behavior, predicts the mobilized passive force behind the backwall due to normal displacement.

[Shamsabadi et al., 2007] also calibrated a hyperbolic force-displacement (HFD) equation that replicates results of LSH model for abutments with 1.67 m height with engineered backfill using experimental data. [Shamsabadi et al., 2017] proposed a generalized HFD to estimate nonlinear abutment-backfill force-displacement relationship as shown in equations 1.1 to 1.7.

$$F(y) = \frac{Cy}{1 + Dy}, \text{ where} \tag{1.1}$$

$$\tag{1.2}$$

$$C = 2K_{50} - \frac{F_{ult}}{y_{\max}} \tag{1.3}$$

$$\tag{1.4}$$

$$D = 2\left(\frac{K_{50}}{F_{ult}} - \frac{1}{y_{\max}}\right) \tag{1.5}$$

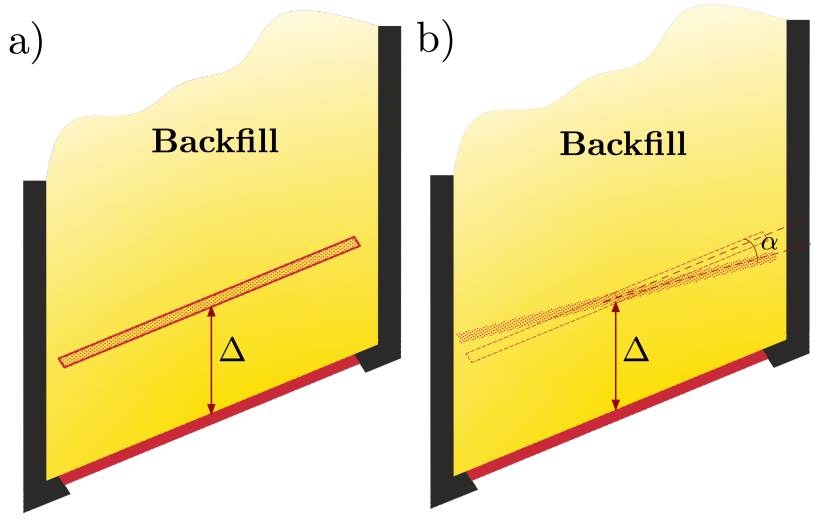

Figure 1.4: a) pure/straight push, b) displacement-rotation push

$$F_{ult} = \frac{\beta H^{2.5}}{1 + \zeta H} \tag{1.6}$$

$$K_{50} = \psi H + \mu \tag{1.7}$$

where $y_{\max} = 0.05H$ and β, $\zeta, > \psi$ and μ are constant coefficients that are listed in table 1.1 for US customary units and metric units.

Table 1.1: Constants and units in US Customary and Metric systems

Contant	**US Customary Units**	**Metric Units**
β	5.5	1565.6
ζ	2.09	6.86
ψ	5.5	10372
μ	20	11496
Parameter	**US Customary Units**	**Metric Units**
$\mathbf{F}$, $\mathbf{F}_{ult}$	kip/ft	kN/m
$\mathbf{K}_{50}$	kip/inch/ft	kN/m/m
H	ft	m
y, $\mathbf{y}_{\max}$	inch	m

1.5 Finite Element Simulations

We use nonlinear 3D finite element model (Plaxis 3D) to Figure verify our SLSH model. FEM model has been calibrated against full-scale non-skew abutment experiment carried out by researchers at UCLA as part of seismic safety research fund supported by Caltrans [Shamsabadi et al., 2007]. The objective of the experiment was to extract force-displacement data for an abutment with 4.6 m width and 1.67 m height with a granular backfill with 95% compaction ratio. The backfill retained within two wingwalls and interior surfaces had been covered with plastic sheets to minimize the soil-wingwall interface friction. The backwall was pushed horizontally between two wingwalls without any vertical movement and rotation.

We employed hardening soil model to simulate UCLA full-scale abutment backwall test in Plaxis 3D. This model is an extension of the hyperbolic model originally proposed by

Duncan and Cheng (1970). Among the unique capabilities of this soil model, one might mention featuring a yield cap and soil dilatancy effects.

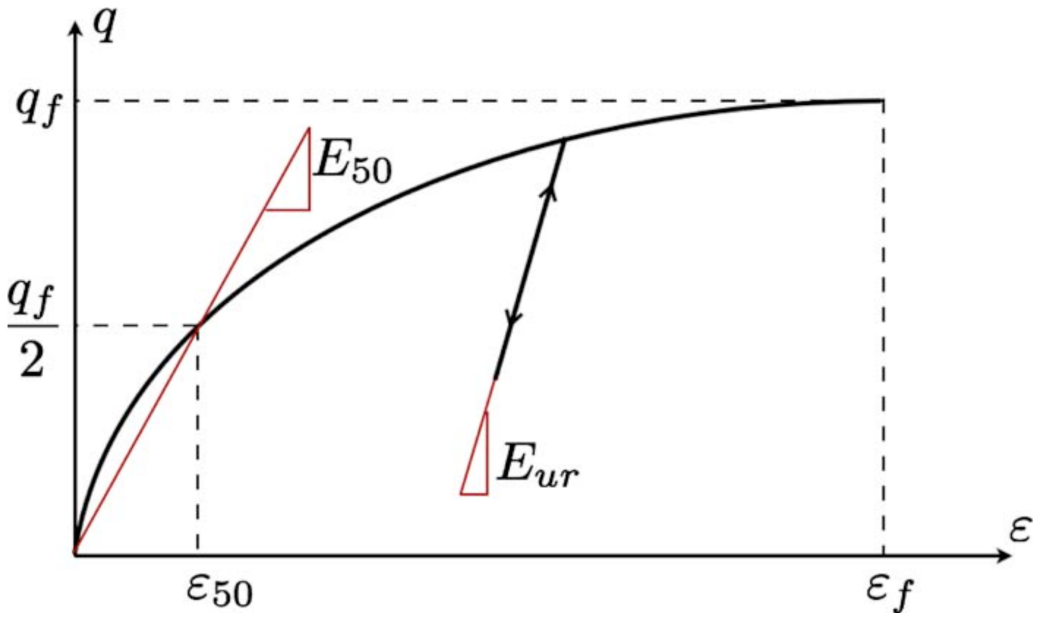

Figure 1.5: Abutment-backfill stress strain model [Shamsabadi et al., 2007].

The hyperbolic shape of the stress-strain curve is depicted in Figure 1.5. R_f denotes the ratio of the stress at failure q_f and the asymptote of the curve q_u. ϕ stands for soil friction angle and R_{int} is ratio of the tangent of interface friction angle ($\tan(\delta)$) over soil internal friction angle $\tan(\phi)$. The loading stiffness is denoted by E_{50} and the unloading stiffness is denoted by E_{ur}. Dialating angle is chosen to be $\psi = \phi - 30$ per recommendation of [Vermeer and Brinkgreve, 1998]. Results of Plaxis 3D is plotted against the UCLA test data in Figure 1.6.

Table 1.2: Soil properties used for simulation of UCLA and BYU test in Plaxis.

Test	**Unit Weight** γ (KN/m^3)	**Friction Angle** ϕ	**Cohesion** c	**Wall Friction** δ (deg)	**Elasticity** E_{50} (kPa)	**Unloading Elasticity** E_{ur} (kPa)	**Failure Ratio** R_f	**Poisson's Ratio** ν
UCLA	20	40	14	20	6e4	1.3e5	0.97	0.3
BYU	20	41	8	31	6e4	1.3e5	0.97	0.3

Following our calibrated FE simulations against UCLA test data, we created a set of skew-abutment simulations by modifying our simulation to match material properties and

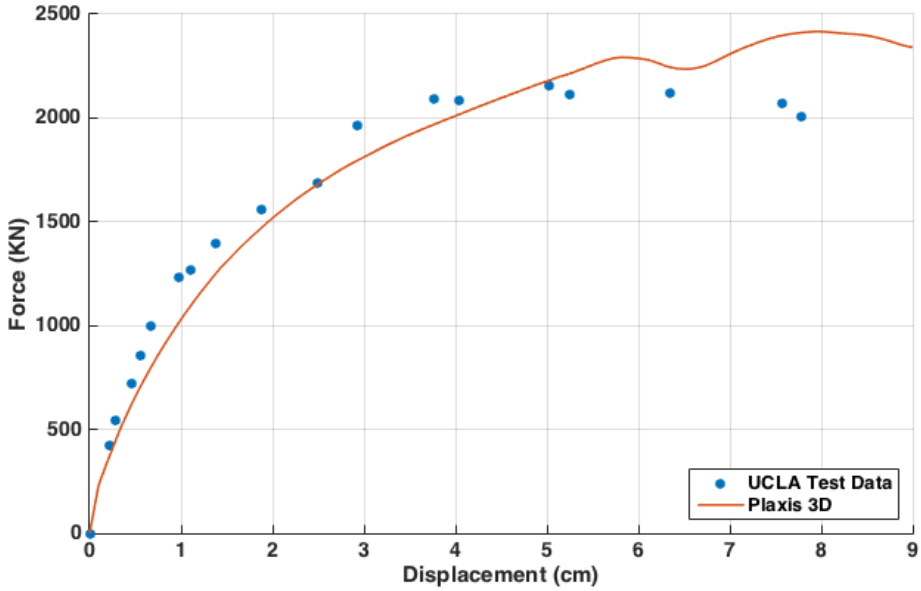

Figure 1.6: Validation of Plaxis 3D simulations agains UCLA test data.

backwall geometry of the BYU test. The material property used in our simulations are listed in table 1.2 ([Marsh, 2013]). Backwall dimensions are listed in table 1.3. We also simulated a 60^o skew abutment with the same material properties and same bridge deck width (3.35 meters). Force per unit width of these skew abutments had been calculated Plaxis 3D FE simulations and are plotted against the displacement in Figure 1.7.

Table 1.3: Backwall width in BYU and UCLA full scale experiments.

Test	**Backwall Width (m)**
BYU 0-skew	3.3
BYU 15-skew	3.5
BYU 30-skew	3.9
BYU 45-skew	4.7
UCLA 0-skew	4.6

An important result of these simulations the exponential decay of the ultimate passive force with respect the to skew angle. Figure 1.8 shows the normalized ultimate passive force. We performed a regression optimization to fit a function of the form $R = e^{-a\theta}$. Figure The 95% confidence intervals is $a = [0.014, 0.022]$. We have plotted the 95% confidence interval internal for the reduction factor in Figure 1.8. The reduction factor proposed by

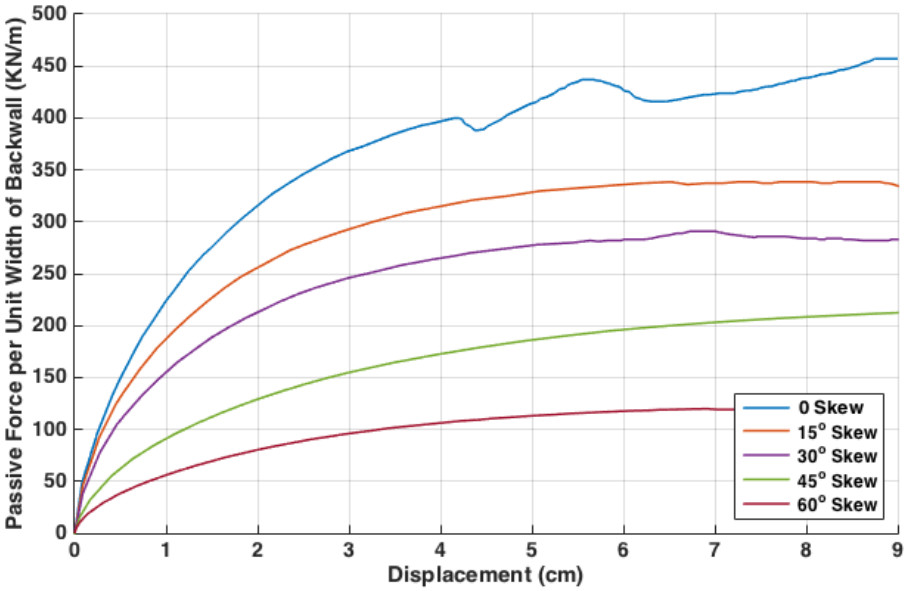

Figure 1.7: Passive force-displacement curves for per unit width of the wall obtained for straight and 15, 30, 45 and 60 degrees skew abutments.

[Shamsabadi and Rollins, 2014] $R = e^{-\theta/45}$ is sandwiched between boundaries of this interval . We conclude that the proposed reduction factor is a legitimate factor and we construct our SLSH model based on it.

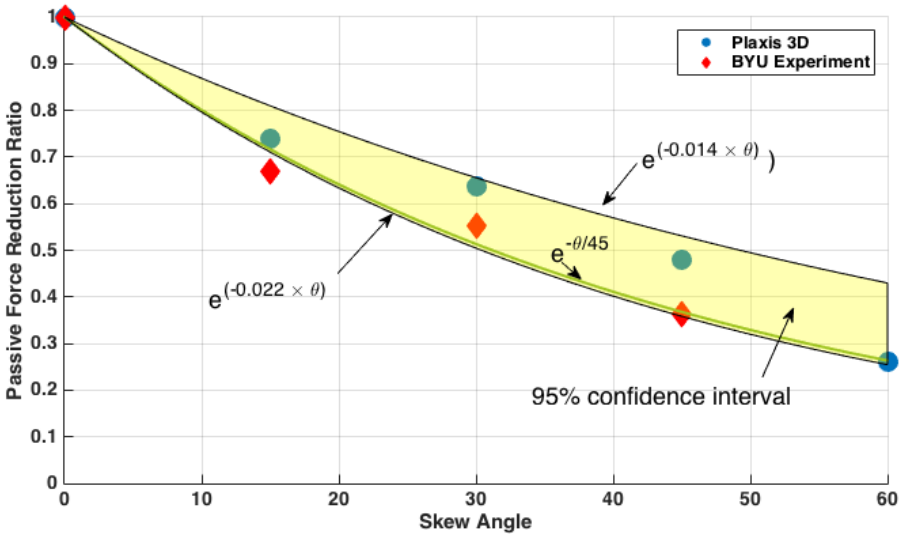

Figure 1.8: Reduction ratio of the passive force.

Figure 1.9 shows a verification for the exponential reduction factor R. The backwall width

in 45^o-skew abutment test at BYU is 4.72 m wide. Although, the backwall in the UCLA test is 4.57 m wide, the assumption that backwall in both test have same length is acceptable due to slight extension of the embankment by sides of the backwall. Furthermore, as shown in table 1.2 the backfill material in UCLA and BYU are relatively similar. Therefore, as shown in Figure 1.9 reducing the force-displacement curve governing the UCLA test by factor of $R = e^{-\theta/45}$ reproduces the that of the 45^o-skew BYU test.

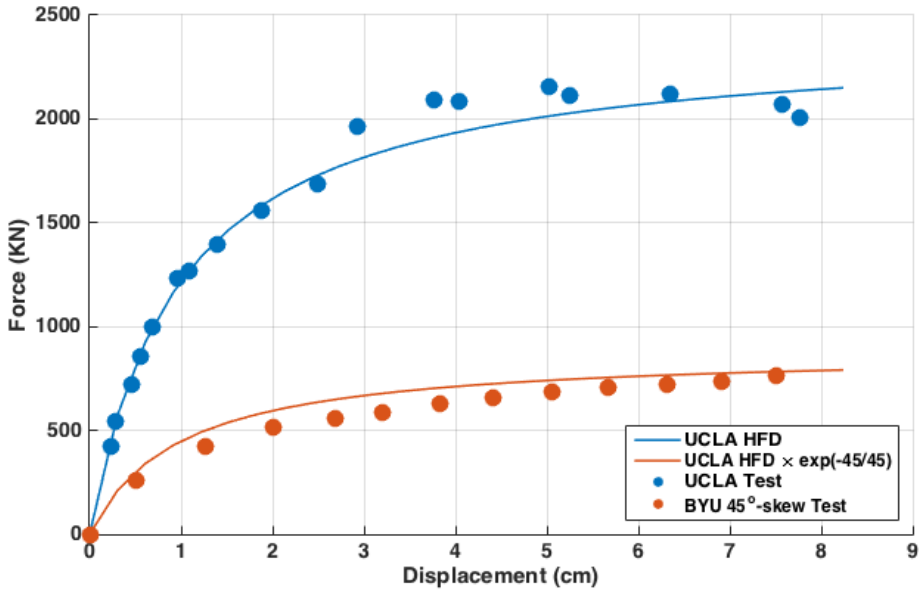

Figure 1.9: non-skew (UCLA) and 45^o-skew (BYU) 15.5 ft backwall with engineered backfill.

1.6 Skew LSH Model

In the analysis of the backfill-backwall interaction problem under backwall horizontal displacement and rotation, the behavior of abutment backfill, especially undergoing asymmetric horizontal displacement, is one of the most important phenomena, which needs to be well understood. The magnitude of the mobilized strength of the backfill material can be related to the magnitude of shear strain within the backfill. The mobilized shear strength and shear strains varies across the backwall as a function of backwall displacements and rotations.

A common method of analyzing abutment response to applied lateral load is through

finite element modeling of the backfill-backwall system using a series of uniform nonlinear spring elements along the width of the backwall to model the lateral backfill reaction. Current design practices model the behavior of these spring elements using predefined lumped Hyperbolic Force Displacement (HFD) curves that provide a relationship between the backfill reaction and lateral backwall displacement. However, HFD curves have been developed based experimental and analytical studies for non-skewed abutments. The lumped HFD curves do not consider variation of nonlinear backfill springs as a function of deck rotation and displacements.

[Sandford and Elgaaly, 1993] mounted pressure cells on a 20 degree skewed monolithic abutment backwall to measure the effects of the skew angle on the soil pressure distribution on the backwall due to deck rotation caused by thermal expansion for a period of 33 months. The deck rotation resulted in larger stress and strain at the obtuse corner than at the acute corner. Hence the greater movement at the obtuse corner caused significant pressure and permanent deformation on the backfill at the obtuse corner than on the acute corner. They recommended trapezoidal pressure distribution equivalent to Rankine passive earth pressure at the obtuse corner and Rankine active earth pressure at acute corner of the abutment shall be used for the design of the abutment (figure 1.10(b)).

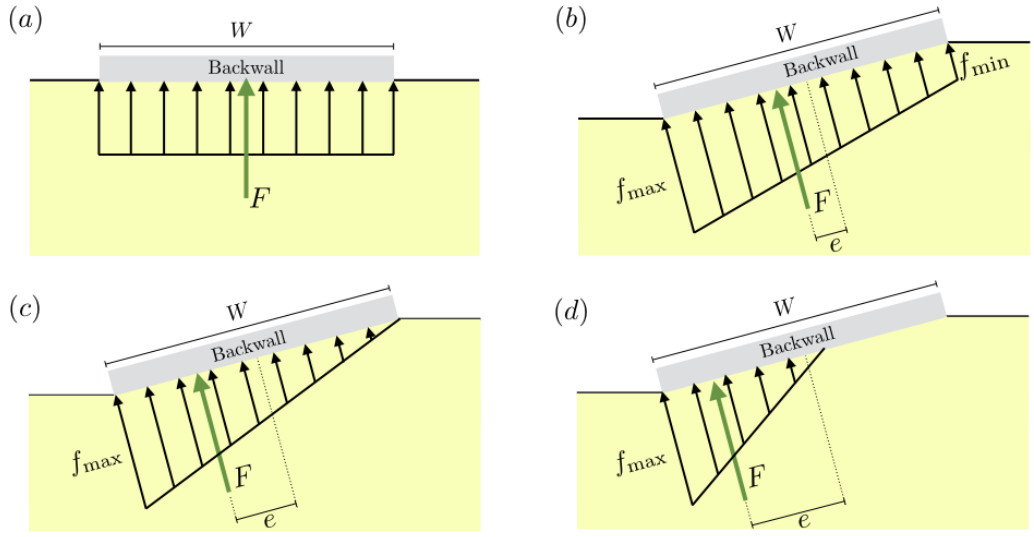

Figure 1.10: Abutment backfill pressure distribution (a) $e = 0$, (b) $e < \frac{w}{6}$, (c) $e = \frac{w}{6}$, (d) $e > \frac{w}{6}$.

In SLSH model, soil domain is assumed to be limited within wingwalls. Therefore, in our verification FE simulations, we modeled the backfill with no side embankment. As it will be discussed later in SLSH verification section, the side embankment may have significant contribution in total mobilized passive force behind the backwall. To account for this contribution we calibrate the SLSH model with a factor, henceforth called 3D-factor [Ovesen and Stromann, 1972].

In spite of the simplicity of this pushing scenario, it is really important to investigate the behavior of the skew abutments under it since it forms the basis of the SLSH model for other pushing scenarios. In fact, the SLSH is based on developing fiber backbone curves based on straight push scenario, and modifying them for other displacement-rotation scenarios and finally adding up the fiber forces to obtain passive force for the whole backwall.

Developing fiber backbone curves requires knowledge of the total passive force mobilized behind the backwall and the way the force is distributed. Using the reduction factor R proposed by the [Shamsabadi and Rollins, 2014], one can obtain force behind the skew-abutment (F_θ) using equations 1.8 and 1.9:

$$R(\theta) = e^{-\theta/45} \tag{1.8}$$

$$F_\theta = R(\theta) \times F_o \tag{1.9}$$

For a given displacement, one can read total passive force F from backbone curve extracted in equations 1.8 and 1.9. Assuming a trapezoidal distribution (figure 1.10) of pressure behind the backwall, given total force and eccentricity, using geometric properties of trape-

zoid one can obtain equivalent fiber backbone curves as below:

$$f_{max} = \frac{F}{W}\left(\frac{6e}{W} + 1\right) \tag{1.10}$$

$$f_{min} = \frac{2F}{W} - f_{max} \tag{1.11}$$

$$f_i = \frac{f_{max} - f_{min}}{W}\left(x_i + \frac{W}{2}\right) + f_{min} \tag{1.12}$$

$$F_i = f_i \times W_i \tag{1.13}$$

where f_i, F_i and F stand for average force per unit width of fiber i, total force behind fiber i and total force behind the backwall, respectively. W is width of the backwall while W_i is width of ith fiber. Figure 1.11 schematically explains the concept of fiber backbone curves under straight push scenario. Figure **??** proves accuracy of our SLSH model comparing that with Plaxis 3D FE simulation under straight push scenario.

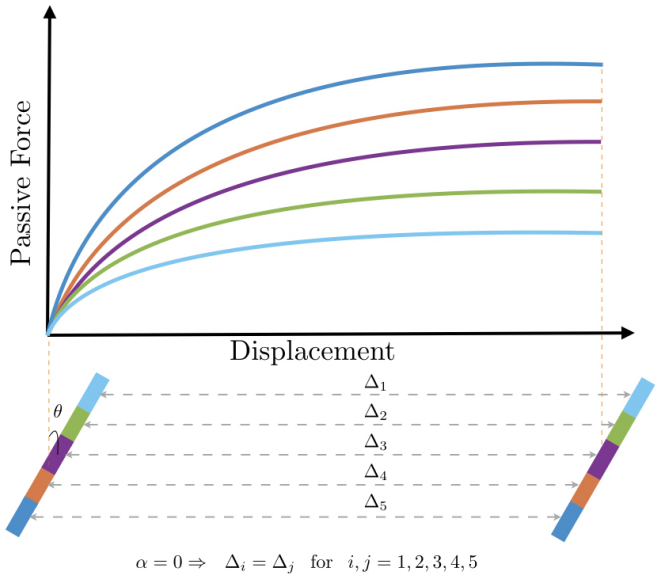

Figure 1.11: Fiber backbone curves for the straight push scenario.

The reduction factor proposed by [Shamsabadi and Rollins, 2014] can be incorporated in the hyperbolic equation 1.1 for estimating the mobilized passive force behind θ-skew abutment under a pure push scenario. In other words, For purpose of a pure push, one can expedite calculations by replacing the LSH algorithm with the simplified hyperbolic equation 1.14. Figure 1.12 shows the verification of LSH and extended hyperbolic equation against

Plaxis 3D simulations.

$$F(y) = \frac{Cy}{1 + Dy} e^{-\theta/45} \tag{1.14}$$

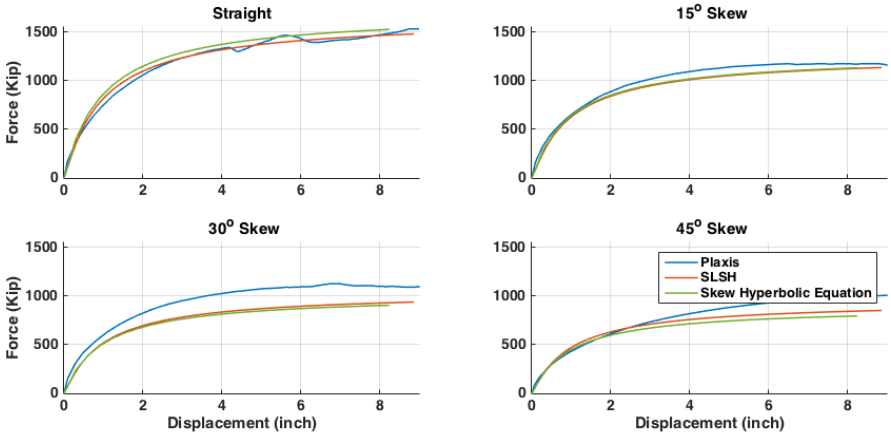

Figure 1.12: Verification of SLSH and skew hyperbolic equation against Plaxis 3D simulation results for the straight push scenario.

Fiber backbone curves developed for the straight push scenario will be modified based on the displacement that each fiber experiences during the pushing procedure. Since the rotation about any point can be explained in terms of a superposition of a displacement and a rotation about the center of the wall, we narrow our study down to scenarios involving rotations about the center.

Our FE simulations show a reduction of capacity in weaker fibers due to the rotation. The reduction of the force developed behind a fiber is proportional to the ratio of the fiber displacement at a displacement-rotation scenario over displacement at the pure push scenario to power n. The power n has been calibrated against FE simulations with reasonable match.

During a seismic event, the superstructure of a skew bridge will experience longitudinal and transverse displacement as well as significant in-plane rotations about its vertical axis, as shown in Figure 1.

We assume that the rotated skew abutment reaches to its ultimate passive capacity

when the middle fiber is displaced by the maximum displacement of the straight push case, roughly $\Delta_{ult} = 0.05H$. At this ultimate condition, rest of fibers either exceed the ultimate displacement Δ_{ult} or never reach to the ultimate displacement. For those fibers that their maximum displacement $\max(\Delta_i)$ are larger than Δ_{ult}, tail of corresponding backbone curve extends by a straight line since they already reached their maximum capacity. However, for those the $\max(\Delta_i)$ is less than Δ_{ult}, corresponding backbone curve is cut at the $\max(\Delta_i)$. Furthermore, the stiffness of of these fibers should be reduced by ratio of $\max(\Delta_i)$ over Δ_{ult}. Figure 1.13 describes the method and concisely it can be formulated as below.

$$\begin{cases} \max(F_i) = \max(F_i)_{st} & \max(\Delta_i) > \Delta_{ult} \\ F_i(\Delta) = (\frac{\max(\Delta_i)}{\Delta_{ult}})^{0.2} F_{i_{st}}(\Delta) & \max(\Delta_i) < \Delta_{ult} \end{cases}$$

where $\max(F_i)_{st}$ stands for maximum force of ith fiber under straight push condition and

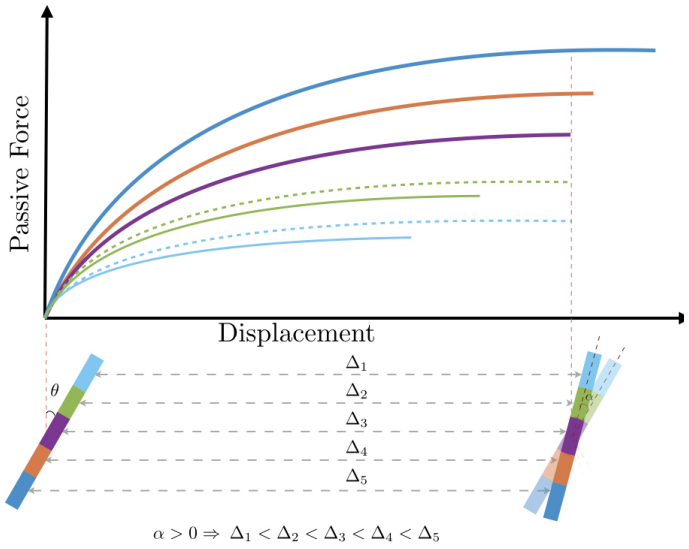

Figure 1.13: Fiber backbone curves for the combined displacement-rotation scenario.

$F_{i_{st}}(\Delta)$ is corresponding backbone curve under straight push condition. If at any point during loading, a fiber detaches from the soil, the effective width of the backwall should be reduced as shown in Figure 1.10. In other words, the force mobilized in the fiber is zero (equation 1.15). Figure 1.13 illustrates the mechanism of the SLSH in presence of rotation

and the flowchart in Figure 1.15 summarizes the method.

$$\Delta_i < 0 \;\; \Rightarrow F_i(\Delta_i) = 0 \tag{1.15}$$

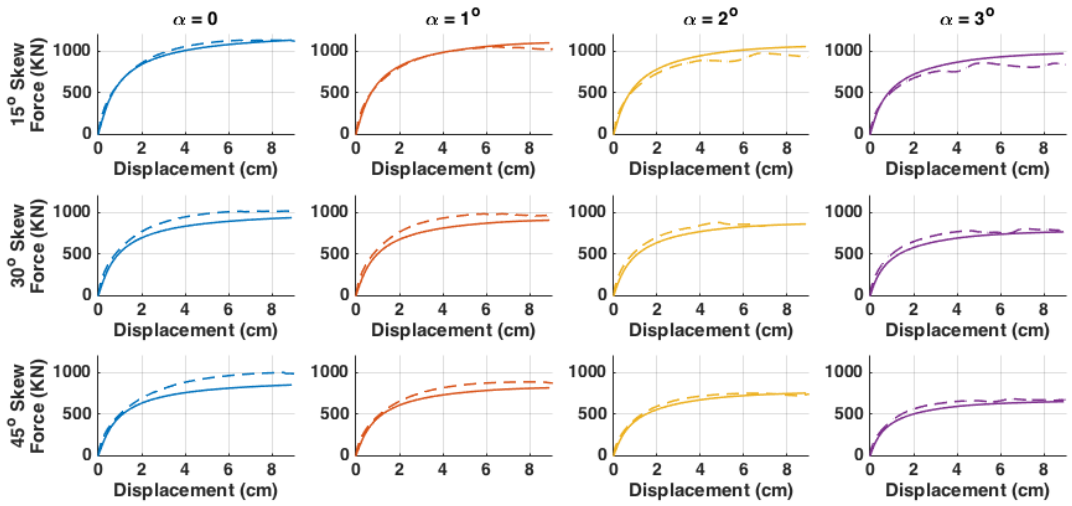

Figure 1.14: Verification of SLSH against Plaxis 3D simulations for displacement-rotation scenarios.

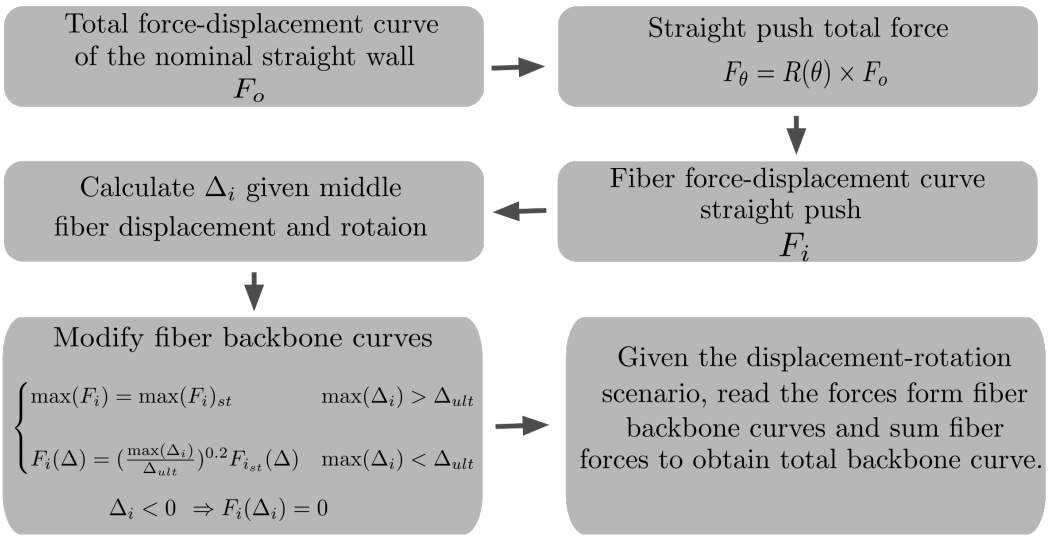

Figure 1.15: Fiber SLSH algorithm.

1.7 BYU Experiments and Model Validation

A series of full-scale static load tests were performed at BYU on an 3.35 m wide deck and 1.68 m tall skewed abutment with various angles as shown in Figure 1.17a (Marsh et al, 2013). The tests were designed to differentiate the nonlinear resistance of the bridge abutment for identical backfill but with four different skew angles namely, 0, 15, 30, and 45 degrees. The backfill materials for all tests were identical, and were compacted to approximately 96% of modified Proctor density per [ASTMD1557, 2012].

The inherent difference of UCLA full-scale experiment with the large scale experiment performed in BYU is the configuration of the backfill. The backfill soil is restrained between two plywood (figure 1.16a) and the interface of the plywoods and soil had been lubricated by placing in a plastic sheet to avoid contribution of lateral plywood walls in the total mobilized force. While in the BYU test the backfill is extended by 1.52 m from edges of the backwall (figure 1.17a). The extended embankment in BYU test contributes to the resistance against the longitudinal force imposed to the backwall. A 3D factor ([Shamsabadi et al., 2007], [Ovesen and Stromann, 1972]) has been applied to SLSH and Plaxis 3D to account for the contribution of embankment extended by the sides of the backwall.

Back calculated 3D-factors are shown on validation plots (figure 1.18). The reducing trend of 3D-factors as the skew grows implies the reduction of the contribution of the part of the backfill that is located on the opposite side of the skewness. Results of SLSH and HFD are presented in Figure 1.18.The minor difference of results in these figures can be translated to unideal soil model, uncertainty in soil properties measurement, unavoidable experimental imperfections and errors due to numerical approximations.

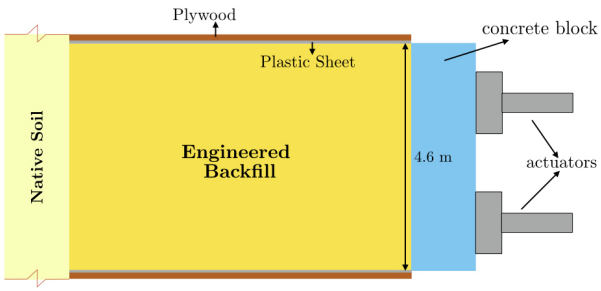

(a) Schematic representation of the UCLA full-scale abutment test configuration.

(b) Excavation of native soil to be substituted with the engineered backfill, UCLA experiment.

Figure 1.16: UCLA Experiment Configuration.

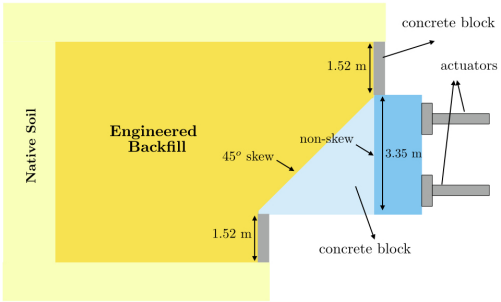

(a) Schematic representation of the BYU large-scale skew abutment test configuration.

(b) BYU large-scale skew abutment field test.

Figure 1.17: BYU Experiment Configuration.

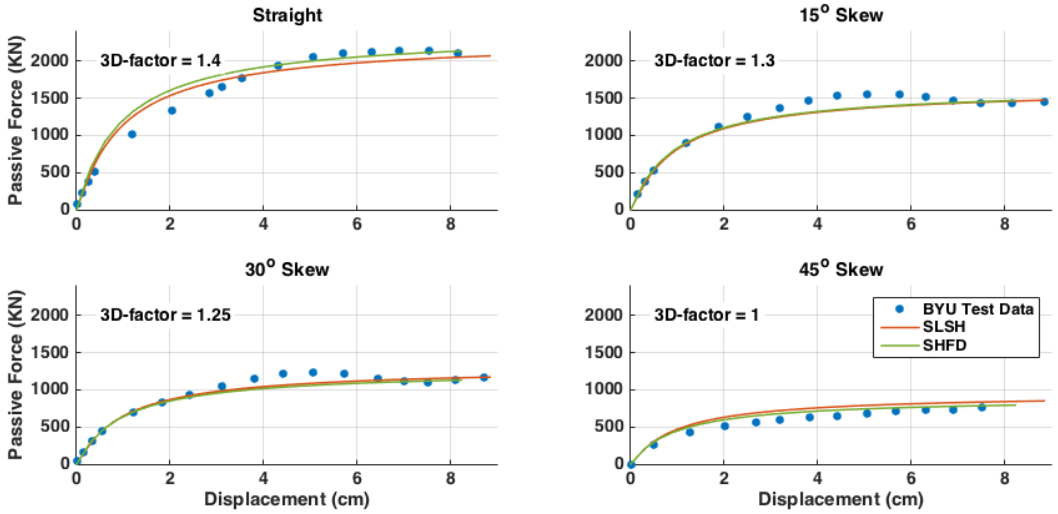

Figure 1.18: Validation of SLSH and skew hyperbolic force-displacement equations 1.14 against BYU experimental data.

1.8 Recommendations for Implementation of SLSH in a Seismic Design Code

Seismic Design Criteria [Caltrans, 2013] employs a simplified bilinear force-displacement relationship for design of non-skew abutment backwall. The bilinear force-displacement curve comprises an elastic segment with stiffness K and a horizontal segment representing equivalent bilinear ultimate passive capacity F_{bil}. To derive an equivalent bilinear model, assuming stiffness equals to K_{50} of the HFD model, F_{bin} is calibrated such that the mobilized potential energies behind the backwall have the minimum difference using two methods. In other words, the area below the HFD curve and the equivalent bilinear curve are equal.

The calibration process begins with assuming a general form for F_{bil} with unknown parameter ξ_{bil} (equation 1.16) which are later determined through an optimization. In this study, for a set of two hundred backwalls with heights varying from the potential energy is calculated using HFD. Then a nonlinear regression is performed to determine α. The regression analysis concluded that with 95% level of significance the value ξ_{bil} equals 2.37 for US customary units and 7.78 for metric units. Figure 1.20 shows potential energy calculated by the calibrated equivalent bilinear against the one calculated by HFD. For case of skew

abutments the reduction factor R remains valid. Figure 1.21 comparatively depicts HFD and bilinear estimations against experimental data.

$$F_{blin} = \frac{\beta H^{2.5}}{1 + \xi_{bli} H} \tag{1.16}$$

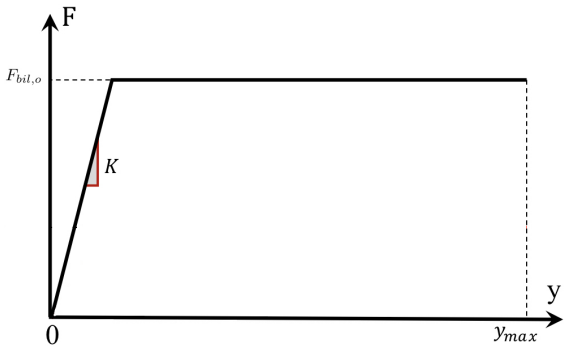

Figure 1.19: Bilinear force-displacement relationship.

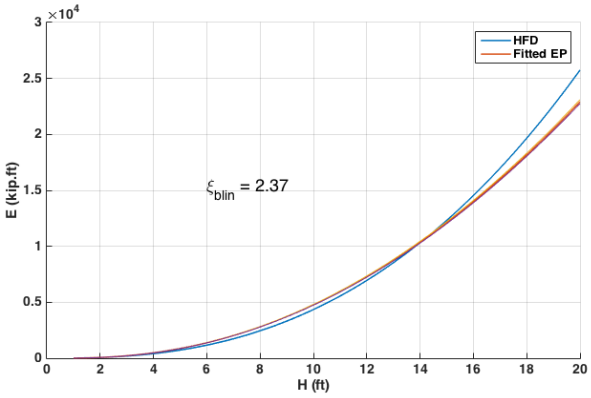

Figure 1.20: The potential energy calculated by the calibrated bilinear model and HFD model.

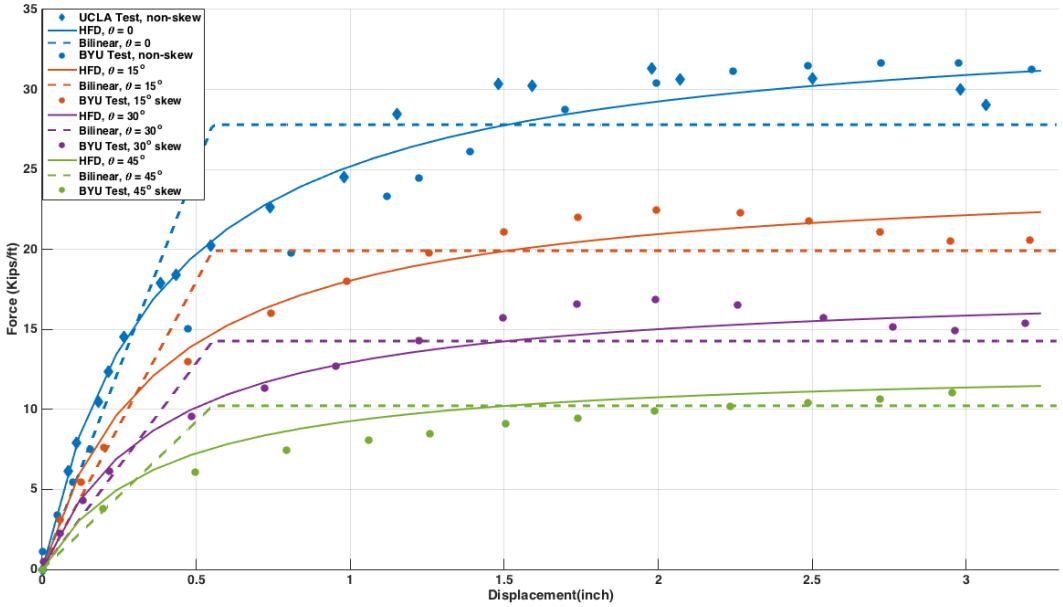

Figure 1.21: Comparison of equivalent bilinear force-displacement and HFD models with UCLA and BYU test data.

1.9 Conclusions and Recommended Future Work

Optimal design and analysis of bridges with skew abutments can always be a challenge due to the complex behavior of backwall-backfill interactions. Our SLSH model and the skew hyperbolic equation facilitates the so called optimal design. These models had been verified against Plaxis 3D FEM simulations as well as full-scale experiments performed at UCLA and BYU.

The SHFD is an extension of the HFD equation proposed by [Shamsabadi et al., 2007]. This is a simple equation that estimates the passive force mobilized behind the unit width of the skew backwall under the straight push scenario. The SHFD has been verified against SLSH and Plaxis 3D simulations and validated agains the large-scale experiment performed in BYU.

Conventional LSH forms the basis of SLSH model which is capable of estimating the behavior of backwall-backfill interactions as a function of displacement and rotation. The objective is to develop the distributed soil springs along the length of the abutment backwall.

Our SLSH, FEM simulations and experimental data shows the exponential decay of

the nonlinear abutment backbone curve as a function of skew angle. The reduction factor $R = e^{-\theta/45}$ originally obtained based on BYU experimental data lies between boundaries of 95% confidence interval of reduction factor calculated from FEM simulation results. In other words, both finite element and large-scale experiment show that $e^{-\theta/45}$ is a reasonable reduction factor.

REFERENCES

[ASTMD1557, 2012] ASTMD1557 (2012). *Standard Test Methods for Laboratory Compaction Characteristics of Soil Using Modified Effort (56,000 ft-lbf/ft3 (2,700 kN-m/m3))*. ASTM International, West Conshohocken, PA.

[Burke, 1994] Burke, M. P. (1994). Semi-integral bridges: Movements and forces. Technical report, Transportation Research Board.

[Caltrans, 2013] Caltrans (2013). *Caltrans Seismic Design Criteria*. California Department of Transportation, Sacramento, CA.

[Duncan and Chang, 1970] Duncan, J. M. and Chang, C.-Y. (1970). Nonlinear analysis of stress and strain in soils. *J. Soil Mech. and Foiund Div. ASCE*, 96(5):1629–1653.

[Kawashima et al., 2011] Kawashima, K., Unjoh, S., Hoshikuma, J.-I., and Kosa, K. (2011). Damage of bridges due to the 2010 maule, chile, earthquake. *Journal of Earthquake Engineering*, 15:1036–1068.

[Khalili-Tehrani et al., 2016] Khalili-Tehrani, P., Shamsabadi, A., Stewart, J. P., and Taciroglu, E. (2016). Physically parameterized backbone curves for passive lateral response of bridge abutments with homogeneous backfills. *Bulletin of Earthquake Engineering*, 14(11):3003–3023.

[Marsh, 2013] Marsh, A. (2013). Evaluation of passive force on skewed bridge abutments with large-scale tests. Master's thesis, Birgham Young University.

[NBI, 2018] NBI (2018). National bridge inventory: Bridge information system.

[Nojoumi, 2016] Nojoumi, A. (2016). *Mldeing the Coupled Cyclic Translational and Rotational Responses of Skew Bridge Abutment Backfills*. PhD thesis, University of California, Los Angeles.

[Ovesen and Stromann, 1972] Ovesen, N. and Stromann, H. (1972). Desgin method for vertical anchor slabs in sand. In *ASCE Proceedings, Specialty Conference on Performance of Earth and Earth-supported Structures*, volume (1)2, pages 1481–1500.

[Sandford and Elgaaly, 1993] Sandford, T. and Elgaaly, M. (1993). Skew effects on backfill pressures at frame bridge abutments. *Transportation Research Record: Journal of the Transportation Research Board*, 1415:1–11.

[Shamsabadi et al., 2017] Shamsabadi, A., Dasmeh, A., and Taciroglu, E. (2017). *Guidelines for Analysis and LRFD-based Design of Earth Retaining Structures*. UCLA, 2 edition.

[Shamsabadi et al., 2010] Shamsabadi, A., Khalili-Tehrani, P., Stewart, J. P., and Taciroglu, E. (2010). Validated simulation models for lateral response of bridge abutments with typical backfills. *Journal of Bridge Engineering*, 15(3).

[Shamsabadi and Rollins, 2014] Shamsabadi, A. and Rollins, K. M. (2014). Three-dimensional nonlinear continuum seismic soil-structure intreaction of skewed bridge abutments. In *Proc. NUMGE 2014, 8th European Conference on Numerical Methods in Geotechnical Engineering*, volume 1, page 6, Delft, The Netherlands.

[Shamsabadi et al., 2007] Shamsabadi, A., Rollinsand, K. M., and Kapuskar, M. (2007). Nonlinear soil–abutment–bridge structure interaction for seismic performance-based design. *Journal of Geotechnical and Geoenvironmental Engineering*, 133(6).

[Vermeer and Brinkgreve, 1998] Vermeer, P. and Brinkgreve, R. B. J. (1998). *PLAXIS: Finite-element code for soil and rock analyses*, version 7.1 edition.

[Yashinsky et al., 2010] Yashinsky, M., Oviedo, R., and Hube, S. A. L. F.-G. (2010). *Performance of highway and railway structures during the February 27, 2010 Maule Chile earthquake*. EERI/PEER/FHWA.

CHAPTER 2

A Validated Lateral Passive Capacity Model for High-Speed Rail Transition Zone Abutments

2.1 Introduction

The California High-Speed Rail (CAHSR) system is being planned to connect major cities of the state of the state (CAHSR, 2018), which renders it to be exposed to all major seismic faults of the state (Field et al., 2018). The seismic performance criteria for HSR bridges are different from highway bridge structures. CAHSR design criteria stipulates the seismic design of all HSR bridges to be based on Operating Base Earthquake (OBE) and Maximum Considered Earthquake (MCE) ground motions with 50-year, and 950 year return periods, respectively (CASHR, 2013). Three levels of seismic performance criteria govern the designs. The Operability Performance Level (OPL), Repairable Performance Level (RPL), and No Collapse Performance Level (NCL). Both RPL and NCL are evaluated with respect to the MCE. For HSR bridges at the OPL performance level, abutment response is required be "essentially elastic (see 11.7.5.1, CASHR, 2013)" and, the displacement levels are required to comply with the OBE limits. Therefore, for the OBE performance requirements, the initial lateral stiffness of the abutment-backfill plays a significant role in the seismic design and analysis of HSR bridges. It is useful to note here that HSR stipulations are different than those for highway bridges, for which a simple idealized bilinear backbone curve is used for seismic design and analysis (Caltrans, 2013). Per CAHSR (2013) design criteria, bridge-abutment transition backfills (BATBs) should be designed to provide a gradual stiffness transition from the bridge deck to the abutment backfill in order to minimize the differential vertical movements between the bridge deck and the abutment due to a traveling train load. A

conventional BATB consists of cement-treated aggregate (CTA) and unbounded compacted aggregate as shown in Figure 2.1. Although passive force-deflection relationships are available for conventional compacted backfill materials (Rollins and Cole 2006; Shamsabadi et al., 2007; Shamsabadi et al., 2010; Khalili-Tehrani et al., 2016), neither numerical/analytical nor experimental studies have been carried out to characterize the passive force-deflection behavior of HSR bridge-abutment transition zones.

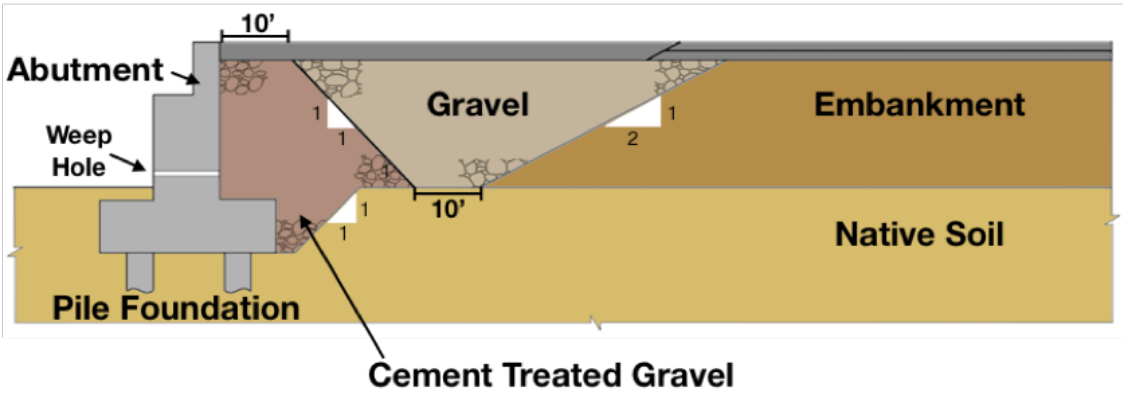

Figure 2.1: California high-speed rail bridge abutment transition backfill configuration.

In the present study a new nonlinear force-displacement backbone curve is proposed based on the experiments performed at Brigham Young University (BYU) on large-scale HSR abutment models. The proposed model shares the same mathematical form –namely a Hyperbolic Force-Displacement (HFD) relationship–as the model previously proposed by the authors for highway bridge abutments with conventional engineered backfill materials (see, e.g., Shamsabadi et al. 2018), but with different parameter values that optimally capture HSR abutment behavior observed in BYU's tests. In the following sections, the setup and measurements form BYUs large-scale tests are provided first. Next, material and load-deformation data from the tests are used for developing detailed three-dimensional nonlinear finite element models that can capture the responses measured during the tests. Finally, both the test data and the simulations with finite element models are used for calibrating a parametric hyperbolic lateral force-displacement backbone curve that is appropriate for HSR bridge-abutment transition zones.

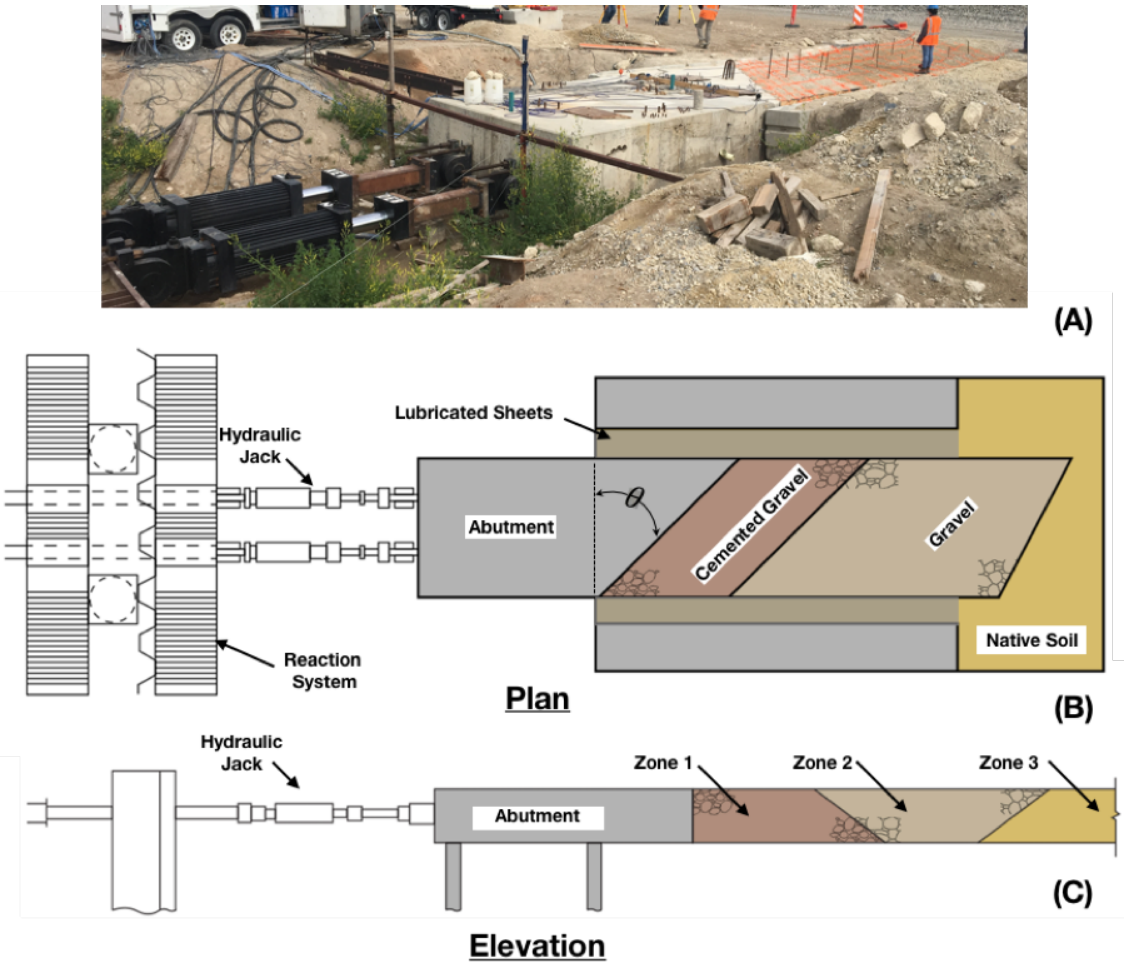

Figure 2.2: Schematic plan and profile of the typical test configuration.

2.2 Large-Scale Tests on Transition Backfills

Lateral passive force-deflection relationships were measured during a series of full-scale bridge abutment tests with skew angles of 0^o, 30^o, and 45^o at a test site located near the Salt Lake International Airport (Figure 2.2 A). As shown in Figure 2B and Figure 2C, the backfill geometry consisted of a zone of CTA backfill (Zone 1) behind an abutment backwall with skew angle θ, followed by a zone of compacted gravel (Zone 2) that stood next to the native soil of the test site (Zone 3). This bridge-abutment transition configuration and backfill materials are in general accordance with the typical section specified in the CAHSR design criteria document (CASHR, 2013).

2.2.1 Test Setup

A reinforced concrete 11ft-wide, 5.5ft-high, and 15ft-long (3.4 m × 1.7 m × 4.6 m) pile cap was used to simulate a bridge abutment backwall. North of the pile cap, an 11ft-wide, 6ft-high, and 32ft-long (3.4 m × 1.8 m × 9.8 m) trench was backfilled to simulate the designed embankment as shown in Figure 2.3A and Figure 2.3B. The embankment comprised one zone of CTA and one of gravel. The CTA was placed and compacted against the pile cap and extending 10 ft (3.0 m) from the pile cap at the embankment surface, then sloping downward with a 1H to 1V slope away from the pile cap. North of the CTA, a zone of "Type 3" gravel was placed with a base width of 10 ft (3.0 m), which was compacted against a 1H to 1V slope of gravel that was already in place. Plywood and double-layer lubricate plastic sheeting were used to line the concrete block sidewalls to the east and west of the backfill zone, as shown in Figure 2.3A, in order to minimize side friction so that a typical segment of wide-approach fills was represented in each test. The backfill Zone 1 of CTA and Zone 2 of gravel are shown in Figure 2.3B and Figure 2.3C. The extent of the passive wedge failure beyond Zone 2 during one of the tests is shown in Figure 3D.

2.2.2 Particle Size Analysis

Backfill materials were tested in compliance with the CAHSR design criteria specifications for particle-size distribution. Type 2 and Type 3 gravel backfills were needed for the transition zone. Figure 2.4 displays the particle-size distribution of the material selected for the Type 2 (CTA) backfill plotted in a solid green line, with the upper and lower bound ranges for acceptable particle-size distribution plotted with dashed lines. Figure 2.5 provides a similar plot for the specially blended material used as Type 3 (gravel) backfill and the corresponding specified range plotted with dashed lines. In both cases, the backfill gradations fall within the specified boundaries.

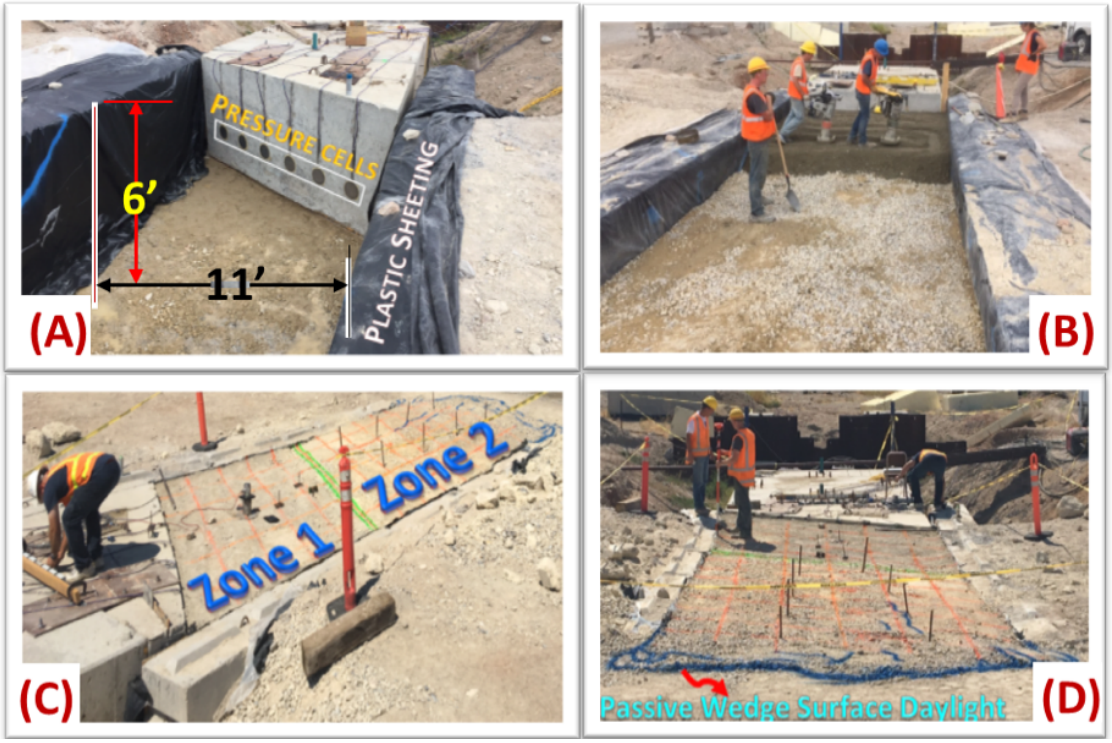

Figure 2.3: Various stages of construction and testing.

2.2.3 Moisture-Density Relationships

For both backfill material types, tests were performed to determine the modified Proctor moisture-density relationship (ASTM D1557). Testing on the CTA was performed at the specified cement content of 3% by mass. The maximum dry density for the Type 2 (CTA) backfill was 138 lbs/ft^3 with an optimum moisture content of 6.5%, while the maxim dry density for the Type 3 (gravel) 135 lbs/ft^3 with an optimum moisture content of 6.5%.

2.2.4 Test Results

Two 600-kip actuators were installed to push the pile cap until passive failure of the backfill in all three tests (see, e.g., Figure 2.3D). Figure 2.8 displays the combined plot of the normal component of the longitudinal force-displacement curves for the three skew angles. The data indicate that the capacity drops with increasing skew angle (from 0^o to 30^o to 45^o), which is a trend that is similar to what was observed for conventional skew highway abutments (Shamsabadi et al., 2018).

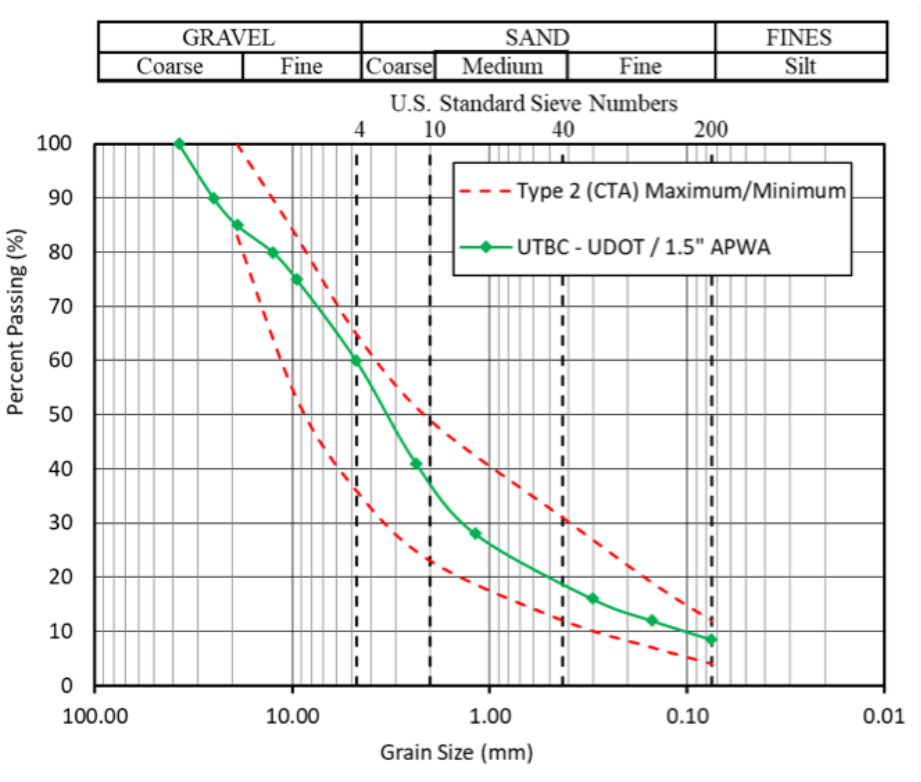

Figure 2.4: Type 2 specification and particle-size analysis of the selected material.

2.3 Finite Element Modeling and Parametric Studies

Detailed three-dimensional finite element (FE) models of the tests were developed and simulations were performed to achieve a more in-depth understanding of the interactions among the backwall and the transition backfill materials. The FE models were created using Plaxis 3D, which is a well-known geotechnical engineering software. Figure 2.6 displays the generic configuration of these finite element models. Each model includes a rigid surface, representing the backwall, and three soil bodies representing the cemented gravel, gravel, and the bottom native soil. PLAXIS' interface modeling features (i.e., frictional contact) were utilized by specifying a reduced wall interface friction angle compared to the soil internal friction (R_{inter}=0.8). The interface of the cemented treated material and the gravel is also modeled using the same feature with the interface reduction parameter R_{inter}= 0.78. In each simulation, a displacement equivalent to 0.04H–with H denoting the height of the backwall– was prescribed to the rigid wall. All other outer boundaries were fixed in their perpendicular

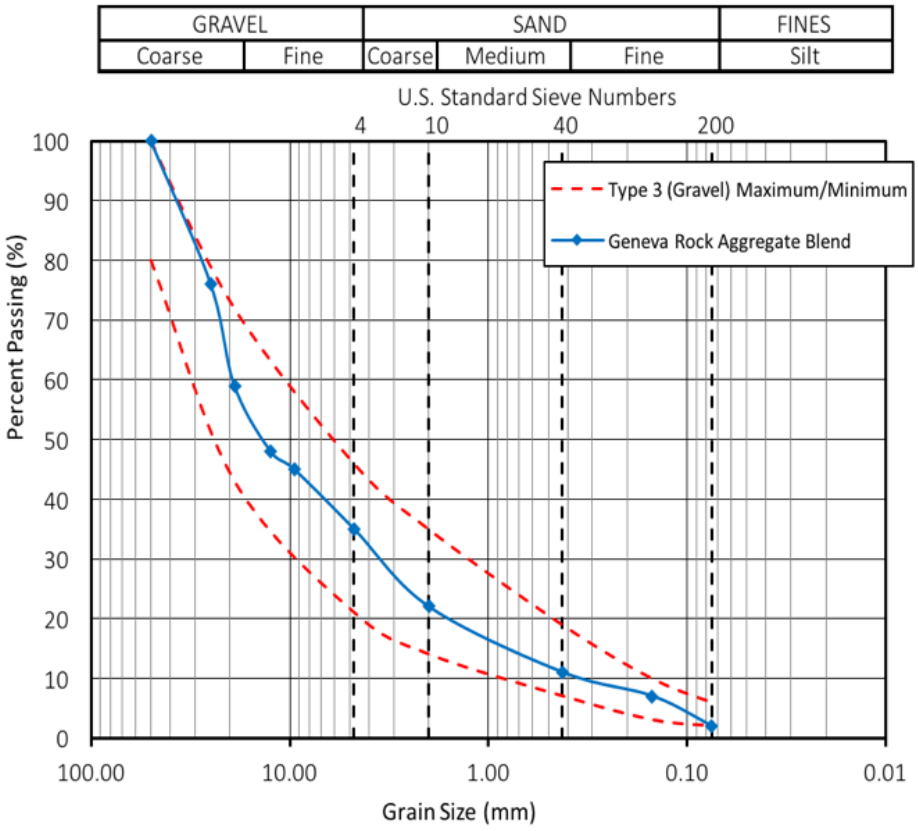

Figure 2.5: Type 3 specification and particle-size analysis of the selected material.

directions, but were allowed to slide (no friction) within the boundary planes–i.e. "Teflon" boundaries were used.

The "hardening-soil model" of Plaxis (2018) was employed to model the cement-treated gravel and the gravel material with using the parameter values given in Table 2.1. The densities of materials were specified per the experiment report (Schwicht, 2018), and other parameters were set within the typical ranges of properties reported by Obrzud and Truty (2018). In the hardening soil model, the values of E_{50}^{ref}, E_{oed}^{ref} , and E_{ur}^{ref} determine the stiffness behavior of the soil. E_{50}^{ref} is the reference modulus corresponding to the reference confining pressure, $E_{oed}^{ref}$is the oedometer loading modulus, and E_{ur}^{ref} is the reference Young's modulus for unloading and reloading, as shown in Figure 2.7. The depth-varying cohesion c(z) for this model is defined using parameters $c_{ref}^{'}$, $c_{inc}^{'}$, and z_{ref} as in

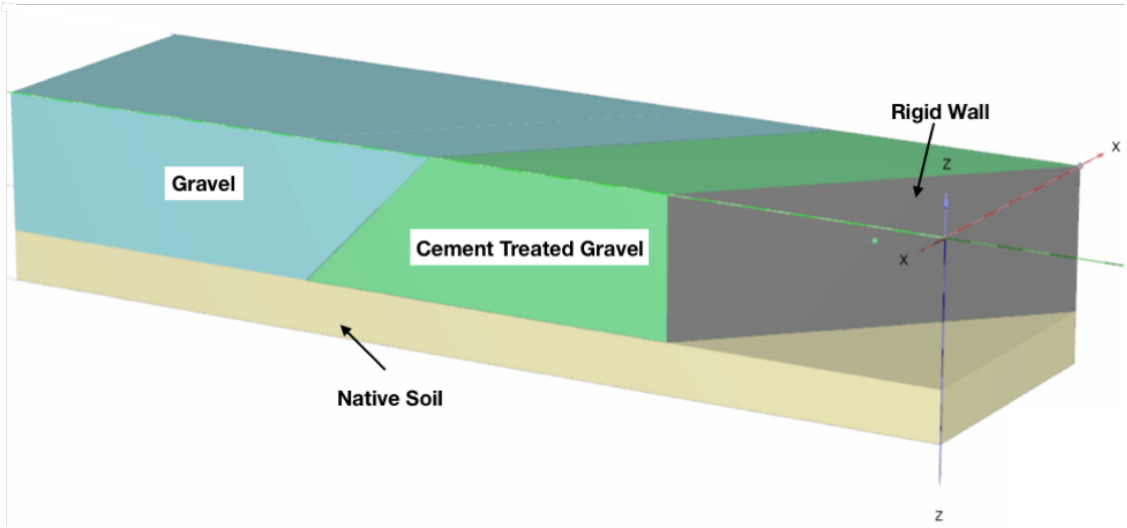

Figure 2.6: TA schematic of the three-dimensional finite element model domains.

$$c(z) = c'_{ref} + (z_{ref} - z)c'_{inc} \tag{2.1}$$

Force-displacement curves obtained from our finite element simulations were generally in good agreement with the those obtained from the tests, as shown in Figure 2.8. Although there are no test data for 15^o and 60^o skew angles, these two skew angle cases were simulated with FE models whose parameters were iteratively calibrated to match the data from 0^o, 30^o, and 45^o skew tests. These additional simulations provided additional data points to calibrate the simplified backbone curve model later. In addition to providing a more refined look at the capacity and initial stiffness reductions due to increasing skew angle, the FE simulations also showed that a log-spiral shaped passive soil wedge was mobilized in the gravel backfill, which matched observations made in prior tests on pile caps reacting against soils (Rollins and Cole, 2006), and abutments reacting against conventional highway abutment backfills (Shamsabadi et al., 2010). Figure 2.9 displays the incremental deviatoric shear strain contours, which illuminates the log-spiral shape of the passive wedge forming in the gravel region. The deformed shape of the finite element mesh, shown in Figure 2.10, indicates that significant strains are confined to the gravel region wherein a significant heave takes place.

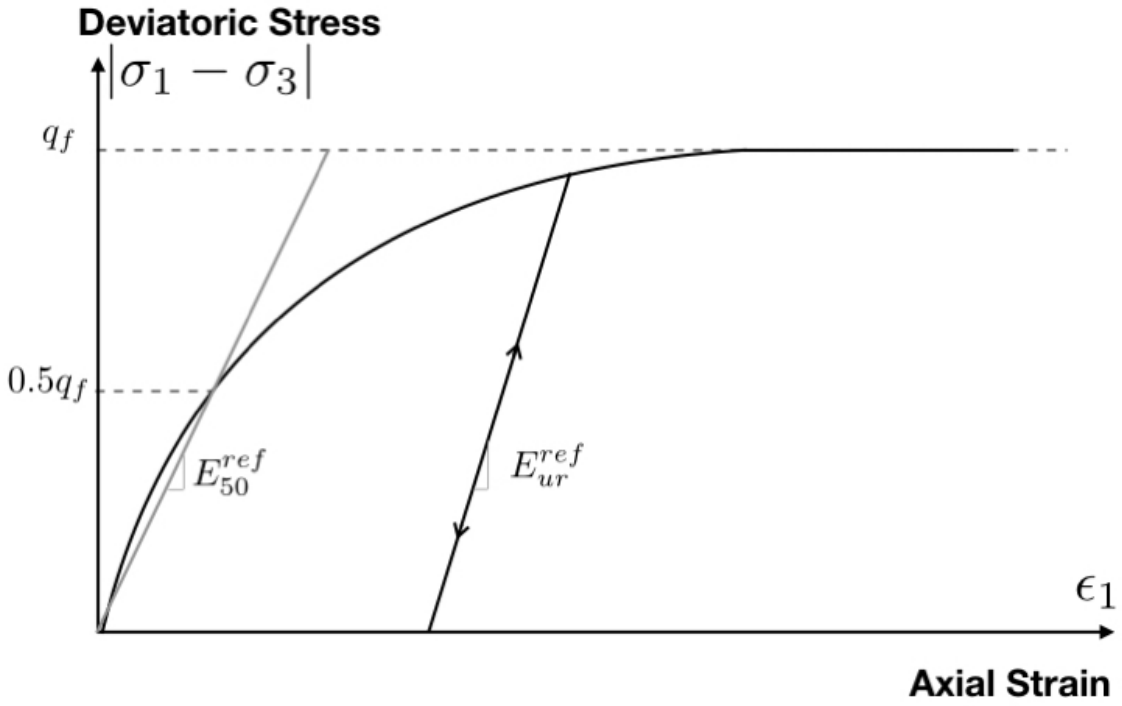

Figure 2.7: The stress-strain relationship of the hardening soil model.

The displacement contour in Figure 2.11 highlights the near-rigid motion of the cemented backfill wedge. These simulations results are in agreement with field observations (see 3.4.1, Schwicht, 2018).

2.4 A Hyperbolic Force-Displacement Backbone Curve

Shamsabadi et al. (2007) had proposed a closed-form hyperbolic force-displacement (HFD) relationship to model the backbone curves for highway bridge abutments. Shamsabadi et al. (2007) found that, for highway bridges abutments with a typical granular backfill of minimum of 95% compaction, the ultimate passive capacity of the abutment-backfill system is reached at a displacement that is approximately $\tau_{hwy} = 5\%$ of the backwall height H. The original HFD formulation was later modified to accommodate the effects of backwall height by Shamsabadi et al. (2010). The HFD formula was further extended to incorporate the effects of skew angle on capacity and stiffness reductions by Shamsabadi et al. (2018) using an exponential reduction factor $R(\theta)$. The latest formulation was dubbed SHFD, wherein

Table 2.1: Soil Parameters.

Gravel Hardening Soil Parameters		
Property	Metric	US Customary
Density, γ	22.6 kN/m^3	0.144 kcf
E_{50}^{ref}	384 MPa	8,000 ksf
E_{oed}^{ref}	192 MPa	4,000 ksf
E_{ur}^{ref}	1152 MPa	24,000 ksf
c'_{ref}	12 kPa	0.25 ksf
c'_{inc} (avg.)	12 kPa	0.25 ksf
z_{ref}	1.67 m	5.5 ft
ϕ	41^o	41^o
ψ	11^o	11^o
R_{inter}	0.78	0.78
Cement Treated Gravel Hardening Soil Parameters		
Density, γ	23.1 kN/m	0.147 kcf
E_{50}^{ref}	720 MPa	15,000 ksf
E_{oed}^{ref}	720 MPa	15,000 ksf
E_{ur}^{ref}	2160 MPa	45,000 ksf
c'_{ref}	48 kPa	1 ksf
c'_{inc} (avg.)	0.0389 MPa/m	0.25 ksf/ft
z_{ref}	1.67 m	5.5 ft
ϕ	41^o	41^o
ψ	11^o	11^o
R_{inter}	0.8	0.8

"S" stands in for "skew."

The primary parameters of the SHFD formulation?which is completely defined through Eqs. 2.2 through 2.8 below are stiffness at 50% of capacity (K_{50}), the ultimate passive capacity of the abutment-backfill system (F_{ult}), and the ultimate displacement when the passive capacity is reached (y_{max}), as shown in Figure 2.12.

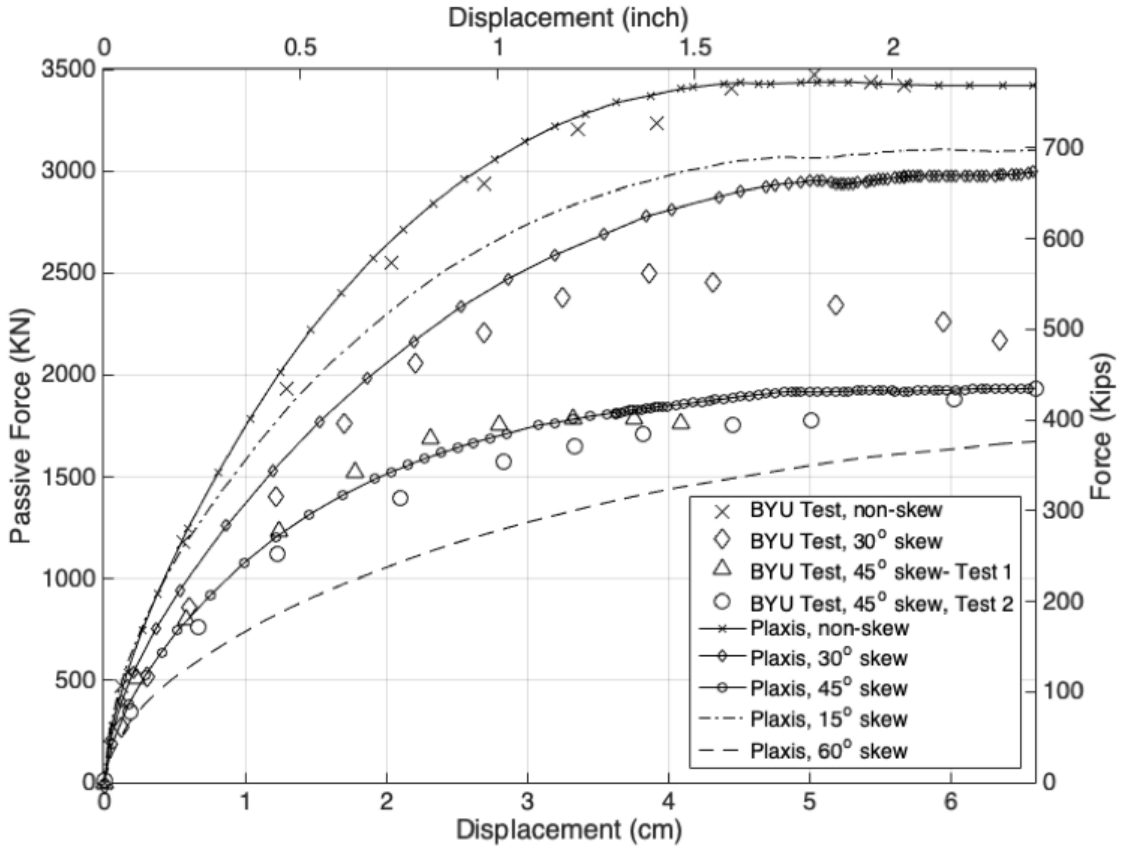

Figure 2.8: Force-displacement curves obtained by finite element simulations versus large-scale test data.

$$F(y) = \frac{Cy}{(1+Dy)} R?(\theta) \tag{2.2}$$

$$C = 2K_{50} - \frac{F_{ult}}{y_{max}} \tag{2.3}$$

$$D = 2(\frac{K_{50}}{F_{ult}} - \frac{1}{y_{max}}) \tag{2.4}$$

$$Fult = \frac{(\beta H^{2.5})}{(1+\xi H)} \tag{2.5}$$

$$K_{50} = (\psi H + \mu) \tag{2.6}$$

$$R(\theta) = \exp(-\theta/\eta) \tag{2.7}$$

$$y_{max} = \tau H \tag{2.8}$$

In the equations above, F is the passive lateral abutment reaction force, and y is the

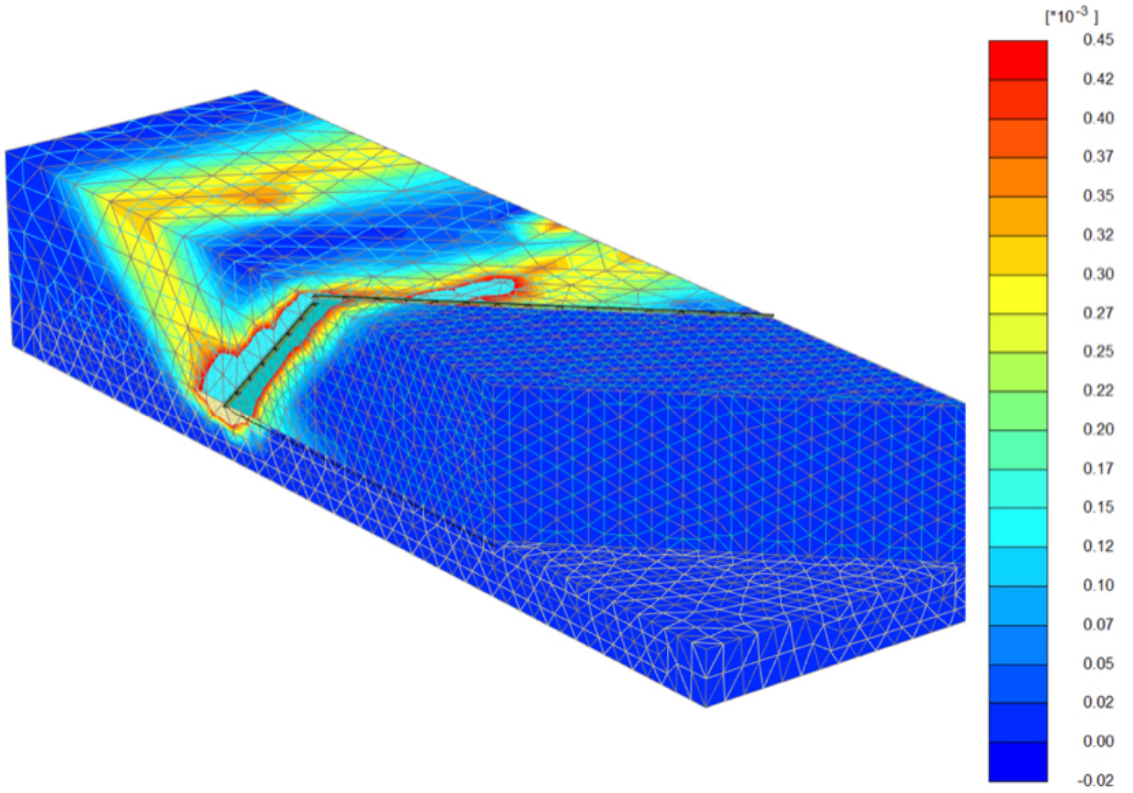

Figure 2.9: Incremental deviatoric shear strain contour indicates that a passive soil wedge is mobilized in the gravel region of the transition backfill.

lateral bridge deck displacement at the abutment. The parameters K_{50} and F_{ult} are functions of height of the backwall (H) and the backfill material properties, which are represented by β, ξ, ψ, and μ. Shamsabadi et al. (2018) back-calculated the values of these material dependent constants from test data and results from simulations with validated finite element models for highway bridge abutments with engineered backfill materials with 95% compaction ratio.

In order to use the same formulation for HSR transition abutments, all of the parameters of the original SHPD need to be recalibrated, which is possible by using BYU's test data as well as simulation results from the validated FE model described in the previous section. We first focus on parameter ?, which controls how rapidly the lateral backbone curve decays with respect to skew angle (see, Eq. 2.7). For typical engineered backfills of highway bridges with 95% compaction ratio, the value of this parameter is $\eta = 45$. (Shamsabadi et al., 2018). For HSR abutments with transition backfill materials, the reduction in capacity at different displacement levels for each skew angle (here, 0^o, 15^o, 30^o, 45^o, 60^o) are obtained using the

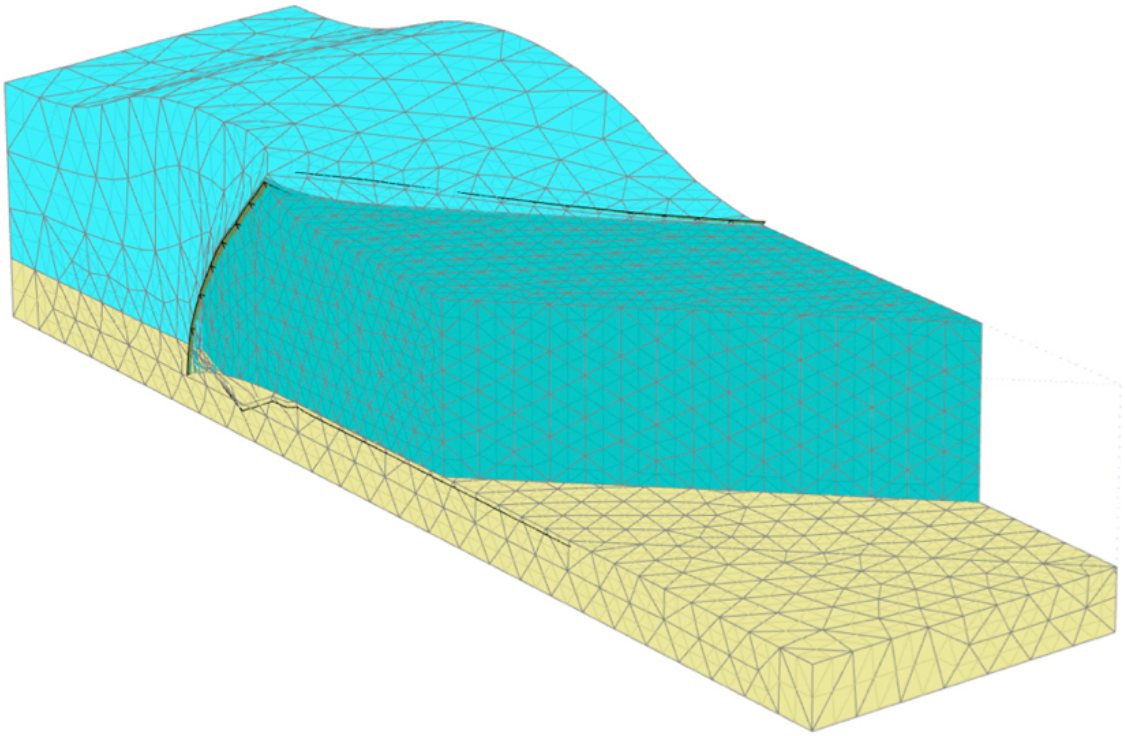

Figure 2.10: The deformed shape of the transition backfill due to a passive displacement of the backwall wherein a significant heave is observed in the gravel backfill.

finite-element simulations as well as BYU test data. Figure 2.13 displays a scatter plot of these reduction ratios. For the sake of simplicity and to retain the same functional form (i.e., exponential) of the original SHFD formulation, we opt here to use the following formula for $R(\theta)$:

$$R(\theta) = \begin{cases} \exp(-\theta/150) & 0 < \theta \leq 30^o \\ 1.8\exp(-\theta/38)), & 30^o < \theta \leq 45^o \\ \exp(-\theta/75), & \theta > 45^o \end{cases} \tag{2.9}$$

The reduction ratio $R(\theta)$ is also plotted in Figure 2.13 where it can be seen that the agreement between this ratio and reductions observed in BYU tests (0^o, 30^o, 45^o) as well as reductions predicted by FE simulations (15^o, 30^o, 45^o, 60^o) are generally in good agreement. Scattered points shows reduction ratio at different displacements for a given skew angle. The

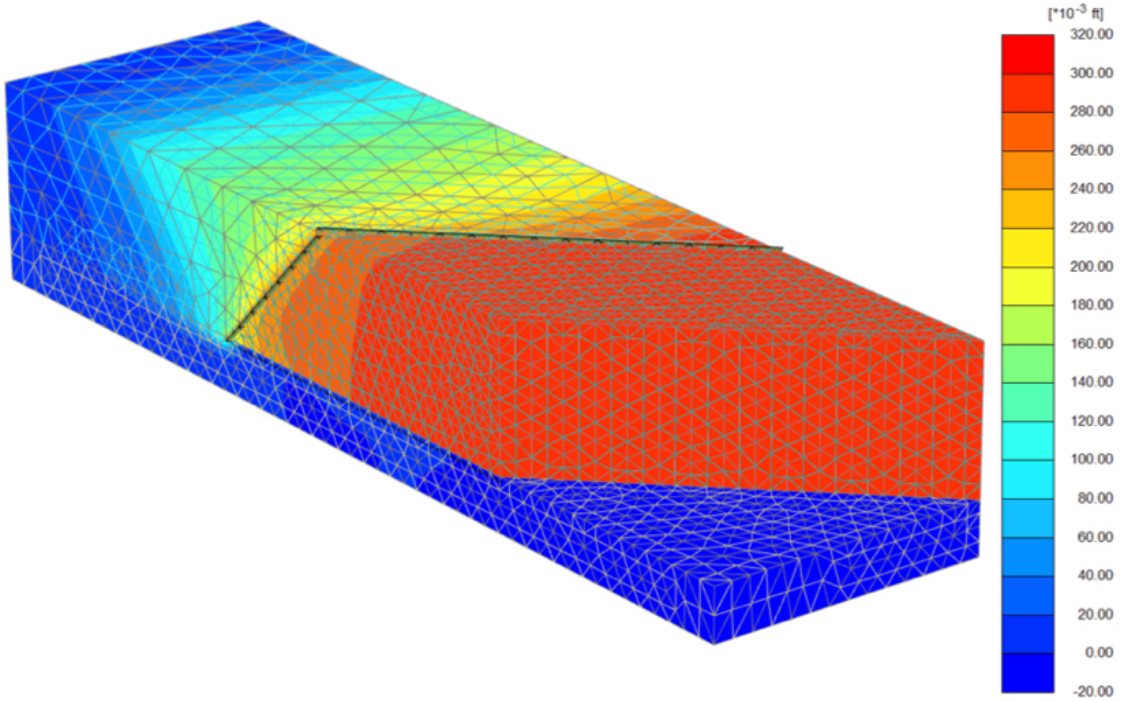

Figure 2.11: Displacement contour plot. The near-uniform warm colors in the cemented backfill region suggests that it moves almost rigidly.

sizes of symbols for a given skew angle increase as the displacement increases. $R(\theta)$ is chosen such that it provides a good estimation of the passive capacity at the ultimate displacement. The same figure also includes the skew reduction ratio used for conventional highway bridges for comparison (Caltrans SDC, 2018).

After settling the reduction ratio, it is now possible to determine the optimal values of the SHFD parameters for the HSR application by utilizing the BYU test data. For this purpose, we first construct a cost function and minimize it with respect to the model parameters ξ,ψ, μ and κ, as in

$$\min_{\beta,\xi,\psi,\mu,\kappa,\lambda} ||F_{BYU}(\bar{y}) - F_{SHFD}(\bar{y},\beta,\xi,\psi,\mu,\kappa)|| \tag{2.10}$$

where $\bar{y}$ is the array of measured displacements during the tests, and F_{BYU} and F_{SHFD} respectively denote the normal components of the experimental passive force and the force predicted by the SHFD model as shown in Figure 2.14.

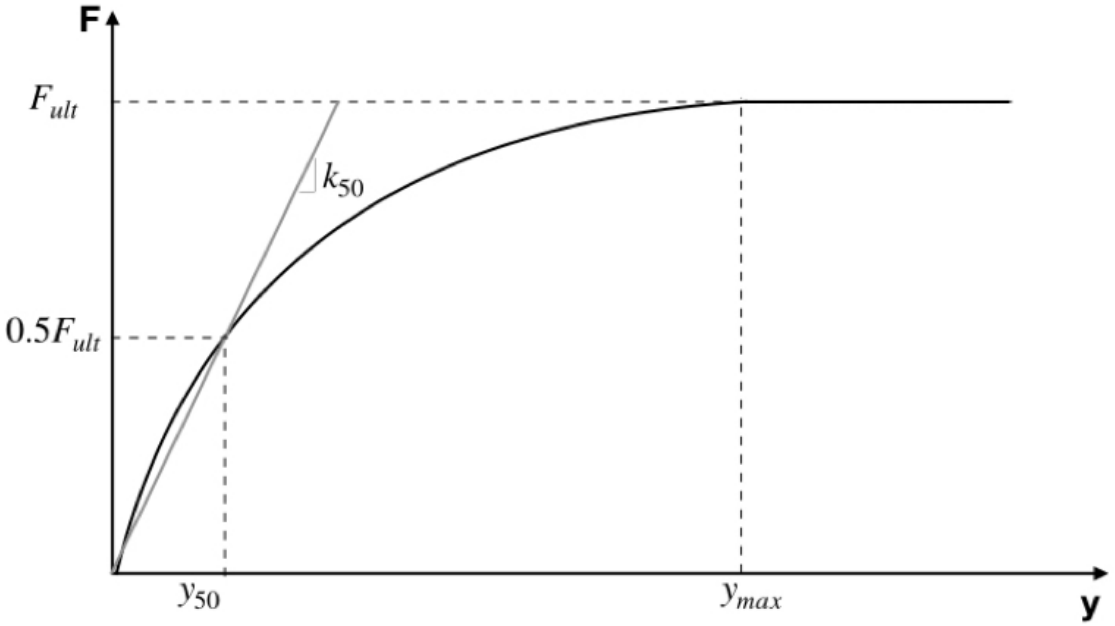

Figure 2.12: The Hyperbolic Force-Displacement (HFD) relationship used by Shamsabadi et al. (2018).

The optimal values of this nonlinear least-squares minimization problem are presented in Table 2.2, and the resulting SHFD model's force-displacement backbone curves are presented along the with BYU data in Figure 2.15. It can be seen that the calibrated SHFD model mimic the test data quite well. It is useful to note there that this figure also contains data from a second 45^o skew BYU test that was not used in calibrating the SHFD model above, which indicates that the test data are reliable/repeatable, and partially validates the SHFD model for HSR bridge-abutment transition zone applications.

Table 2.2: Optimized parameters of HFD equation for HSR transition abutments.

Constant	US Customary	Metric
β	11	3131.2
ξ	1.8	5.91
ψ	11	20,744
μ	40	22,992
κ	0.04	0.04

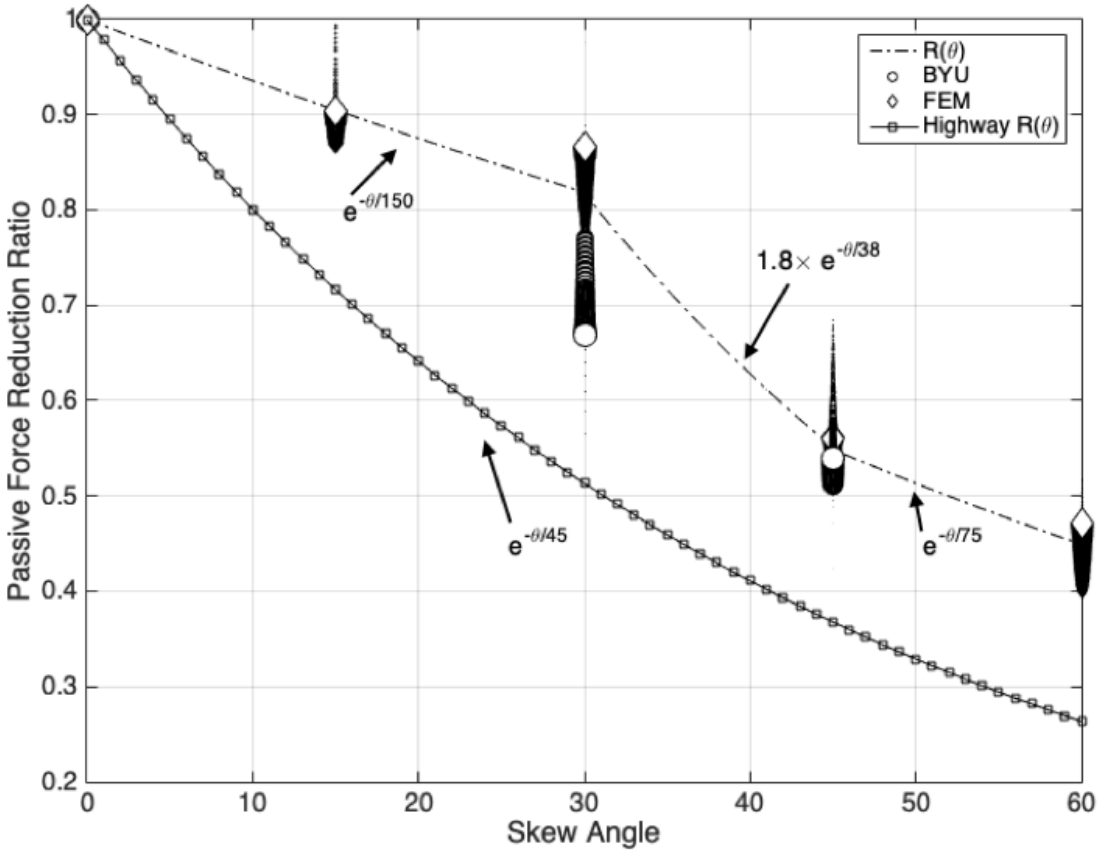

Figure 2.13: Reduction Factor scatter plots represent the reductions factors at different displacements.

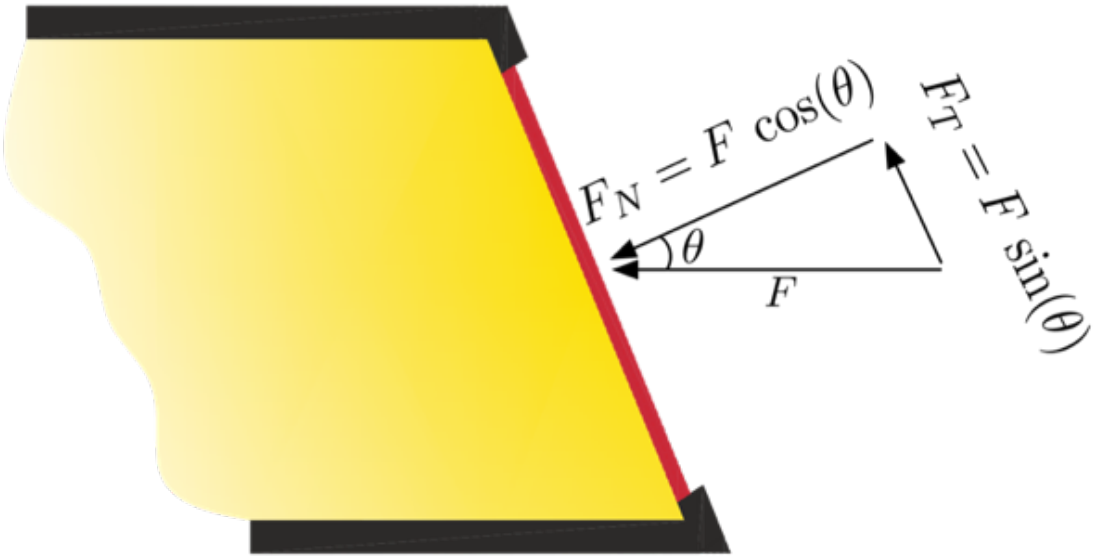

Figure 2.14: Normal (F_N) and transverse (F_T) actuator thrust components resisted by the backfill passive reaction.

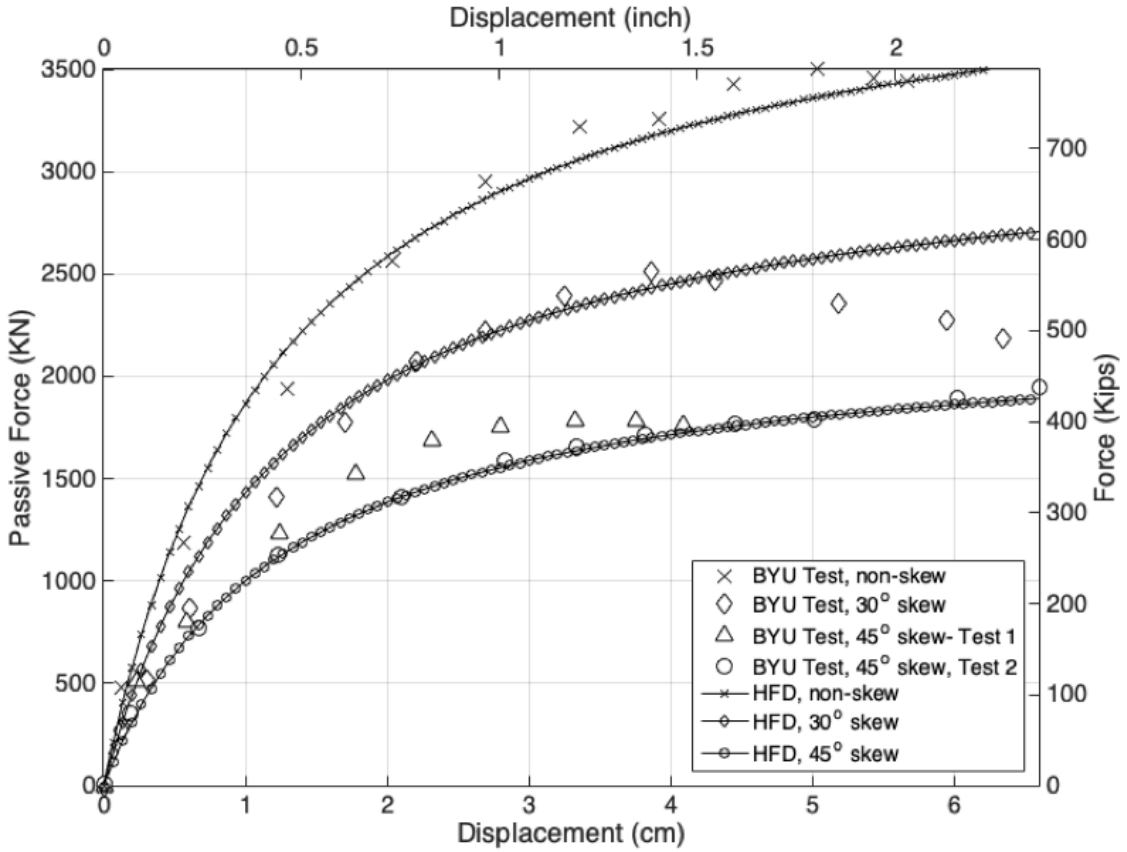

Figure 2.15: Optimized SHFD equation and the force-displacement data measured in BYU's large-scale tests.

2.5 Practical Implications

The current HSR bridge design employs bilinear elastic-perfectly plastic force-displacement relationships proposed by Caltrans Seismic Design Criteria (SDC 2.0). This formulation has been originally developed by Shamsabadi et al. (2018) for highway bridges with typical engineered backfill material. The use of SDC formulation results in underestimations of both stiffness and passive capacity. This issue has been discussed in the following example involving an HSR bridge abutment with 3.35 m (11 ft) height and 13.1 m (43 ft) width (Figure 2.16).

Following the current Caltrans SDC, the passive capacity and stiffness for the elastic-perfectly-plastic force displacement backbone (shown in Figure 2.1) for this HSR abutment would be predicted using

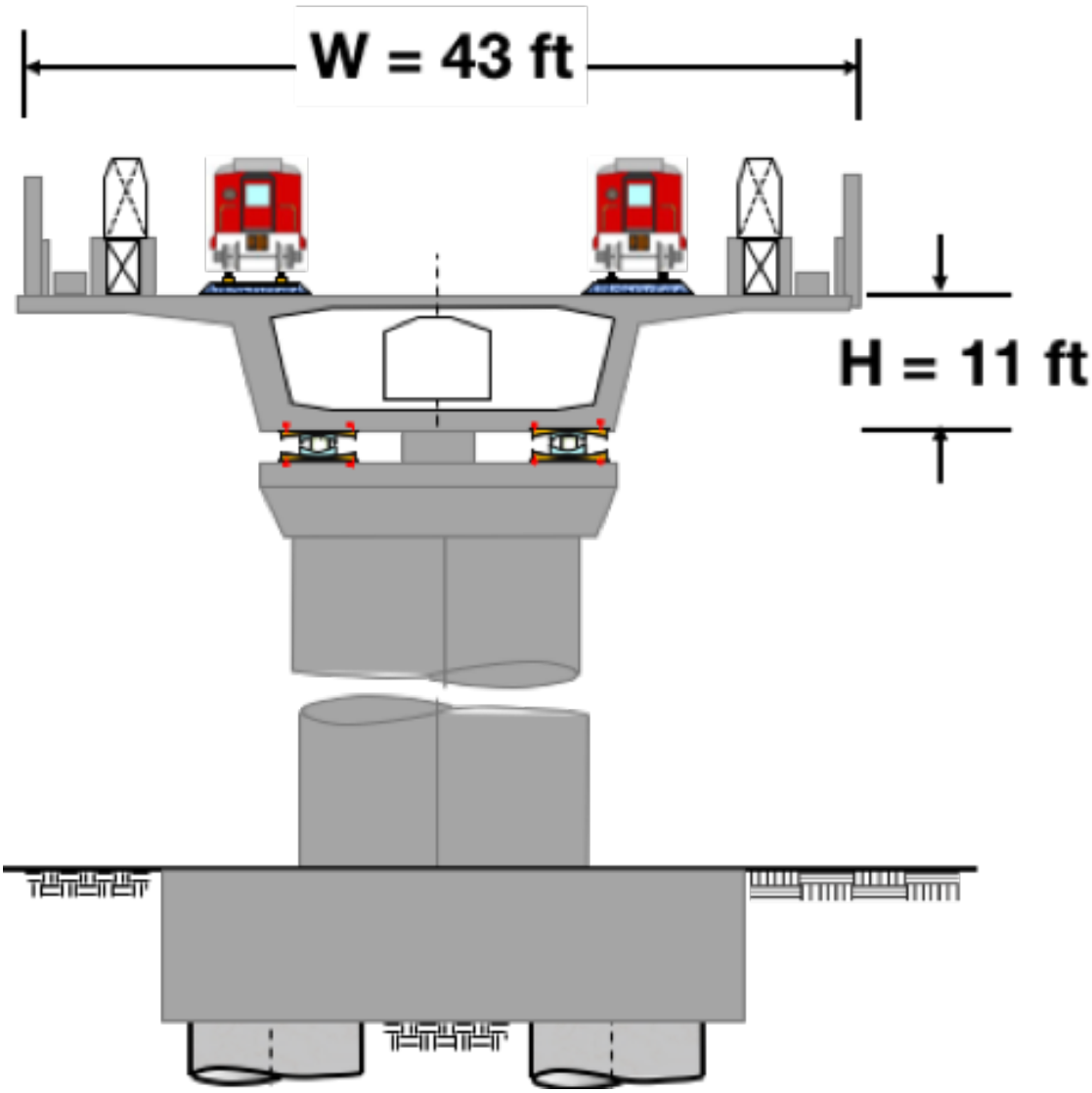

Figure 2.16: An example HSR bridge section.

$$F_{ult}^{SDC} = \frac{5.5H^{2.5}}{1+2.37H} W\, R(\theta) \tag{2.11}$$

$$K^{SDC} = (11H+40) W\, R(\theta). \tag{2.12}$$

where US Customary units are used and W denotes the width of the backwall in ft. On the other hand, we can produce an estimate of the backbone curve Eqs. (2.2)-(2.8) and (2.11), and (2.12). These the capacity and stiffness resulting from these equations, which are

appropriate for HSR, are tabulated in Table **??**; and the SDC and HSR Force-displacement curves are compared in the Figure 2.18.

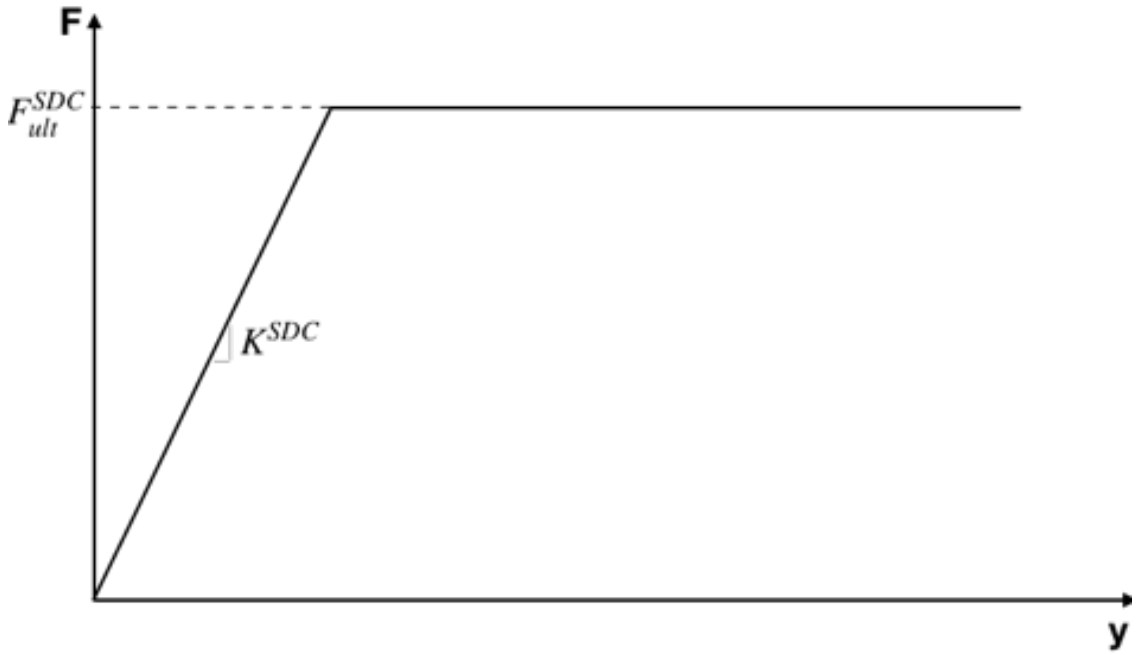

Figure 2.17: The elastic perfectly plastic force-displacement relationship proposed by Shamsabadi et al. (2018) used in Caltrans SDC for highway bridge abutments.

Table 2.3: Comparison of the capacity and stiffness calculated using SDC and proposed HFD formula for HSR.

Skew Angle	Width (m)	F_{ult}^{SDC} (MN)	F_{ult}^{HSR} (MN)	Capacity Ratio	K^{SDC} (MN/m)	K_{50}^{HSR} (MN/m)	Stiffness Ratio
0^o	13.1	15.6	40.6	2.6	60.5	121.2	2.0
45^o	18.6	8.1	31.6	3.9	31.6	94.2	3.0

As seen in Table 2.3, use of SDC formulation for HSR abutments results in the underestimation of the capacity by factors of 2.6 and 3.9 for 0^o skew and 45^o skew angles, respectively. Also, SDC underestimates the stiffness by factors of 2 and 3, respectively.

It should be noted that the underestimation factors between the SDC and HSR formulations vary with skew angle and abutment height. Figure 2.19 (A) and (B) display the color-mapped surface plots for passive capacity ratios and stiffness ratios between the SDC

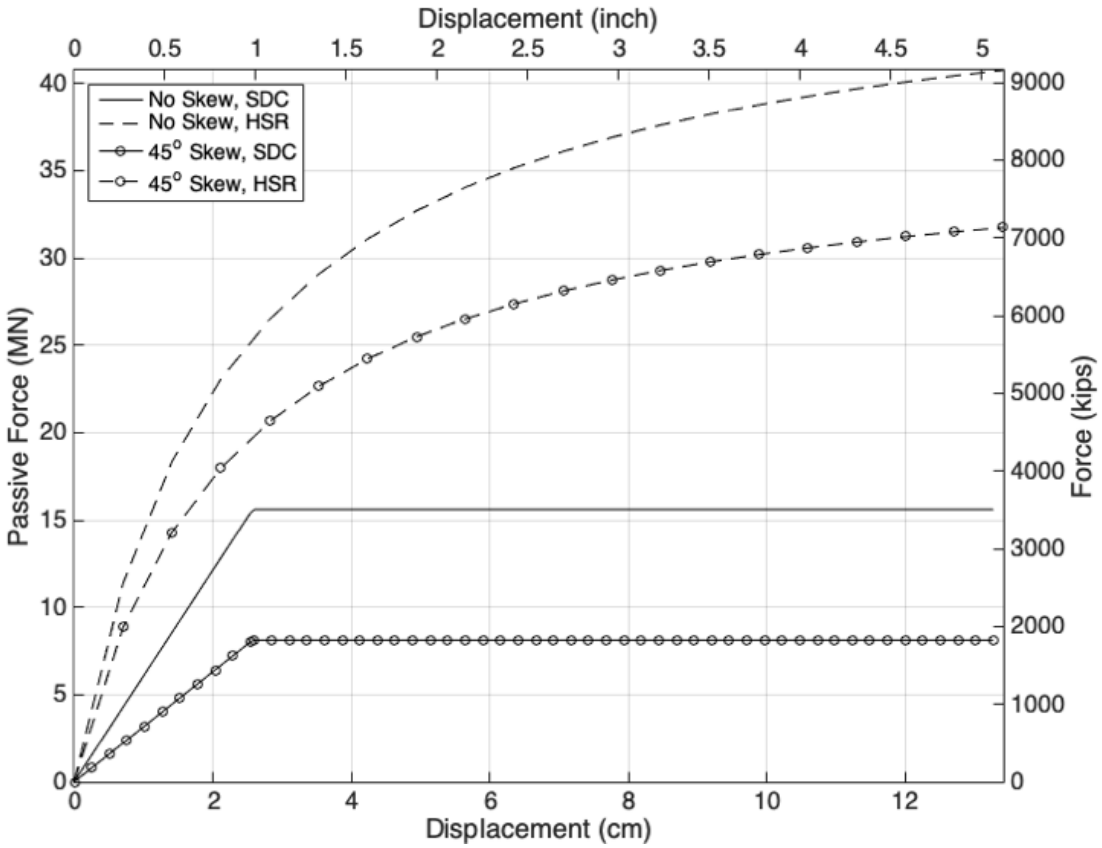

Figure 2.18: Comparison of force-displacement curves for obtained by SDC formulation versus proposed HFD equation for HSR abutments for the example abutment.

and HSR formulations for the typical ranges of skew angles and backwall heights. It can be seen in these figures that for typical abutments ratio of passive capacities between HSR and SDC can vary from 2 to 4.5 and for stiffness it can vary from to 2 to 3.4. Both figures clearly show that the skew angle has a far more pronounced effect than the backwall height on both stiffness and the passive capacity ratios between the two formulations.

2.6 Summary and Conclusions

Data from a series of full-scale lateral abutment load tests and simulations with detailed finite element models were used for developing passive lateral force-displacement relationships for bridge-abutment transition zone backfills for seismic analyses. Such backfills consist of cement-treated aggregate (CTA) (here with 3% cement) and compacted gravel. The

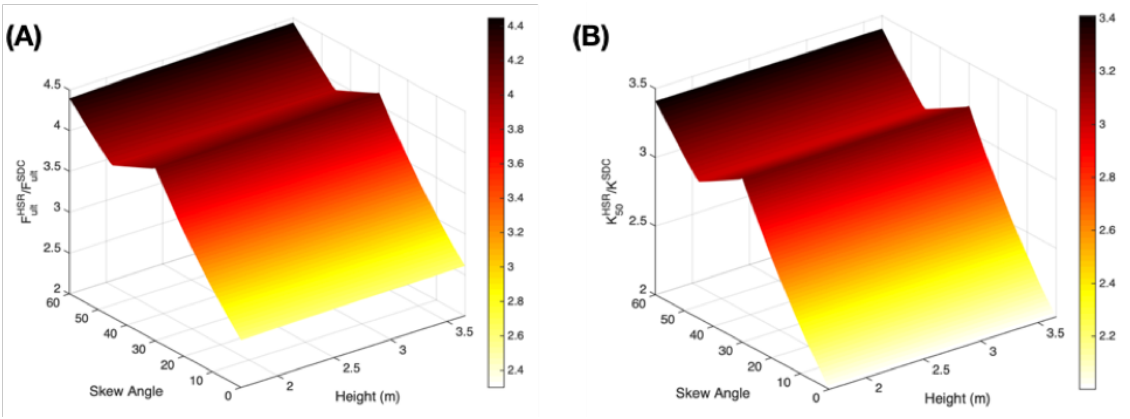

Figure 2.19: Color-mapped ratios of (A) passive capacity and (B) stiffness calculated using Caltrans SDC and the proposed HSR SHFD for skew angles ranging from 0 to 60o and wall heights ranging from 1.65 to 3.65 meters.

transition zone backfills are nominally designed to minimize differential movements between the bridge deck and the abutment due to traveling trains. While there is adequate literature on this particular function of the transition backfills, their lateral seismic responses have not been previously characterized.

This study offered a parametric model of the lateral force-displacement backbone curve that takes into account the height of the abutment backwall as well as its skew angle. Dubbed as the Skew Hyperbolic Force-Displacement (or SHFD) model, the resulting parametric backbone curve shares the same functional form (but different parameter values) with an earlier model that was designed for highway bridge abutments.

Based on the model and the observations made from the tests, the following conclusions can be drawn:

1. The peak passive force developed for HSR abutments is higher–ranging from 2 to 4.5 times higher with skew angles ranging from 0^o to 60^o– than what is predicted for highway abutments (specifically Caltrans granular backfill materials) for the same backwall height.

2. The displacement required to develop the peak passive force decreases with skew angle and the reduction observed for HSR abutments is less than that for comparable highway abutments.

3. The peak passive force is developed when the lateral displacements reach around 4% of the wall height (H) for the HSR abutment (as opposed to 5% of H for the conventional highway abutment).

4. Field measurements suggest that the CTA backfill moves more or less rigidly with the abutment, and does not exhibit significant heave. The shear failure and heaving is confined to the granular backfill behind the CTA zone.

REFERENCES

ASTM D1557-07 (2007). Standard Test Methods for Laboratory Compaction Characteristics of Soil Using Modified Effort (56,000 ft-lbf/ft^3 (2,700 kN-m/m^3)), ASTM International, West Conshohocken, PA, 2007, www.astm.org.

CAHSR (2013). *California High Speed Train Project Design Criteria* (HSR 13-06), California High Speed Rail (CAHSR) Authority, Sacramento CA (weblink) [last accessed January 02, 2019].

CAHSR (2018). *California High-Speed Rail 2018 Business Plan.* CAHSR Authority, Sacramento CA (weblink) [last accessed January 02, 2019].

Caltrans (2018). *California Department of Transportation (Caltrans) Seismic Design Criteria v.2.0*, Sacramento, CA.

Field EH, Biasi GP, Bird P, Dawson TE, Felzer KR, Jackson DD, Johnson KM, Jordan TH, Madden C, Michael AJ, Milner KR, Page MT, Parsons T, Powers PM, Shaw BE, Thatcher WR, Weldon II RJ, Zeng Y (2013), Uniform California earthquake rupture forecast, version 3 (UCERF3)The time-independent model: U.S. Geological Survey Open-File Report 20131165, 97 pp., California Geological Survey Special Report 228, and Southern California Earthquake Center Publication 1792 (url: http://pubs.usgs.gov/of/2013/1165, last accessed, January 02, 2019).

Khalili-Tehrani P, Shamsabadi A, Stewart JP, Taciroglu E (2016). Backbone curves with physical parameters for passive lateral response of homogeneous abutment backfills. *Bulletin of Earthquake Engineering*, 14(11), 3003-3023.

PLAXIS (2018). Material Models Manual (weblink) [last accessed, January 02, 2019].

Rollins KM, Cole RT (2006). Cyclic Lateral Load Behavior of a Pile Cap and Backfill. *ASCE Journal of Geotechnical and & Geoenv. Engineering*, 132(9), 1143-1153.

Shamsabadi A, Dasmeh A, Nojoumi A, Rollins K. M., Taciroglu E (2018). A Lateral Capacity Model for Backfills Reacting Against Skew-Angled Abutments under Seismic Loading. *ASCE Journal of Geotechnical & Geoenv. Engineering* (2018 under review).

Shamsabadi A, Khalili-Tehrani P, Stewart JP, Taciroglu E (2010). Validated Simulation Models for Lateral Response of Bridge Abutments with Typical Backfills. *ASCE Journal of Bridge Engineering*, 15(3), 302-311.

Shamsabadi A, Rollins KM, Kapuskar M (2007). Nonlinear Soil-Abutment-Bridge Structure Interaction for Seismic Performance-Based Design. *Journal of Geotechnical & Geoenv. Engineering*, 133(6), 707-720.

Schwicht DEW (2018), Large-Scale Strength Testing of High-Speed Railway Bridge Embankments: Effects of Cement Treatment and Skew Under Passive Loading, *M.Sc. Thesis, Brigham Young University.*

Obrzud R, Truty A (2018). The Hardening Soil ModelA Practical Guidebook. *Z_Soil. PC 100701 Report.* Zace Services Ltd., Software engineering, CH-1028 Preverenges Switzerland.

CHAPTER 3

A Lumped Impedance Model for Nonlinear Time-History Analysis of Retaining Walls

This chapter describes a new model—dubbed here as the Lumped Impedance Model (LIM)—that can predicted the responses of earth-retaining walls and the retained soil under seismic shaking, including the inelastic response of the soil under active and passive conditions as well as residual wall displacements and rotations. The formulation of LIM is introduced and verified against various analytical solutions as well as detailed finite element simulations. Potential extensions of LIM are also outlined, together with a basic performance-based seismic assessment and design framework for earth-retaining structures, which uses LIM as its computational engine.

The remainder of this Chapter is structured as follows: First, a summary of literature on experimental and analytical studies on retaining walls is provided. The available methods are categorized into various groups and shortcomings of each group are discussed. The proposed Lumped Impedance Model (LIM) is developed and verified next. The formulation of the LIM for a rigid wall resting on a rigid base retaining an elastic material in the frequency domain is explained, and it is verified against exact analytical and simplified solutions. Then the implementation of the LIM for a cantilevered wall retaining an elastic soil in the time domain is explained and verified against ABAQUS FEM simulations. Subsequently, the innovative fuse element is introduced, and its application for simulating elastoplastic behavior of wall-backfill under quasi-static passive and active conditions are verified. In the last part of part two full implementation of LIM in the time-domain for cantilevered wall

retaining elastoplastic soil is explained and verified against FEM simulations.

In part three, the reason for the unsuitability of FEM for conducting performance-based assessments for retaining walls and also exigency of a computationally inexpensive model for such aim is discussed. LIM's capability for performing such intensive analysis is demonstrated by developing a fragility curve for a sample retaining wall. Finally, necessary expansions of LIM for making it a comprehensive performance-based design engineering tool is explained.

3.1 Introduction

Earth-retaining structures are ubiquitous in highway construction, and their potential failure during seismic events bears significant consequences. Repair/retrofit/ replacement of these structures "can become extremely costly, and time-consuming," as such, research on improved design and analysis methods for retaining structures is stated as having the "highest priority" in NCHRP Report 611 (2008). Despite, their strong performances in past earthquakes, there does not appear to be any consensus on the level of design conservatism the existing earth-retaining structures exhibit. Many engineers claim that there is gross conservatism in current methods of analysis (e.g., Al Atik and Sitar, 2010; Lew et al., 2010), while others have stated that those same design methods are non-conservative (e.g., Wood 1973; Veletsos and Younan, 1994; Ostadan, 2005).

Most of the studies in the literature use Mononobe-Okabe (M-O) equations for determining seismic pressures on a retaining wall subjected to seismic excitations. The M-O equations are based on a presumption that the wall yields or moves sufficiently that a soil wedge is created behind the wall. Most of the studies during 1980-2007 (Bolton and Steedman, 1982; Sherif et al., 1982; Ortiz et al., 1982; Steedman, 1984; Steedman and Zeng, 1990; Stadler, 1996; Madabhushi and Zeng, 2007) considered the MO predictions to becredible. The NCHRP 611 report and also recent versions of AASHTO Bridge Design Specifications assesses the MO method to be overly-conservative and alleviates this issue by recommending

the use of half of the peak ground acceleration as the seismic coefficient. The centrifuge test by Al Atik et al. (2010) also argues that methods based on the MO theory significantly overestimate the recorded pressures and moments.

The basic shortcomings of the M-O model are recognized as (see, for example, NCHRP Project 12-70, 2008) follows:

Backfill Cohesion & Active Pressures: MO equations are based on a homogeneous cohesionless backfill and Coulomb failure-wedge hypothesis. For soils where the shear strength is due to internal friction (ϕ) and cohesion (c), the distribution and magnitude of the active pressures are largely unknown. Current provisions stipulate that the incremental seismic load distribution is uniform, and hence its resultant is at the mid-height of the wall. There is a consensus—which is supported by experimental evidence and analytical studies (e.g., by Saran and Prakash, 1968; Richards and Shi, 1994; Shukla et al., 2009)–that this stipulation incorrect and overly conservative (cf. B7.3.3, Anderson et al., 2008).

Passive pressures: An accurate accounting of passive pressures is needed to determine the resisting force at the toe of standard semi-gravity walls, and at the wall-face for pile-supported cantilever walls. Again, the MO equations do not provide this information, and should not be used. While there are more sophisticated limit-equilibrium methods for determining the passive pressures for general $c - \phi$ backfills (Shamsabadi et al., 2013; Xu et al., 2015), however, they currently do not take wave propagation and wall flexibility effects into account and should be extended.

Sloping backfill and high seismic coefficient: The M-O equations possess mathematical singularities for certain values of the backfill slope angle and for high seismic coefficients. These problems may cause non-physical predictions in the form of "unrealistically large seismic active earth pressure coefficients," or "infinite earth pressures" (NCHRP (2008)).

An important consideration lacking in the current design guidelines of earth retaining structures is the prediction of permanent wall displacements (e.g., lateral translation and rotation). Force-based approaches are based on designing the system to withstand peak seismic loads. Unless the system being designed is very fragile (i.e., low ductility), force-based designs will be overly conservative (FHWA (2011)). While there have been continued attempts at devising predictive models of residual wall displacements since the late 60s (e.g., Newmark (1965); Richard and Elms (1979); Nadim and Whitman (1983); Cai and Bathurst (1996)) observations from recent earthquakes (e.g., Al-Homoud and Tahtamoni (2000); Fang et al. (2003); Zhang et al. (2012)), as well as comparisons against experimental measurements (e.g., Cascone et al., 1995; Watanabe et al., 2003) have demonstrated that this issue remains an unresolved problem.

3.1.1 Developments in seismic response analysis and design of earth retaining structures

Recent studies on seismic response analysis of earth retaining structures can be categorized based on their objectives. In the first category, the soil is studied as an elastic material that seismic waves propagate through it. Efforts in a sub-category of this class of studies provide analytical solutions for evaluating the seismic earth pressures under a seismic event, while others propose a simplified lumped model that acceptably estimates the seismic earth pressures. Studies in the second category account for the mobilization of a soil wedge due to the rupture along the failure surface. The model proposed in this study incorporates state-of-the-art in both categories.

Wood's (1973) study is a turning point in studying soil as an elastic medium. The study proposed a model based on the classical elasticity theory for determining earth pressures on two walls retaining soil resting on a rigid base. Arias et al. (1981) extended Wood's model for anisotropic homogenous soil and using Bessel functions came up with a solution for a semi-infinite backfill. Veletsos and Younan (1994) used a single degree of freedom oscillator

that could replicate results of the mathematically intensive model by Arias. Ostadan's (2005) model incorporated the soil nonlinearity in Veltesos' SDOF oscillator. Brandenberg (2015) accounted for wave propagation effects by using frequency dependent stiffnesses proposed by Kloukinas et al. (2012) and explained conflicting results of Ostadan (2005) and Al Atik et al. (2010).

Use of lumped parameter models to determine the earthquake-induced pressures on the retaining walls began with Scott's (1973) attempt to model a rigid wall on a rigid base using springs attached a shear beam representing the far-field soil column (Figure 3.1 (a)). Veletsos (1994) found the steady state base shear amplitude under a harmonic excitation differs from the one obtained by the analytical solution and resolved this discrepancy by use of a single degree of freedom oscillator (Figure 3.1 (b)). Wolf (1997) came up with a systematic approach for developing lumped parameter models based on the analytically derived frequency-dependent stiffnesses. His frequency independent lumped model (Figure 3.1 (c)) not only could predict earthquake-induced pressures and driving moment but also imitated the frequency response function of the model with frequency dependent stiffness.

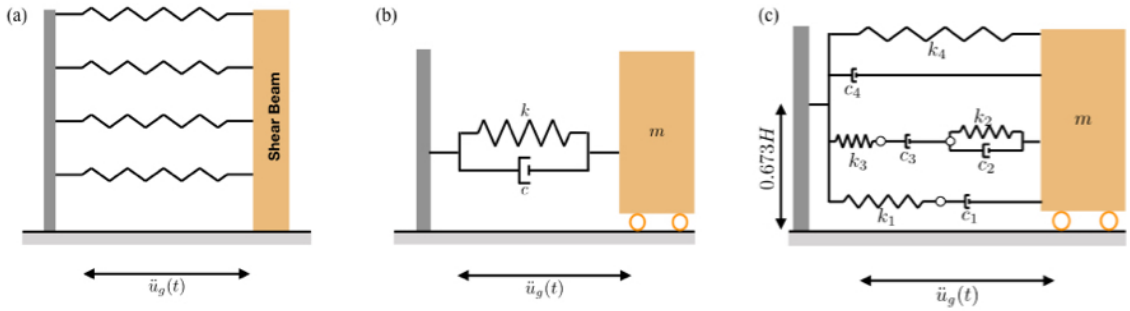

Figure 3.1: (a) Scott's model: shear beam represents the far-field soil column (b) Veletsos (1994) model: employs a SDOF oscillator, (c) Wolf's model: obtained through his systematic approach for developing lumped models.

There are two general approaches for constructing lumped parameter models: the systematic derivation or optimization of parameters. In a systematic procedure, the frequency dependent stiffness (dynamic stiffness function) is rewritten/factorized in terms of ratios of two polynomials. Order and roots of the polynomials determine the configuration and parameters of the equivalent lumped model. Wolf (1994) explains the derivation of such

models for semi-infinite mediums and Wu and Prakash (2001) proposed a model for foundations resting on a half-space using such a systematic approach. This type of lumped models typically predicts frequency response function accurate in all range of frequencies. However, derivation of a such lumped model for more complex problems with layered soil, wall flexibility, etc., is very difficult if not unattainable.

The alternative approach for constructing lumped models is based on the minimization of an objective function to solve for parameters of a pre-sdetermined configuration. The construction of the lumped model begins with choosing a configuration of masses, springs, and dashpots with values to be determined. The objective function is defined as the difference between a reference Frequency Response Function (FRF) (in this case pressure-frequency function), and its counterpart obtained from the lumped model. The reference FRF is achieved either through analytical methods or high-fidelity numerical methods like FEM. By defining the objective function, one can find optimal parameters of the given configuration by employing nonlinear regression techniques.

Seismic earth pressure models involved with the mobilization of a soil wedge fall into two main sub-categories, models with a planar failure surface and those with log-spiral failure surface. M-O method assumes that the failure surface is similar to the one predicted by Coulomb and Rankine earlier. The trial wedge method is basically a numerical implementation of the M-O method that takes the soil cohesion into account. Tolunay and Shields (1973) proposed a limit equilibrium model using Terzaghi's predicted log-spiral shape for failure surface. Marrison and Ebeling (1995) modified Toulnay's limit equilibrium model by accounting for the balance of angular momentum. Shamsabadi et al. (2013) noted that under certain conditions Marrison's model could be non-conservative and proposed a model using the method of slices which is typically used for slope stability analysis.

The method proposed in this study is a lumped model but novel in several aspects. In a sense, the method is an alternative systematic approach meaning the stiffness and dashpot values are obtained systematically but not based on the dynamic stiffness function of the

system. All the above-mentioned lumped parameter models are valid for cases that no soil wedge is mobilized; however, this model incorporates such condition by defining a new element henceforth called fuse. The threshold of this fuse represents the yielding force on the failure surface. Implanting fuses only on strategic locations makes the forthcoming model computationally inexpensive.

3.1.2 Classification of Seismic Analysis Methods

Available methods in literature for seismic analysis of retaining walls can be classified based on employed analysis method (limit equilibrium, finite element, or finite difference), whether they are pseudo-static, pseudo-dynamic, or dynamic. In this section, these different types along with their advantages and shortcomings are explained. Also, summaries of available methods in literature are tabulated in Table 3.1 and Table 3.2 that are updated versions of tables provided by Taylor (2007). The following classification summary heavily borrows from Taylor (2007).

3.1.2.1 Pseudo-Static Methods

A summary of these methods is given in Table 3.1. Methods under this category fall into two subclasses:

Force-Based Methods: In this class of methods, the total static load acting on retaining wall assumed to be a sum of loads imposed by static sources (like gravity or static surcharge) and a pseudo-static seismic load. The horizontal and vertical components of the pseudo-static load are obtained by multiplying the mass of a pre-calculated failing soil wedge with coefficients of horizontal and vertical ground acceleration K_h and K_v. These methods are reported to be too conservative and result in over-design; therefore, codes recommend a lower factor of safety for pseudo-static analysis comparing to static (Taylor (2007). To the best of authors' knowledge, no force based pseudo-static is

capable of estimating wall displacements.

Displacement-Based Methods: These methods are empirical equations resulted from a Franklin and Chang (1977) database developed based on Newmark sliding block analysis. Their proposed equations estimate the wall displacement for accelerations causing the mobilization of a failure wedge. Critical accelerations resulting such limiting conditions are determined using the M-O earth pressure theory. The methods have shown inconsistent estimations for residual wall displacements, mostly because of their empirical basis (Kramer (1996)).

3.1.2.2 Pseudo-Dynamic and Dynamic Methods

These methods are capable of time-history analyses. A summary of these methods is given in 3.2.

Force-Based Methods: Both efforts in this category of retaining wall analyses to some extent rely on principals of pseudo-static methods. Zarrabi (1979) requires the determination of the size of the failure wedge at each time increment. They employ MO theory to carry such pre-processing, therefore preserves MO's over-conservative nature. The method proposed by Steedman and Zeng (1996) also depends on MO theory for calculation of critical rotational acceleration K_{cr}. It further assumes the resultant thrust acts on 1/3 height of the wall which turns out to be inaccurate.

Dynamic Methods: Limit equilibrium models capable of performing dynamic time-history analysis are typically complex. Although the complexity of numerical methods like finite element methods (FEM) and finite difference (FD) are not any less than dynamic limit equilibrium models and are computationally more expensive, they received better attention in commercial engineering tool because of their robustness. The model proposed in this study (Lumped Impedance Model (LIM)), retains the robustness of FEM and FD while reduces the complexity and computational cost by

employing state-of-the-art earth pressure theories in the back-end processes.

Table 3.1: Pseudo-static analysis methods for retaining walls.

Mode of Seismic Load Application	Method	Prescribed Soil Behavior	Analysis Method	Load Derivation	Earth Pressure Theory	Prescribed Failure Mode	Prescribed Point of Application	Output		Dynamic Features Modeled		
								Displacement	Force	Inertial	Soil Damping	Soil Plasticity
Force	Mononobe-Okabe (MO) (1929)	Rigid Plastic	Limit Equilibrium	PGA	MO	Translation/Rocking	N/A	×	✓	×	×	Perfect Plastic
	Wood (1973)	Rigid Plastic	Limit Equilibrium	PGA	MO	Translation/Rocking	0.58H	×	✓	✓	×	×
	Wood and Elms (1990)	Linear Elastic	Limit Equilibrium	PGA	Elasticity Theory	N/A	0.5H	×	✓	✓	×	×
	Mylonakis *et al.* (2007)	Rigid Plastic	Kotter Equations	PGA	Kotter Equations	N/A	N/A	×	✓	×	×	Perfect Plastic
	Simonelli and Penna (2009)	Rigid Plastic	Limit Equilibrium	PGA	MO	Translation/Rocking	N/A	×	✓	×	×	Perfect Plastic
	Shamsabadi *et al.* (2013)	Rigid Plastic	Limit Equilibrium	PGA/V	LSH	Translation	N/A	×	✓	×	×	Perfect Plastic
	Gaudio *et al.* (2018)	Rigid Plastic	Limit Equilibrium	PGA	MO	Translation /Rocking	N/A	×	✓	×	×	Perfect Plastic
Displacement	Franklin & Chang (1977)	Elastic-Plastic	Limit Equilibrium	PGA/V	N/A	N/A	N/A	✓	✓	✓	×	Perfect Plastic
	Richards and Elms (1979)	Rigid Plastic	Limit Equilibrium	PGA/V	MO	Translation	N/A	✓	✓	✓	×	Perfect Plastic
	Whitman and Liao (1985)	Rigid Plastic	Limit Equilibrium	PGA/V	MO	Translation	N/A	✓	✓	✓	×	Perfect Plastic
	Ambraseys and Menu (1988)	Rigid Plastic	Limit Equilibrium	PGA	N/A	Translation	N/A	✓	✓	✓	×	Perfect Plastic
	Jibson (1994)	Rigid Plastic	Limit Equilibrium	Arias Intensity	N/A	Translation	N/A	✓	✓	✓	×	Perfect Plastic
	Pseudo-Static FEM/FD	Any	FEM/FD	PGA	N/A	N/A	N/A	✓	✓	✓	✓	Perfect Plastic

Table 3.2: Pseudo-dynamic and dynamic analysis methods for retaining walls.

Mode of Seismic Load Application	Method	Soil Material Model	Analysis Method	Load Derivation	Earth Pressure Theory	Prescribed Failure Mode	Prescribed Point of Application	Output		Dynamic Features Modeled		
								Displacement	Force	Inertial	Soil Damping	Soil Plasticity
Pseudo-dynamic	Zarrabi (1979)	Mohr-Coulomb	Limit Equilibrium	ATH	MO	Translation	N/A	✓	✓	✓	×	Perfect Plastic
	Steedman and Zeng (1996)	Mohr-Coulomb	Limit Equilibrium	ATH	MO	Rocking	H/3	✓	✓	✓	×	Perfect Plastic
Dynamic	Newmark (1965) 2D	Mohr-Coulomb	Limit Equilibrium	ATH	N/A	Translation	N/A	✓	✓	✓	×	✓
	Elms (2000) 3D	Mohr-Coulomb	Limit Equilibrium	ATH	N/A	Translation	N/A	✓	✓	✓	×	✓
	Miyata and Sugano (2000)	Mohr-Coulomb	Limit Equilibrium	ATH	N/A	Translation	N/A	✓	✓	✓	✓	✓
	Steedman and Zeng (2000)	Mohr-Coulomb	Limit Equilibrium	ATH	N/A	Translation/Rocking	H/3	✓	✓	✓	×	✓
	Chlimintzas (2003)	Mohr-Coulomb	Limit Equilibrium	ATH	N/A	Translation	N/A	✓	✓	✓	×	✓
	FEM/FD	Any	FEM/FD	ATH	N/A	N/A	N/A	✓	✓	✓	✓	✓
	LIM	**Elasto-plastic**	**LIM**	**ATH**	**N/A**	**N/A**	**N/A**	✓	✓	✓	✓	✓

3.2 Development and Verification of the Lumped Impedance Model

The determination of lateral earth pressure behind a retaining wall subjected to a seismic excitation is a problem with a convoluted nature. In order to solve such a complicated problem, many simplifications and idealizations are generally required. Although for certain problem conditions such simplifying assumptions may result in solutions with some acceptable predictive power, most of these solutions are not extendible to an inclusive set of problem conditions. In this chapter, a novel lumped parameter model is proposed that in addition to simplicity, is extendible to a vast extent of retaining wall problems. The distributed lumped model is comprised of elements with physical interpretations; hence, it's easy to implement and extend. Since the backbone of the model relies on the fundamentals of classical elasticity one can customize it for specific inquiries. The model also handles soil nonlinearity by employing an innovative fuse element concept which significantly reduces complexity and computation cost of plastic limit conditions.

The rest of this chapter is organized as follows: a general description of the lumped impedance model; the implementation of the model in the frequency domain is described and verified against available methods in the literature; time-domain implementation of the model for elastic material and verification against finite element simulations; quasi-static nonlinear calibration of the model against) LSH model by Shamsabadi et al. (2013) and the finite element studies by Nakai (1981); full time-domain implementation of the nonlinear model and verification against finite element simulations.

3.2.1 Derivation of The Lumped Impedance Model

The lumped impedance function is a lumped mass-spring system derived from fundamental equations of elasticity. Constructing the lumped impedance model begins with discretizing the soil domain lumped masses (Figure 3.2(a)) which are interconnected by horizontal and shear springs. Figure 3.2(b) shows the generic form of the lumped impedance model. In

addition to masses and springs, the model comprises fuse element, to account for the soil nonlinearity in active/passive limiting conditions; a rigid element, representing the retaining wall; and two base springs, to account for the wall embedment/foundation.

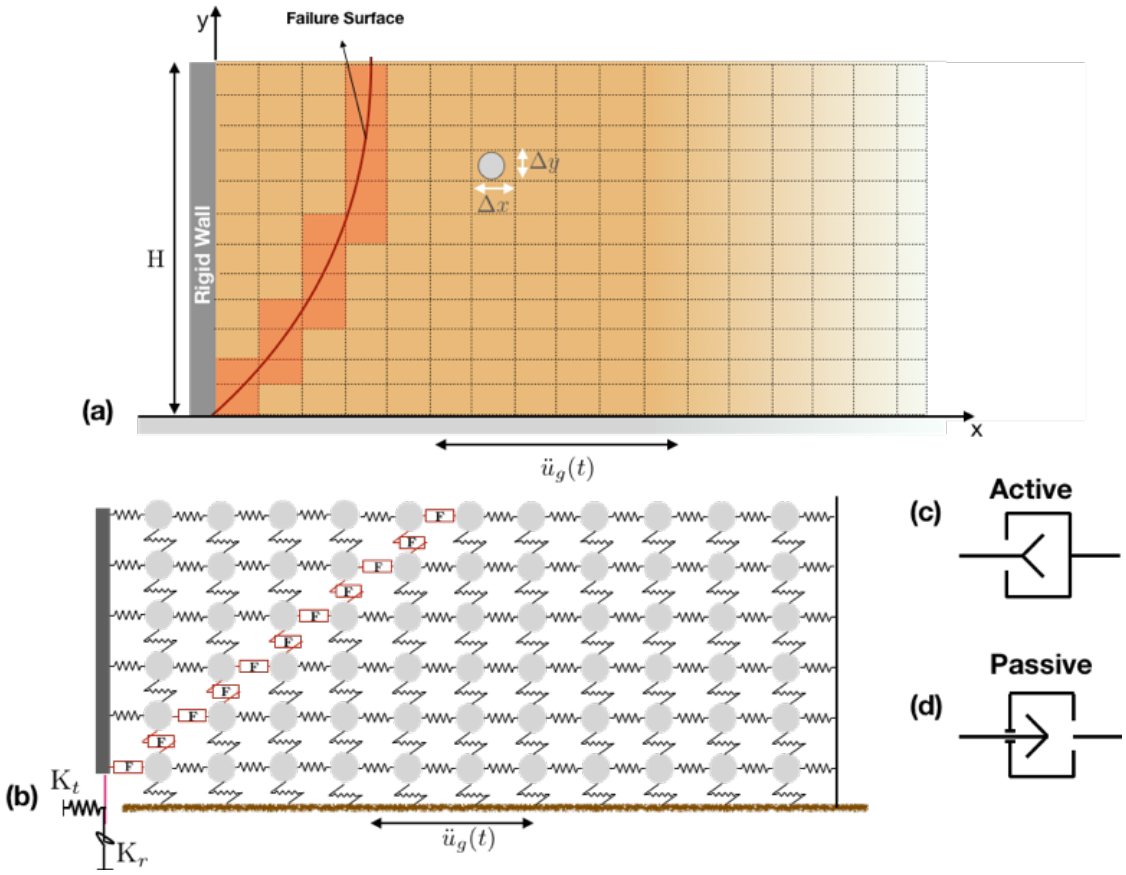

Figure 3.2: (a) Discretization of the soil domain to lumped masses (b) generic schematics of lumped impedance model (c) schematic symbol of active fuse and (d) passive fuse.

Stiffness parameters of the lumped impedance model are obtained through a systematic approach. Parameters of the model are determined directly from the fundamental equations of elasticity assuming plane strain condition. If a rectangular coordinate system of x, y is used as shown in Figure 2 2 the equation of motion may be written in the form of:

$$\rho \frac{\partial^2 u}{\partial t^2} = \frac{\partial \sigma_{xx}}{\partial x} + \frac{\partial \sigma_{xy}}{\partial y} \tag{3.1}$$

Assuming no coupled stresses is developed in the backfill, vertical displacements are zero, and stress components have the following forms, one can derive the equations of motion in terms of displacement.

$$\sigma_{xx} = K_{xx}\frac{\partial u}{\partial x} \tag{3.2}$$

$$\sigma_{xy} = K_{xy}\frac{\partial u}{\partial y} \tag{3.3}$$

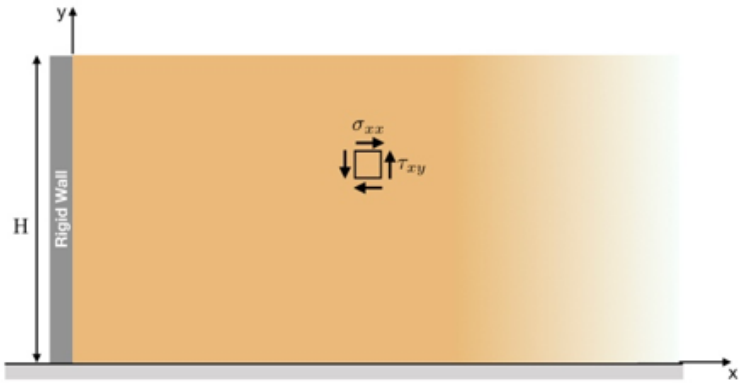

Figure 3.3: Developing the elasticity equation under plane strain assumption.

Also, to account for material damping, it's assumed that there exists a constant ? that relates stiffness values to cohesion values as following:

$$C_{xx} = \kappa K_{xx},\ C_{xy} = \kappa K_{xy} \tag{3.4}$$

Therefore, stress-strain relationships of a cohesive soil are:

$$\sigma_{xx} = K_{xx}\frac{\partial u}{\partial x} + C_{xx}\frac{\partial \dot{u}}{\partial x} \tag{3.5}$$

$$\sigma_{xy} = K_{xy}\frac{\partial u}{\partial y} + C_{xy}\frac{\partial \dot{u}}{\partial y} \tag{3.6}$$

And finally, equation 3.1 can be written as follows:

$$\rho\frac{\partial^2 u}{\partial t^2} = (1 + \kappa\frac{\partial}{\partial t})(K_{xx}\frac{\partial^2 u}{\partial x^2} + K_{xy}\frac{\partial^2 u}{\partial y^2}) \tag{3.7}$$

The proposed formulation represents anisotropic solid, and it resembles classical elasticity if and only if the stiffness values are taken equal to $K_{xx} = E/(1-\nu^2)$ and $K_{xy} = G$ (Arias et al. (1981)). Value of κ can be determined analytically based on characteristics of the soil provided by laboratory tests or can be back-calculated through an optimization process based on a frequency response function. One can also use common methods like Rayleigh's method to account for material damping. But developing a soil damping model is beyond the scope of this work.

To build-up the distributed lumped model, the backfill soil is discretized to a number of elements as depicted in Figure 3.4. A major difference of this lumped parameter model with commonly used lumped models is that the lumped masses represent real segments of the physical domain and it is not just a calibrating parameter. In this sense, the distributed lumped parameter model is similar to the finite element method. This becomes particularly important later in nonlinear lumped impedance model, for implanting the fuses on the failure surface. The model can also be interpreted as dices discretization resembling the concept of slices in LSH model proposed by Shamsabadi et al. (2013).

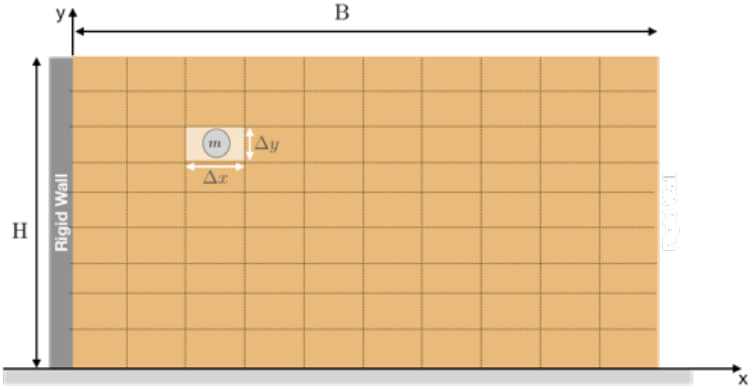

Figure 3.4: Discretization of backfill in order to establish the lumped parameter model.

Before introducing the differentiation scheme, it is necessary to establish a numbering scheme. In this study, we number elements from left to right and bottom to top as shown in Figure 3.4. n_r and n_c stand for the number of elements in each row and each column respectively. Using the central difference scheme the derivatives of displacement u in equation

3.7 can be written in the following form:

$$\frac{\partial u^2}{\partial x^2} = \frac{u_{i+1} - 2u_i + u_{i-1}}{\Delta x^2} \tag{3.8}$$

$$\frac{\partial u^2}{\partial y^2} = \frac{u_{i+nr} - 2u_i + u_{i-nr}}{\Delta y^2} \tag{3.9}$$

By plugging these derivatives into equation 3.7, the governing equation for each lumped mass is obtained:

$$\rho \ddot{u}_i = K_{xx} \frac{u_{i+1} - 2u_i + u_{i-1}}{\Delta x^2} + K_{xy} \frac{u_{i+nr} - 2u_i + u_{i-nr}}{\Delta y^2} \tag{3.10}$$

In order to isolate the mass on the left side of the equation we can multiply both sides with Δx and Δy terms:

$$m_i \ddot{u}_i = K_{xx} \frac{\Delta x}{\Delta y} (u_{i+1} - 2u_i + u_{i-1}) + K_{xy} \frac{\Delta y}{\Delta x} (u_{i+nr} - 2u_i + u_{i-nr}) \tag{3.11}$$

Hereby, we derive the equilibrium equation of the ith mass from its free body diagram in order to determine the stiffness parameters of the LIM. Figure 3.5 shows the free body diagram of a lumped element assuming no body force. The equilibrium of forces in x-direction will results in:

$$m_i \ddot{u}_i = K_h (u_{i+1} - 2u_i + u_{i-1}) + K_s (u_{i+nr} - 2u_i + u_{i-nr}) \tag{3.12}$$

One by one correspondence of equations 3.11 and 3.12 results in:

$$K_h = K_{xx} \frac{\Delta y}{\Delta x} = \frac{E}{(1 - \nu^2)} \frac{\Delta y}{\Delta x} \tag{3.13}$$

$$K_s = K_{xy} \frac{\Delta x}{\Delta y} = G \frac{\Delta x}{\Delta y} \tag{3.14}$$

By determining the stiffness parameters of the model, one can assemble the stiffness matrix of the multi-degree of freedom system to perform calculations in frequency and time-

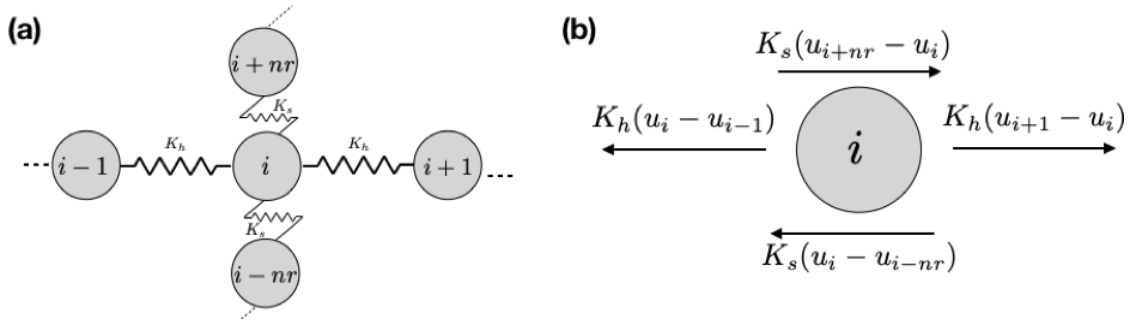

Figure 3.5: (a) the general connectivity of a lumped mass, (b) the free-body diagram of a typical lumped element.

domain. A significant advantage of the lumped impedance model over finite element model is that it does not require numerical integrations for assembling matrices which notably reduces the computational costs of simulations. Comparing to the finite difference method, the perspective that LIM provides reduces the complexity of formulation by providing physical interpretation of differentiation schemes, and makes the extendibility of the model significantly simpler especially in case of nonlinearities.

3.2.2 Frequency Domain Model

To establish a verification process for the lumped impedance model, in this section the implementation of the model for a rigid wall subjected to harmonic excitation is discussed. To establish a valid comparison with Arias et al. (1981) and Veletsos and Younan (1994), It is further assumed that the wall rests on a rigid base retaining a homogenous soil. Although at the far-field boundary a fixed boundary condition is assumed, to assure negligibility of effects of such simplifying assumption the far-field is placed far enough. Following the formulation and verification studies of the frequency response is provided.

3.2.2.1 Formulation

After assembling mass, damping and stiffness matrices of the LIM once can perform frequency domain analysis to identify the response spectrum of the system under harmonic loads. Under

a base excitation (shown in Figure 2 5), the governing equation can be rewritten as follows:

$$\mathbf{M}(\ddot{u} - \ddot{u}_g) + \mathbf{C}\dot{u} + \mathbf{K}u = 0 \tag{3.15}$$

where **M**, **C**, and **K** are mass, damping and stiffness matrix of the LIM, u is the vector of lumped elements displacements, and $\ddot{u}_g$ is the base acceleration. Under a harmonic excitation, the frequency domain formulation of the latter equation is obtained by taking Fourier transformation:

$$-\mathbf{M}\omega^2 u + \mathbf{C}(i\omega)u + \mathbf{K}u = -\mathbf{M}u_g\omega^2 \tag{3.16}$$

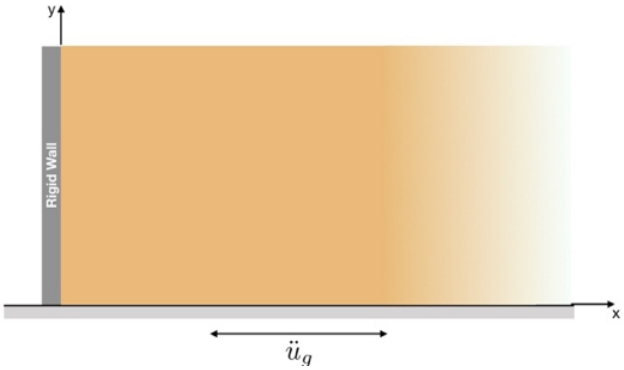

Figure 3.6: A retaining wall resting on rigid base and retaining a homogenous backfill subjected to a base excitation.

3.2.2.2 Verification

Veletsos and Younan (1994) provided an analytical solution for determining dynamic pressures and associated forces induced by ground acceleration to a rigid retaining wall resting on a rigid base retaining a semi-infinite homogenous layer of soil. This analytical method is based on the solution of the coupled system of partial differential equations of motion for the backfill medium with stronger assumptions than those used by Arias et al. (1981). The LMI model is verified against Veletsos?s analytical solution as well as his equivalent lumped parameter models.

Veletsos and Younan (1994) also developed two lumped parameter models (Figure 3.7) in an attempt for resolving shortcomings of Scott?s shear beam model. In a version of their lumped model, parameters of the model are frequency independent while the other version stiffness and damping parameters are frequency dependent. As will be shown later in verification studies, both models provide a relatively reasonable approximation of the analytical solution.

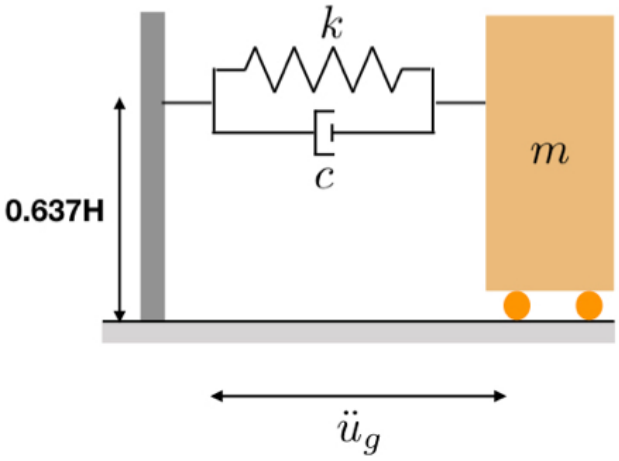

Figure 3.7: The lumped parameter model proposed by Veletsos and Younan (1994).

In the constant parameter model, the value of the stiffness is determined such that the undamped frequency of the system equals the fundamental frequency of the backfill idealized as a series of vertical shear beams. In the frequency dependent version of their lumped model, the values of stiffness and damping are defined as calibrated functions of frequency that minimizes the difference between the lumped model response and the exact analytical formulation.

In Figure 3.8 the base shears calculated by analytical solution per Veletsos and Younan (1994) are plotted against the those of the lumped impedance model. The discretization causes some unwanted damping modes. To eliminate effects of those modes a negligible amount of numerical damping ($\kappa = 1e - 5$) is added to the lumped impedance model for undamped case. As the figures show, the lumped impedance model estimates the maximum base shear precisely although it the natural frequency of the LIM is insignificantly less than the exact model. The LIM generally underestimates the based shear under high-frequency

harmonic excitations. In the undamped case, the LIM shows a pick at normalized frequency $\omega/\omega_1 = 3$ while it is not able to accommodate the sharp spike seen in the analytical solution.

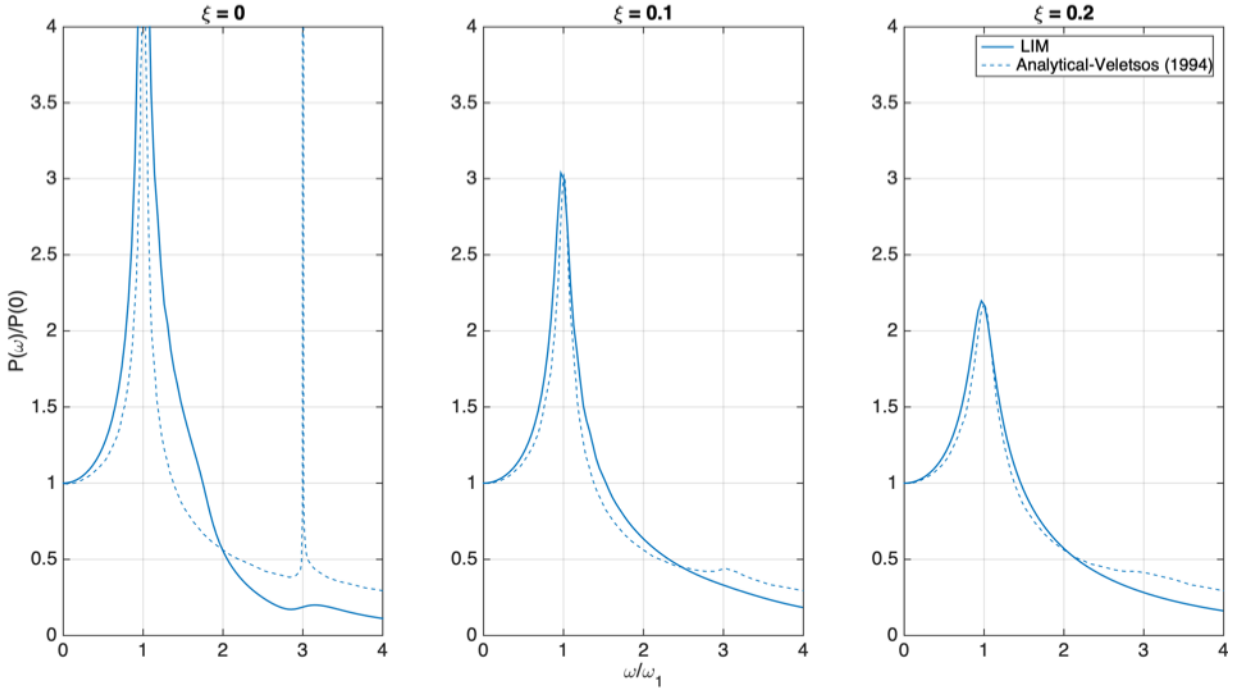

Figure 3.8: Comparison of frequency response of the lumped impedance model versus the analytical solution by Veletsos and Younan (1994).

In another comparison, the LIM is compared with both frequency dependent and constant value parameter lumped models proposed by Veletsos and Younan (1994). Generally, all the three models show an acceptable performance in estimating the maximum base shear and the first natural frequency. Both lumped parameter models proposed Veletsos and Younan (1994) underestimate the high-frequency responses like LIM. In fact, in the high-frequency region, the LIM outperforms those lumped models (Figure 3.9).

The amplitude of the reaction moment can be expressed as the product of the base-shear reaction and the height of the point of the application. In Figure 3.10 the calculated point of application using the LIM is compared with the exact solution. Except for the undamped case, the point of application is predicted about $0.6H$ where H is the height of the wall. To capture the moment, Veletsos and Younan (1994) chose (2/?)H=0.637H as the point of application for their lumped models (Figure 3.7).

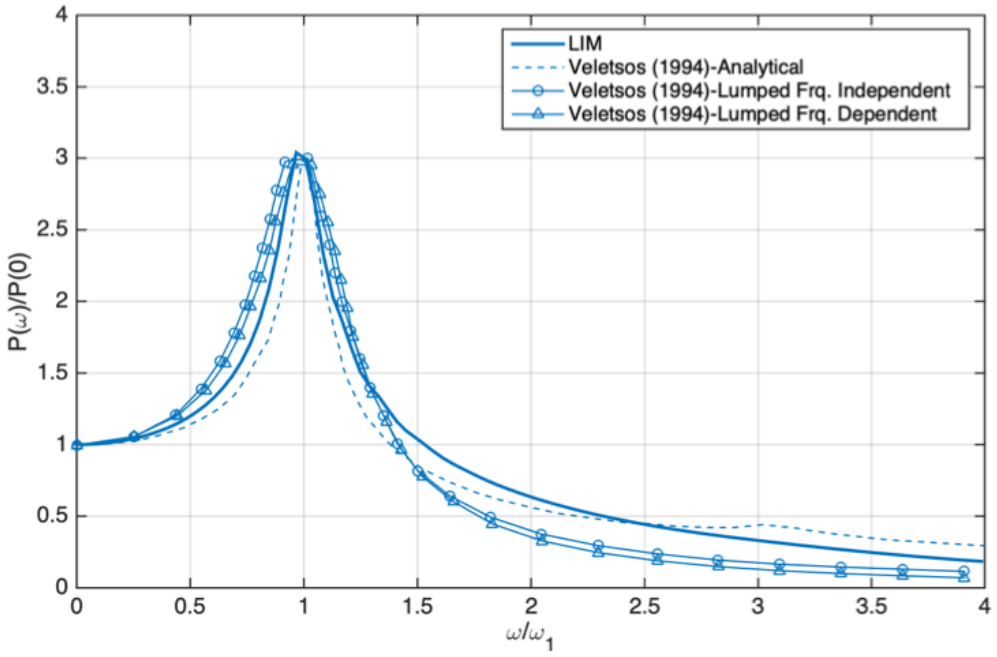

Figure 3.9: The frequency response estimated by lumped impedance model versus constant value lumped model, frequency dependent lumped model, and the analytical model by Veletsos and Younan (1994).

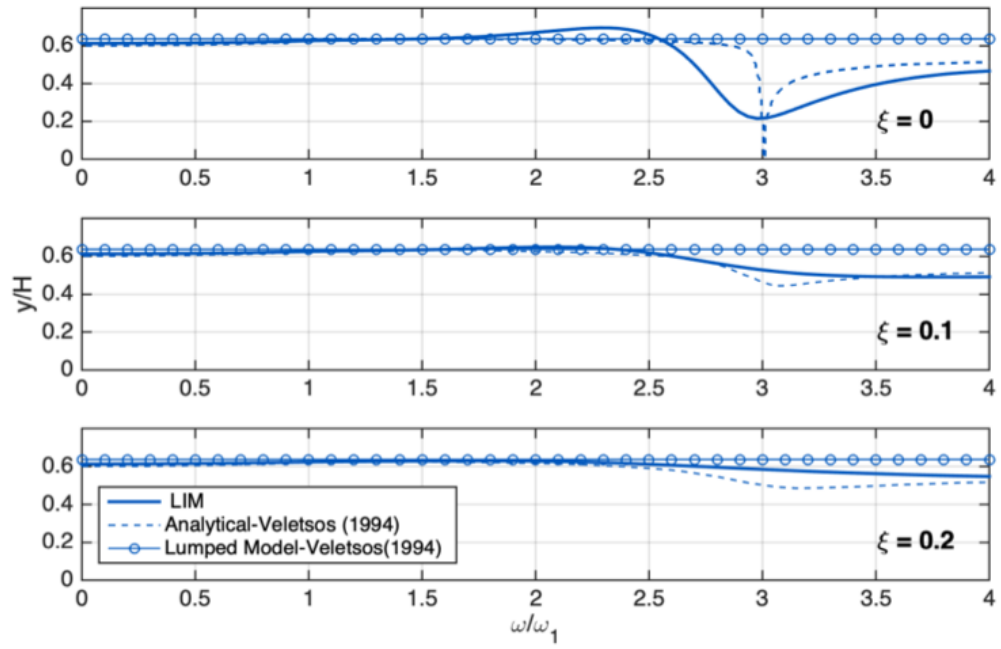

Figure 3.10: The comparison of height of the point of application using the LIM and Veletsos analytical solution and lumped model.

3.2.3 Time-Domain Elastic Model

In the following section, the implementation of the LIM in the time-domain for a rigid cantilever wall embedded in an elastic foundation soil and retaining an elastic backfill soil is elaborated. The system is subjected to a ground motion from the bottom boundary of the foundation soil. Figure 3.11 (a) shows the general configuration of a cantilever wall of height H and with embedment depth H$_e$*mb*. The problem is simplified in LIM as a rigid wall of height H resting on two base springs accounting for translational (K_t) and rocking stiffness (K_r) of the embedment. A transfer function is used to convert the bedrock shaking time-history to the shaking time-history at the embedment level. For verification studies in this chapter, the LIM is utilized to determine such transformation.

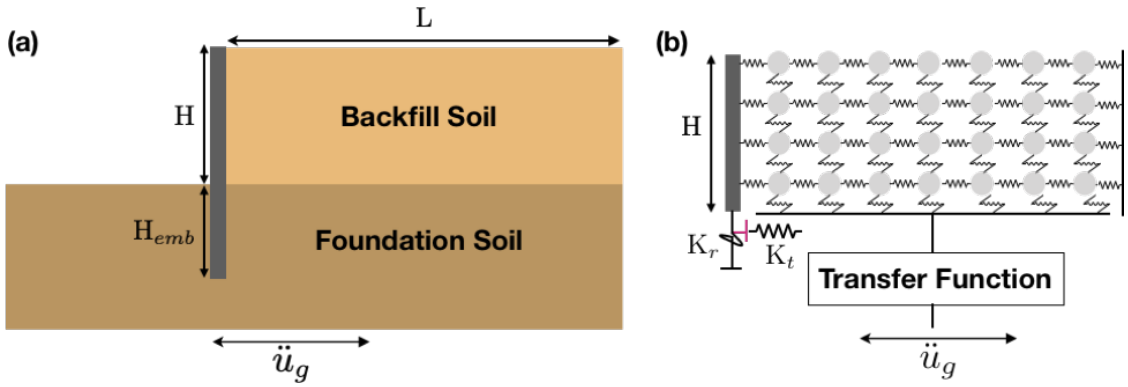

Figure 3.11: (a) A generic configuration of a cantilever wall problem. (b) The idealized equivalent LIM.

The time-domain implementation of the LIM using the Newmark time-stepping scheme is the first step toward the implementation of the full elastoplastic model in the time-domain. For elastic backfill material, linear Newmark time-stepping is employed as springs behave linearly throughout time-history excitations. In following sections, use of nonlinear Newmark time-stepping for handling elastoplastic backfills is explained. Subsequent to the derivation of the LIM in the time-domain for elastic backfill, it has been verified against several finite element simulations.

3.2.3.1 LIM Setup and Formulation

In the time-domain formulation of the LIM the mass, damping and stiffness matrices are assembled as explained in section 3.2. The far-field boundary (the side of soil domain located opposite to the wall) is assumed to be fixed and to assure negligibility of effects of such truncation this boundary should be located at sufficiently far distance of the wall. To impose shaking boundary condition, all the elements at the bottom boundary are connected to the ground degree-of-freedom. The displacement of the ground degree-of-freedom is prescribed by the transfer function which transfers the ground motion from bedrock depth to wall depth.

The values of translation stiffness K_t and the rocking stiffness K_r are calibrated to optimize results LIM methodology. It is assumed that the interactions of the embedment and the soil are frequency independent. This simplifying assumption is essentially similar to the effort by Gazetas and Roesset (1976) for developing the closed-form equation for stiffness of a rigid strip footing. Although in extensions of LIM a solution for avoiding such simplification is recommended (see section **XXX**).

The governing equation of the time-domain model has the form of:

$$\begin{bmatrix} \mathbf{M_f} & 0 \\ 0 & \mathbf{M_p} \end{bmatrix} \begin{bmatrix} \ddot{u}_f(t) \\ \ddot{u}_p(t) \end{bmatrix} + \begin{bmatrix} \mathbf{C_{ff}} & \mathbf{C_{fp}} \\ \mathbf{C_{pf}} & \mathbf{C_{pp}} \end{bmatrix} \begin{bmatrix} \dot{u}_f(t) \\ \dot{u}_p(t) \end{bmatrix} + \begin{bmatrix} \mathbf{K_{ff}} & \mathbf{K_{fp}} \\ \mathbf{K_{pf}} & \mathbf{K_{pp}} \end{bmatrix} \begin{bmatrix} u_f(t) \\ u_p(t) \end{bmatrix} = \begin{bmatrix} 0 \\ 0 \end{bmatrix}$$

where the u_f and u_p are the displacement vectors corresponding to free degrees of freedom and prescribed degrees of freedom respectively. In most cases the rotation calculated by FEM were negligible and due to the wall flexibility, therefore, in the rest of this document, the rocking degree of freedom assumed to be fixed unless mentioned. The rest of degrees of freedom including wall translational displacement are set to be free.

Subsequent to assembling and partitioning the matrices, and defining the time-histories of prescribed degrees of freedom, one can employ the linear Newmark?s time-stepping scheme to solve for $u_f(t)$:

$$u_f^n = u_f^{n-1} + du \tag{3.17}$$

$$du = \mathbf{K_{ff}}^{-1}\left((\frac{1}{\beta\Delta t}\mathbf{M}_f + \frac{\gamma}{\beta}\mathbf{C_{ff}})\dot{u}_f^{n-1} + (\frac{1}{2\beta}\mathbf{M_f} + \Delta t(\frac{\gamma}{2\beta} - 1)\mathbf{C}_{ff})\ddot{u}_f^{n-1} + \mathbf{C_{fp}}\dot{u}_p^n + \mathbf{K_{fp}}u_p^n\right) \tag{3.18}$$

$$\dot{u}_f^n = \dot{u}_f^{n-1} + \frac{\gamma}{\beta\Delta t}du - \frac{\gamma}{\beta}\dot{u}_f^{n-1} + \Delta t(1 - \frac{1}{2\beta})\ddot{u}_f^{n-1} \tag{3.19}$$

$$\ddot{u}_f^n = \ddot{u}_f^{n-1} + \frac{1}{\beta\Delta t^2}du - \frac{1}{\beta\Delta t}\dot{u}_f^{n-1} - \frac{1}{2\beta}\ddot{u}_f^{n-1} \tag{3.20}$$

where β and γ are Newmark time-stepping constants.

To implement the transfer function, the same procedure must be done. After assembling matrices of soil sublayers, one can prescribe the displacement of the bottom boundary (input of the transfer function) and read the displacement time-history at the wall depth (output of the transfer function). The output of this transfer function is fed to the system of the wall and the backfill as the prescribed displacement time-history of the ground degree of freedom. The transfer function in LIM configuration is intended to accommodate more sophisticated site-response techniques.

3.2.3.2 FEM Setup and Verification

To verify the time-domain implementation of the LIM for elastic backfill material, a series of finite element simulations are conducted using ABAQUS. In these simulations, an elastic concrete cantilever wall of height 7 meters and with 0.45 meters width retains an elastic material (Figure 3.12). The wall is embedded in an elastic soil with 5 meters embedment depth. The domain is truncated at 35 meters from each side of the wall. The depth of each soil layer is 7 meters and soil properties are listed in Table 3.3. An input time-history displacement is prescribed at the bottom boundary. The interface of the wall and the soil is modeled using a contact element which behaves hard in the normal direction and in tangential direction uses a penalty constraint with 0.3544 friction coefficient.

Table 3.3: Material properties used in ABAQUS simulations.

	Soil 1 Backfill	Soil 2 Sublayer	Concrete	Unit
Density	1600	1900	2400	kg/m^3
Young's Modulus	2e+7	4e+7	2.056e+10	N/m^2
Poisson's Ratio	0.35	0.3	0.2	

The wall and both soil layers are meshed using the ABAQUS 4-node bilinear plane-strain quadrilateral mesh element CPE4R with reduced integration and hourglass control. The soil mesh near the wall is refined to assure the accuracy of the wall-soil contact behavior. The wall height is discretized by 48 elements (4 elements per meter) and the width is discretized by 6 elements. The model consists of two steps, a quasi-static load step for enforcing the gravity and a dynamic step for imposing the ground motion. All tolerance defaults of ABAQUS assumed to be sufficiently accurate for all models. Maximum time step values were adjusted to assure the smoothness of the projected result.

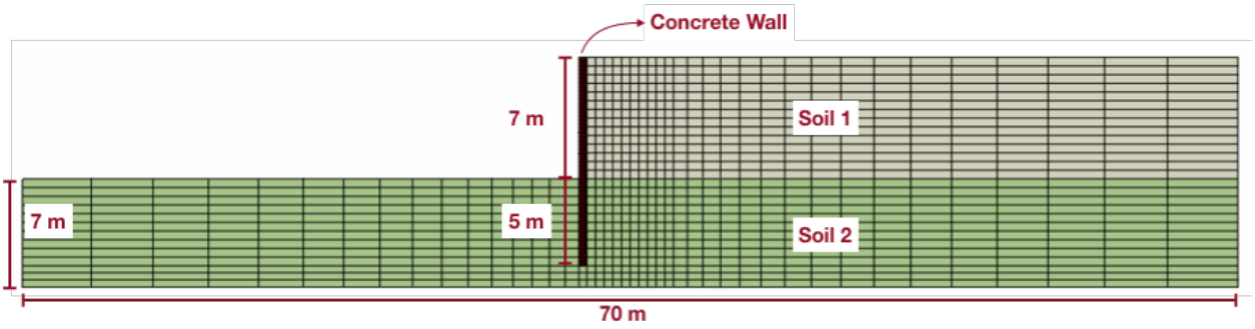

Figure 3.12: The finite element simulation of a cantilever wall.

Sine-Dwell Excitation: In the first series of simulations, the imposed ground motions had the sine-dwell form. The sine-dwell excitations enable us to understand the behavior of the cantilever wall under a quasi-harmonic excitation with varying amplitudes. For each frequency of our series of sine-dwell excitations, the ground motion time-history begins with three periods of rest followed by 10 periods with ascending amplitude. After the first thirteen

periods the signal reaches to its maximum amplitude and hold the amplitude for another 20 periods and after 10 periods of descending it returns to rest state. The simulations are stopped after 46 periods giving the system another three periods for free-vibration and returning to the rest (Figure 3.13).

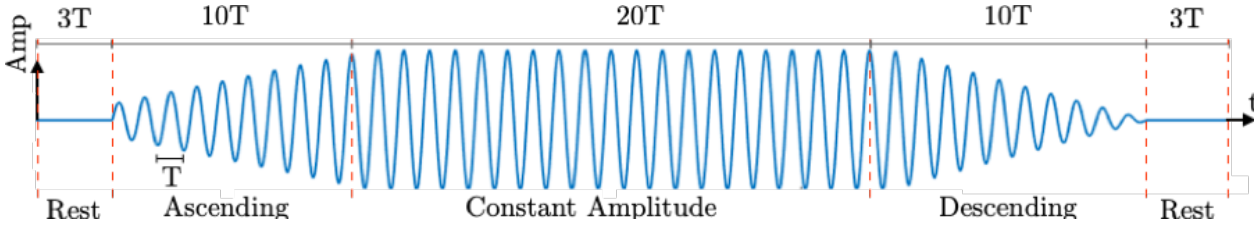

Figure 3.13: Sine-dwell displacement time-histories used for FE simulations.

Three sine-dwell displacement time-histories with frequencies 0.07 Hz, 0.24 Hz, and 2 Hz and amplitude 0.1 m are chosen for the purpose of this verification study. Amplitude is chosen based on the maximum amplitude of the El Centro displacement time-history. The 0.07 Hz excitation represents the first peak in El Centro frequency content (Figure 3.14), and 0.24 Hz represents the last tangible peak frequency in El Centro. The excitation with 2 Hz frequency is employed to verify the response of the LIM for high-frequency values. To assure the smoothness of the simulations the maximum time-step equals 1/16 of the period of the excitation. Both dimensions of the backfill have been discretized to 20 elements in the LIM simulation.

The translational stiffness K_t is a frequency dependent value as the embedded part of the wall, and the wall interface interacts with the surrounding soil in different ways at different frequencies. In this study, K_t has been calibrated for different frequencies. The calibrated translation base stiffness K_t in these simulations are 4.86e+7, 5.01e+7, 7.31e+6 N/m for 0.07, 0.24 and 2.00 Hz excitation frequencies. A solution to this issue will be discussed more in section 3.4.2 wherein potential future extensions of the LIM are described.

The estimated wall displacement, thrust, and moment time-histories by LIM are compared with the FEM simulations in Figure 3.15. Displacement time-histories shows a close agreement of the results between the models. The oscillations in force and moment time-

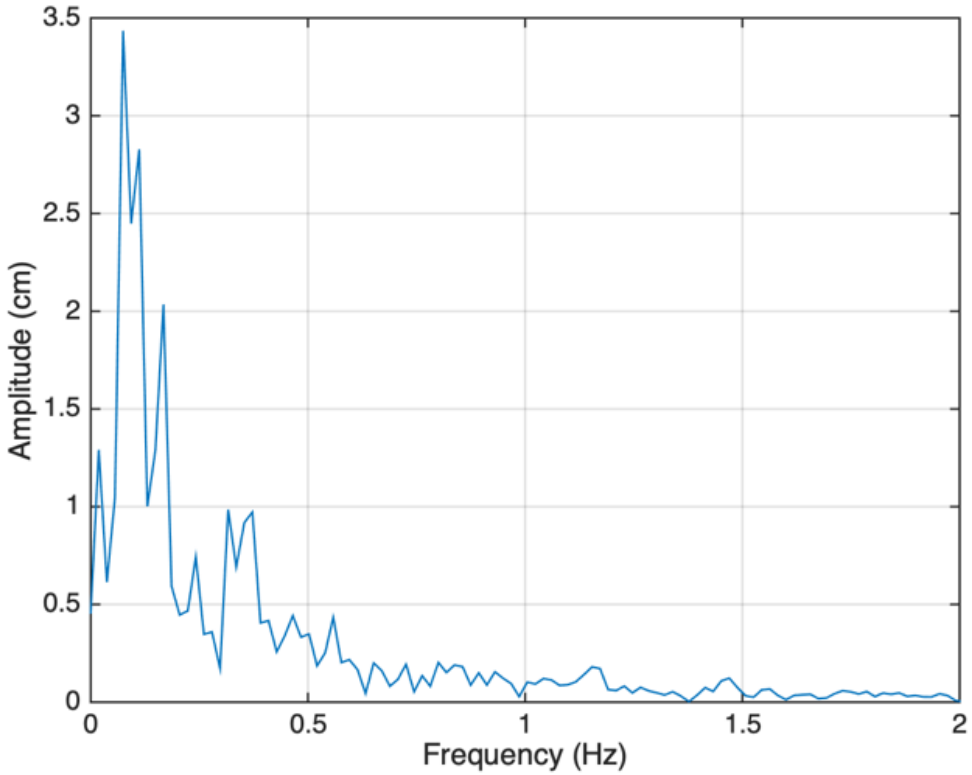

Figure 3.14: Frequency content of the El Centro Record.

histories for the higher frequencies in the LIM are due to the difference of the bottom truncation boundary. As the bottom truncation boundary in LIM is a Dirichlet (displacement) type, there is some energy trapped in the backfill soil while in the FEM model this energy is distributed in the foundation soil as well. To alleviate the effects of these reflections, in Figure 3.16 a small numerical damping is added to the model using $\kappa = 5e-3(\xi < 1\%)$. The figure also shows that the LIM overestimates the moment in higher frequencies. This overestimation is mainly due to the idealization of the FEM flexible wall as a rigid wall in LIM.

Broadband (El Centro) Excitation To verify the predictive ability of the LIM for a wide range of frequencies, the aforementioned retaining wall studied when it is subjected to El Centro displacement time-history. The calibrated base translational stiffness for this verification study is 2.70e+7 N/m. The response time-histories are plotted in Figure 2 16. The over-predicted value of the moment is due to the idealization of the wall as a rigid plate

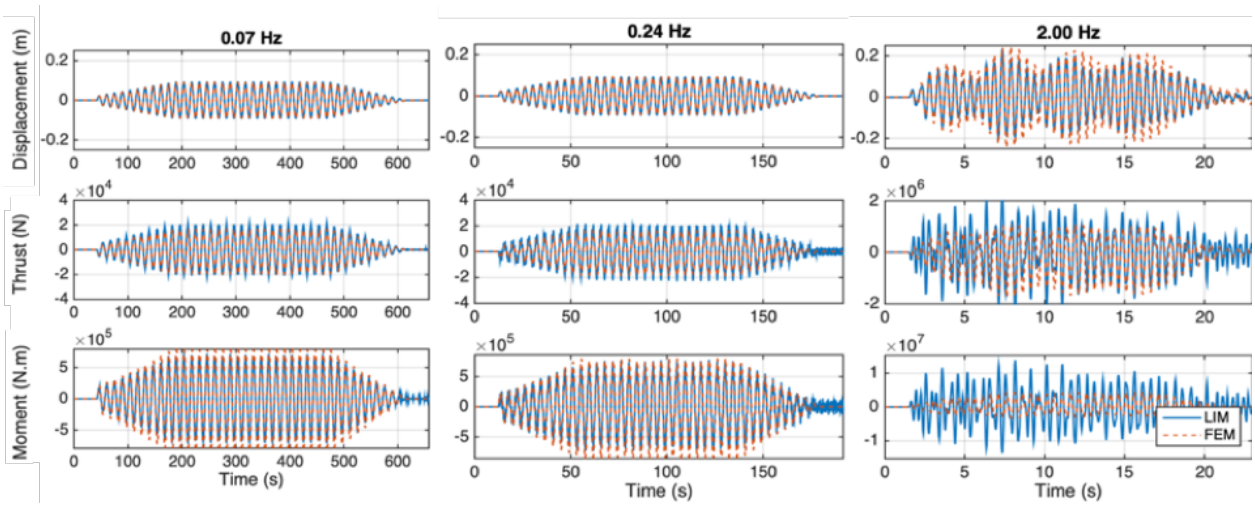

Figure 3.15: Verification of LIM wall displacement, thrust, and moment time-history against ABAQUS FEM simulations for the example retaining wall subjected to sine-dwell excitation.

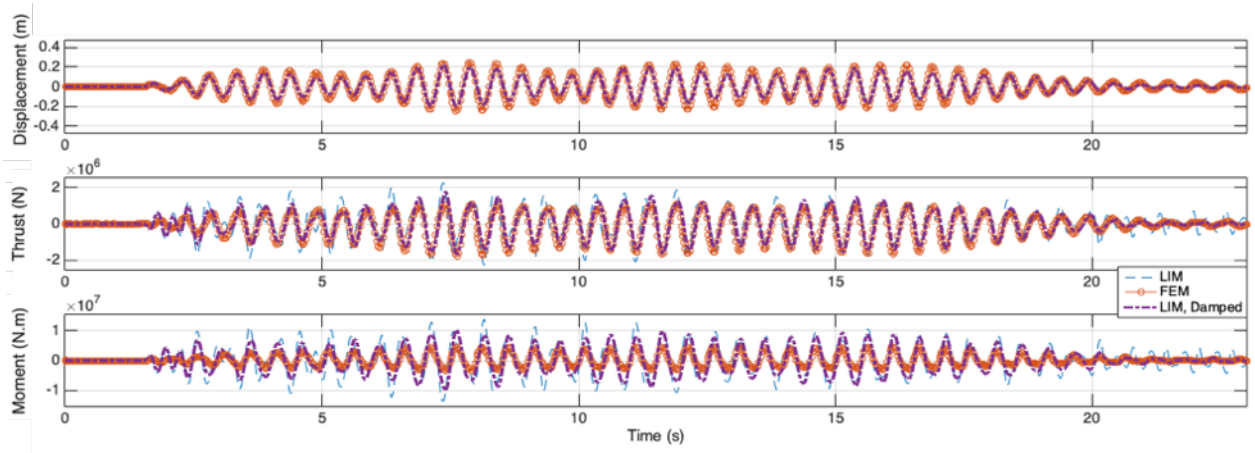

Figure 3.16: The added numerical damping eliminates the effects of the trapped energy due to bottom truncation boundary.

in LIM.

3.2.4 Full time-domain elastoplastic model

To investigate the applicability of the LIM in passive and active limit conditions, the implementation of LIM for elasto-plastic backfill material is discussed in this section. This implementation accounts for soil nonlinearity using the innovative fuse element. The fuse element is an elastic-perfectly plastic element which controls the behavior of the backfill

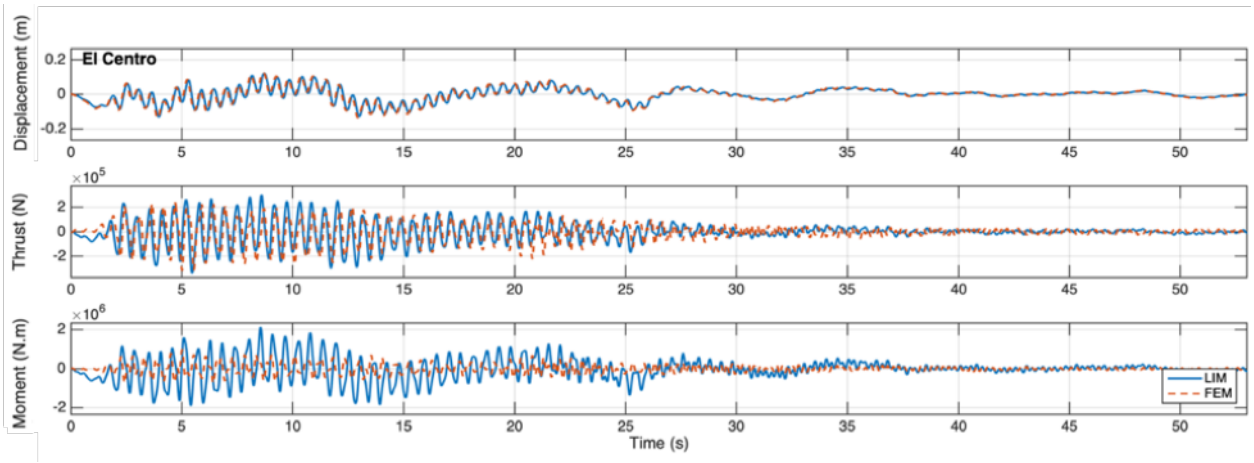

Figure 3.17: Verification of response time-history estimated by LIM against ABAQUS FEM for the example retaining wall subjected to El Centro recorded time-history.

when a failure wedge is mobilized. The active and passive capacities are controlled using the yielding force of these fuse elements calibrated using LSH model by Shamsabadi et al. (2013).

The fuse elements are placed in strategic locations and their strength are calibrated to capture the force-displacement curves proposed by well-known limit equilibrium models. LIM employs a log-spiral shape failure surface calculated by LSH limit equilibrium model proposed by Shamsabadi et al. (2013) or the classic Rankin failure surface. In a sense, quasi-static implementation of LIM is an extension of LSH limit equilibrium model proposed by Shamsabadi et al. (2013) which considers vertical discretization in addition to the horizontal discretization of the backfill.

3.2.4.1 LIM Setup and Formulation

After assembling the general connectivity of the elements, the springs corresponding to the elements on the failure surface are replaced with the fuse element (Figure 2 17). Fuse elements on the active failure surface behave linear elastic in compression and have an elasto-plastic behavior in tension. On the other hand, fuse elements on the passive failure surface have an elasto-plastic behavior in compression and elastic behavior in tension. For the purpose

of the time-domain analysis of retaining walls, passive fuse elements will not be necessary, as it is impossible for these fuses to be mobilized in a seismic event. However, the passive elements can be used to analyze abutment backwall behavior.

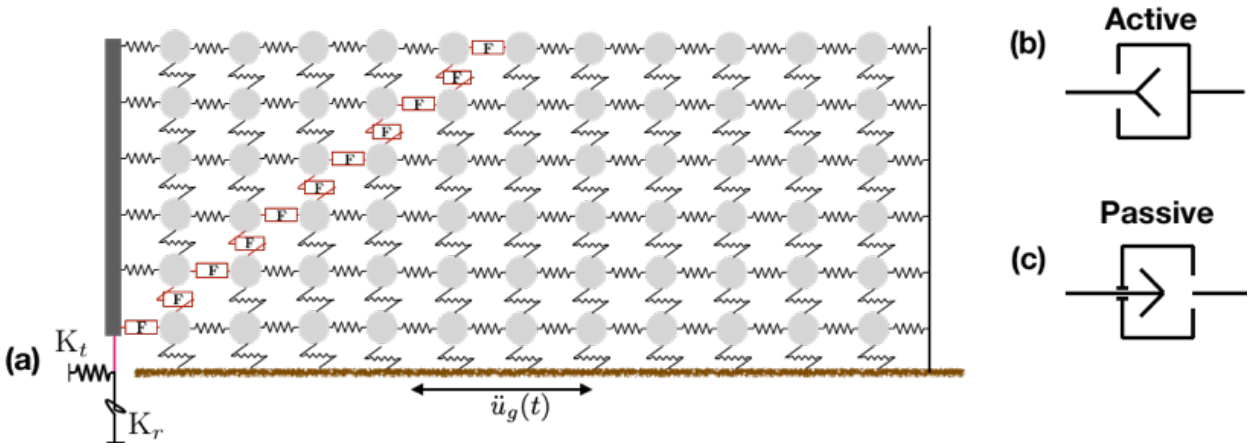

Figure 3.18: (a) placing the fuse elements on strategic locations determined by the failure surface calculated by LSH model. (b) the schematic of the active fuse element. (c) the schematic of the passive fuse element.

Determination of the force and permanent elongation of the fuse element requires knowledge of the fuse endpoints displacements $\{u\}$, rest length of the fuse (reference elongation of the fuse) L_{ref}, the yielding force of the fuse F_y, and its stiffness K as reflected in the flowchart in Figure 3.19. The F_y is material dependent strength parameter determined using LSH method by Shamsabadi et al. (2013), and the stiffness K is equivalent to the spring stiffnesses determined by LIM. Reference length L_{ref} is initialized with zero and changes when some plastic deformation is mobilized in the fuse and defines the displacement state for which the fuse is at rest (zero force).

The effective elongation ΔL which causes mobilization of some force in the fuse is the difference of the endpoints displacement and the reference length L_{ref}. In the following flowchart, a temporary value of force is determined assuming the fuse remains in elastic regime F_t. If this assumption is correct, there is no need for further calculation of the force, and the Jacobian of force between endpoints of the fuse equals the stiffness of the fuse. Otherwise, if F_t exceeds the yielding force, the fuse force equals $\mp F_y$ (signs correspond to passive/active behaviors respectively), and Jacobians of the endpoints will be zero. In this

case, the reference length needs to be updated to reflect the permanent elongation of the fuse.

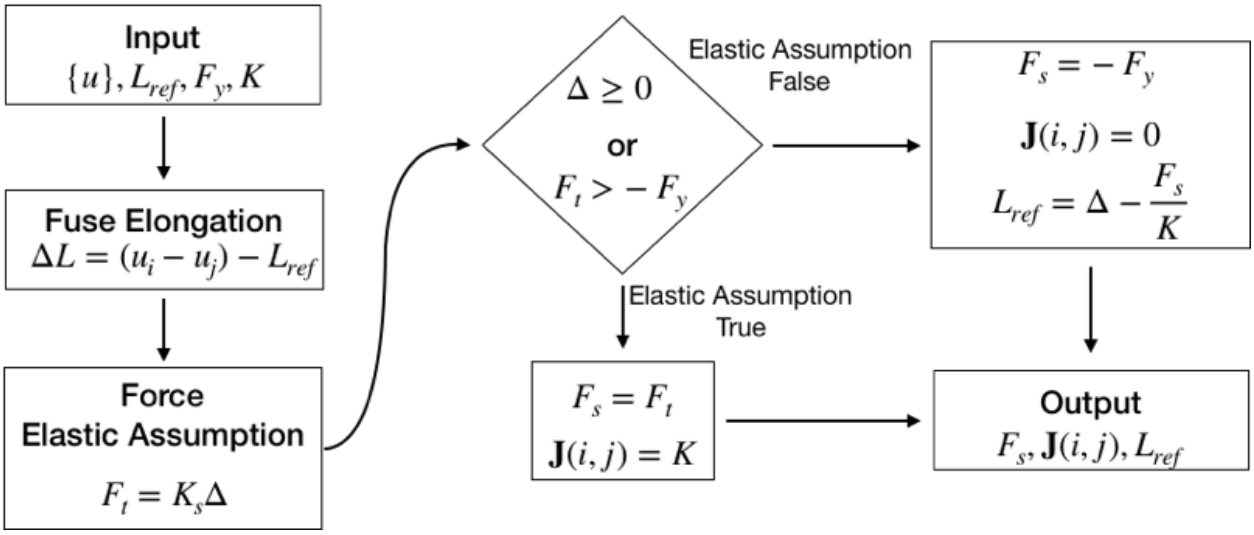

Figure 3.19: Flowchart of the determination of the force and permanent elongation of an active fuse element for a given displacement array.

Figure 3.20 shows the generic force-displacement behavior of the active fuse element. Initially, there is no permanent elongation in the fuse, and in compression, it behaves like simple spring. However, if the active fuse is stretched enough until it reaches its capacity F_y (at elongation ($\Delta = \Delta_y$), it begins deforming without gaining more force (Figure 3.20 (a)). After such plastic deformation, the permanent elongation of the fuse L_{ref} defines the zero-force state (Figure 3.20 (b)), and compression only happens when $(u_i - u_j) > L_{ref}$ (Figure 3.20 (c)). The passive fuse shows the same behavior only in the opposite direction.

In the quasi-static active/passive scenarios the wall displacement slowly increases throughout the simulation time, and the ground degree of freedom and the far-field boundary are fixed. In the nonlinear LIM, the restoring force vector provided by springs and fuses is a nonlinear function of displacements $r = r(u)$. Therefore, to solve for free degrees of freedom, the nonlinear Newmark time-stepping must be used. In nonlinear Newmark time-stepping, displacements of the free DOFs at each step u_f^n, are calculated by adding a differential

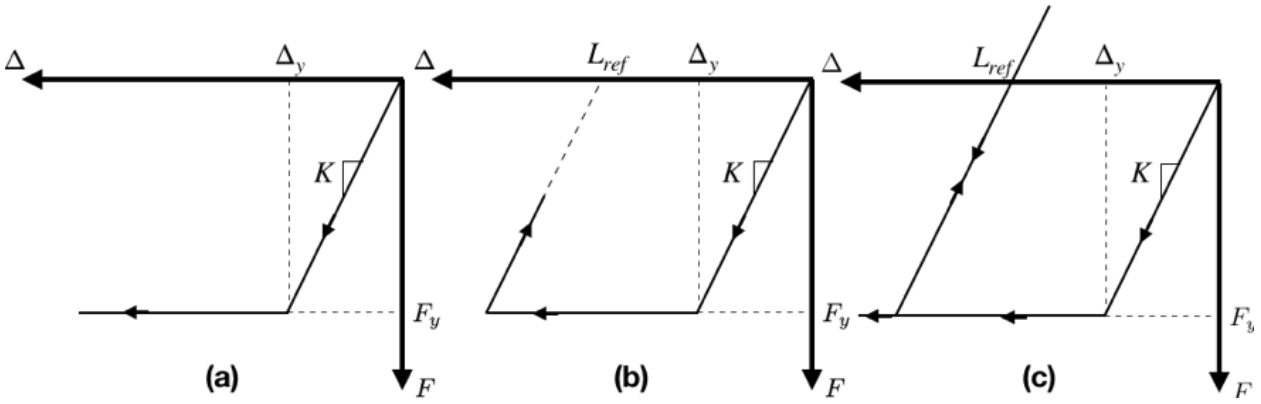

Figure 3.20: Generic behavior of the active fuse element. (a) loading the fuse element until it reaches its capacity (b) unloading after plastic deformation (c) compressing the fuse element.

displacement du to displacement at the previous step u_f^{n-1}:

$$u_f^n = u_f^{n-1} + du \tag{3.21}$$

where du is determined through corrector-predictor iterations:

$$du_i = du_{i-1} - \hat{K}_T \epsilon_{i-1} \tag{3.22}$$

where $\hat{K}_T$ is the effective tangent stiffness and ϵ_{i-1} is residual unbalanced force vector based on the predicted du_{i-1}. The effective tangent stiffness is calculated based on the predicted value of du_i as follows:

$$u_i^* = u_f^n + du_i \tag{3.23}$$

$$A = \frac{1}{\beta}\Delta t \mathbf{M_f} + \frac{\gamma}{\beta}\mathbf{C_{ff}} \tag{3.24}$$

$$B = \frac{1}{2}\beta \mathbf{M_f} + \Delta t \frac{\gamma}{2\beta - 1}\mathbf{C_f f} \tag{3.25}$$

$$\hat{K}_T = \frac{1}{\Delta t} A + \mathbf{J}_\epsilon(u) \tag{3.26}$$

where the $\mathbf{J}_\epsilon(u)$ is the Jacobian of the residual unbalanced force vector with respect to

element displacements. If elements p and q are connected by conventional springs $[\mathbf{J}_\epsilon(u)]_{pq}$ equals to the spring stiffness, otherwise, if they are connected by a fuse element with stiffness K and yielding displacement Δ_y the Jacobian is determined by:

$$[\mathbf{J}_\epsilon(u)]_{pq} = [\frac{\partial \epsilon_p}{\partial u_q}] = \begin{cases} K & \Delta_{pq} \geq \Delta_y \\ 0 & \Delta_{pq} < 0 \end{cases} \tag{3.27}$$

where $\Delta_p q$ is the elongation of the fuse element connecting elements p and q. In other words, $\mathbf{J}_\epsilon(u)$ represents the stiffness of the fuse or the spring connecting elements p and q. As the stiffness of the fuses are a function of elongation, the $\mathbf{J}_\epsilon(u)$ and subsequently the effective stiffness matrix $\hat{K}_T$ are displacement dependent matrices. The residual unbalanced force in iteration i is given by:

$$\epsilon_i^* = \frac{1}{\Delta t} A du_i + F(u_i^*) - F(u^(n-1)) \tag{3.28}$$

upon convergence of the corrector-predictor iterations to the a du value, velocity and acceleration at the time-step n are obtained by:

$$\dot{u}^n = \frac{\gamma}{\beta}\Delta t du + (1 - \frac{\gamma}{\beta})\dot{u}^{n-1} + \Delta t(1 - \frac{\gamma}{2\beta})\ddot{u}^{n-1} \tag{3.29}$$

$$\ddot{u}^n = \frac{\gamma}{\beta \Delta t^2} du + (\frac{1}{\beta \Delta t}\dot{u}^{n-1} + (\frac{1}{2\beta})\ddot{u}^{n-1} \tag{3.30}$$

3.2.4.2 Quasi-Static Verification

In the following verification study, the same 7 m height wall retaining a backfill with Poisson?s ratio $\nu = 0.3$, and friction angle $\phi = 40^o$ is used. The interface of the wall and the backfill soil is assumed to be frictionless ($\delta = 0$), and the backfill assumed to be cohesionless ($C = 0$). The backfill is 7 m deep and 32.5 long to assure its ability to accommodate the failure surface. The backfill has been discretized into 20 elements in each direction. Bottom and far-field boundaries are fixed, and the prescribed wall displacement is applied sufficiently slow to

Table 3.4: Parameters of Nakai-Matsuoka (1983) soil model used in FEM simulations by Nakai (1981).

Parameter	Value
λ^*	0.9
μ^*	0.27
μ'^*	0.41
γ^*_{oi}	0.10%
C^*_d	0.066%
σ^*_{mi}	98 KN/m^2
K_o	0.45
ν	0.3
ϕ	40^o

avoid dynamic effects.

The strength of fuses is calibrated to achieve the force-displacement relationship of FEM simulations by Nakai (1981) for quasi-static push/pull of a cantilevered wall with material properties tabulated in Table 3.4. The calibrated elasticity modulus $E = 13$ MPa is also used to match the initial stiffness. The interface of wall is a frictionless in Nakai (1985); hence, we employ Rankine?s closed form equation to determine the location of failure surface in the LIM. The force-displacement calculated by both models are compared in Figure 3.21.

The model is also verified against LSH model proposed by Shamsabadi et al. (2010). LSH is a limit equilibrium method that determines the force-displacement of a rigid abutment retaining a given backfill soil, subjected to passive push using method of slices. Parameters used in this verification study is tabulated in Table 3.5.

For the given soil properties, the calculated yielding strength of horizontal fuses are 3.45e+3 N and 1.76e+5 N for active and passive case, respectively. The calibrated values for the shear fuses are 4.01e-7 and 3.50e-2 which are negligible comparing to horizontal fuses.

Table 3.5: LSH parameters used for the calibration and verification of quasi-static implementation.

Parameter	Value	Description
$\boldsymbol{\phi}$	40	Friction angle
$\boldsymbol{\delta}$	0	Interface friction angle
C	0	Cohesion
$\boldsymbol{\epsilon_{50}}$	0.0035	Soil strain parameter
$\boldsymbol{\nu}$	0.3	Poisson's Ratio
$\boldsymbol{\gamma}$	16 KN/m^2	Density
N	30	Number of Slices

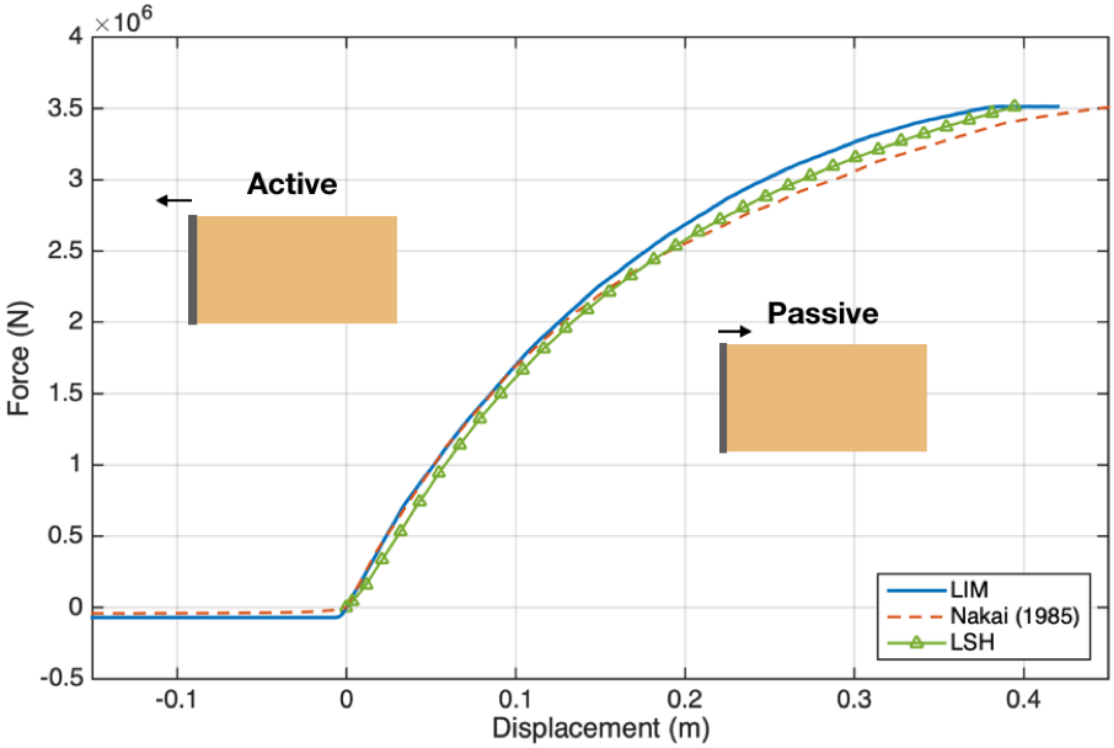

Figure 3.21: The force-displacement curve obtained by calibrated LIM versus Nakai (1981) and LSH.

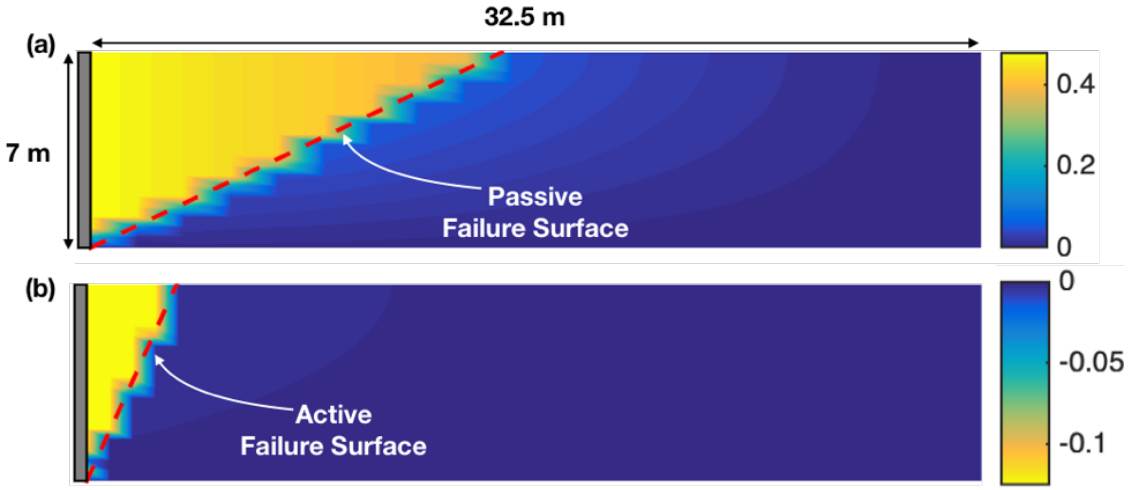

Figure 3.22: The displacement contour obtained by LIM in the passive (a) and active (b) limiting conditions show the large relative movement of the passive and active wedges.

3.2.4.3 Full Time-Domain Elastoplastic Verification

The formulation of the LIM in time-domain is explained in the previous section. In this section, the full implementation of the LIM model is verified against ABAQUS FE simulations for dynamic excitations. First, to evaluate the predictive ability of the LIM for specific frequencies, the ground DOF is subjected to semi-harmonic sine-dwell excitations with specific frequencies. Eventually, the model is verified for the broadband El Centro excitation record.

A wall with the same geometry and material property as section 3.2.3.2 is used in this study. The soil depth is extended to 75 meters (Figure 3.23) and to avoid unnecessary convergence iterations, first 50 meters of the soil is an elastic material. As reflected in Table 3.6 the elastic property of the elastic property of the elastic layer is the same as the foundation layer. The Mohr-Coulomb plasticity model is used for modeling elastic-plastic materials (soil 1 and soil 2). The mesh size reduces by distancing from boundaries and approaching to the concrete wall. The height of the wall is discretized into hundred elements and the width of the wall into six.

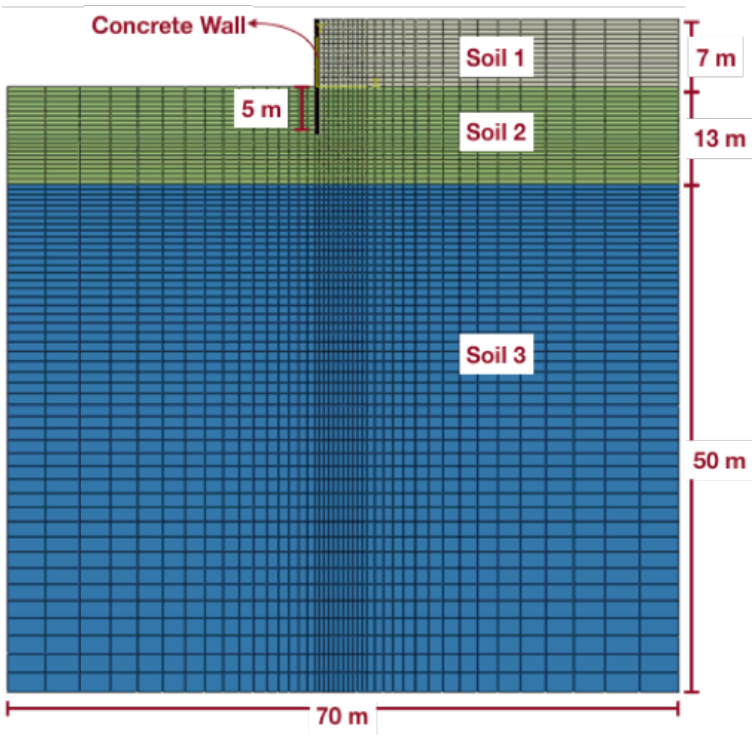

Figure 3.23: The ABAQUS FEM model with elastoplastic material.

Table 3.6: Material properties used in the elastic-plastic FEM model.

	Soil 1 **Backfill**	Soil 2 **Sublayer**	Soil 3 **Elastic Layer**	Concrete **wall**	**Unit**
Density	1600	1900	1900	2400	kg/m^3
Young's Modulus	2e+7	4e+7	4e+7	2.056e+10	N/m^2
Poisson's Ratio	0.35	0.3	0.3	0.2	
Friction Angle	28	40	-	-	Degrees
Dilatancy Angle	0.1	0.1	-	-	Degrees
Cohesion	5000	2000	-	-	N/m^2

Sine-Dwell Excitations: Similar to section 3.2.3.2, the LIM is initially verified against FEM for sine-dwell displacement time-history. Also similar to section 3.2.3.2, for each frequency of our series of sine-dwell excitations, the ground motion time-history begins with three periods of rest followed by 10 periods of ascending amplitude. After the first eight periods the signal reaches to its maximum amplitude and hold the amplitude for another 20 periods till after 10 period of descending it returns to rest state. The simulations are stopped

after 46 periods giving the system another three periods for free-vibration and returning to the rest (Figure 3.13).

The three sine-dwell displacement time-histories used in this verification study have the same frequencies (0.07 Hz, 0.24 Hz, and 2 Hz). The amplitude used to verify the elastic model (0.1 m) caused such severe plasticity in the FEM model for 2 Hz case that no converged solution could be obtained. Therefore, the peak amplitude for all frequencies chosen to be 1 cm in this verification study. Even 1 cm peak amplitude of the excitations caused significant residual force.

Figure 3.24 shows a comparison of displacement, force and moment time-histories calculated by LIM and FEM. The calibrated translation base stiffness K_t for 0.07, 0.24 Hz and 2.00 Hz are 1.10e+6, 1.06e+6, and 3.35e+5 N/m, respectively. The yielding strength of horizontal fuse elements is F_{yh}=2e+3 N. The shear fuses are assumed to be strengthless F_{ys}=0. Small numerical damping (κ=5e-5 N.s) is added to the model to alleviate effects of numerical discretization of the soil domain and account for energy dissipation by Mohr-Coulomb material in areas other than failure surface.

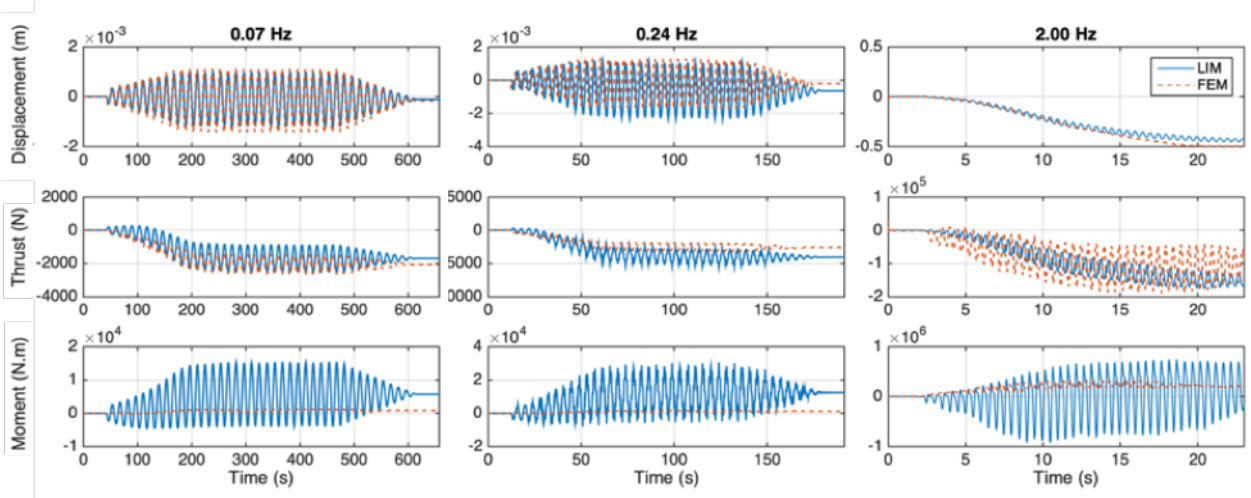

Figure 3.24: Comparison of the displacement, trust and moment time-histories calculated by FEM and LIM.

Although the LIM provides good estimation of displacement and thrust mobilized behind

the wall, it overestimates the moment in all frequencies for several reasons. The idealization of the flexible wall (in FEM) to a rigid wall (in LIM) significantly effects the amplitude of the moment. Also, the base in the LIM model assumed to behave elastic while the FEM simulations shows a passive wedge mobilized behind the embedded part of the wall (Figure 3.25). This passive wedge indicates that the embedment behaves in an elastoplastic way rather than a perfectly elastic. This issue will be further explained in section 3.4.2 wherein future extensions of the LIM are described.

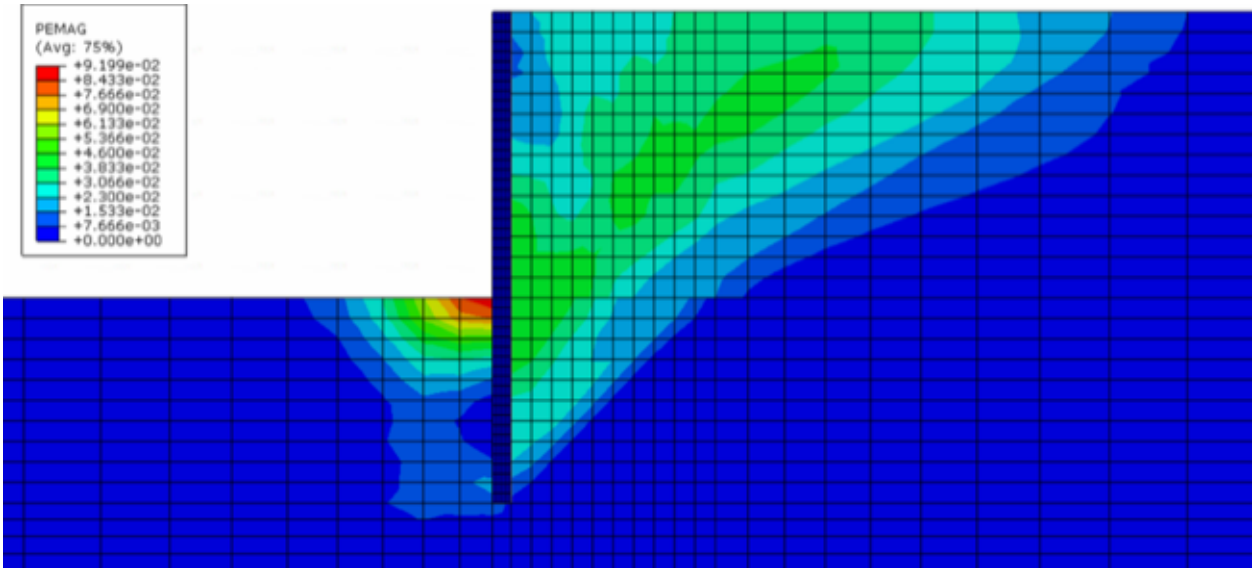

Figure 3.25: Plastic strain magnitude contour in rest after El Centro excitation obtained from FEM simulation. The concentration of the plastic strain shows passive and active failure wedges.

Broadband (El Centro) Excitation: The elastoplastic LIM is verified against FEM simulations for the El Centro broadband excitation. In the translational base stiffness in these simulations is calibrated to 1.13e+6 N/m and the strength of fuses are the same as the semi-harmonic excitations (F_{yh}=2e+3 N, F_{ys}= 0). The same damping coefficient κ=5e-5 N.s is used to alleviate effects of numerical discretization of the soil domain, the trapped energy due to truncation of the bottom boundary, and account for energy dissipation by Mohr-Coulomb material in areas other than failure surface. Figure 2 25 shows a comparison of the time-histories of LIM and FEM model.

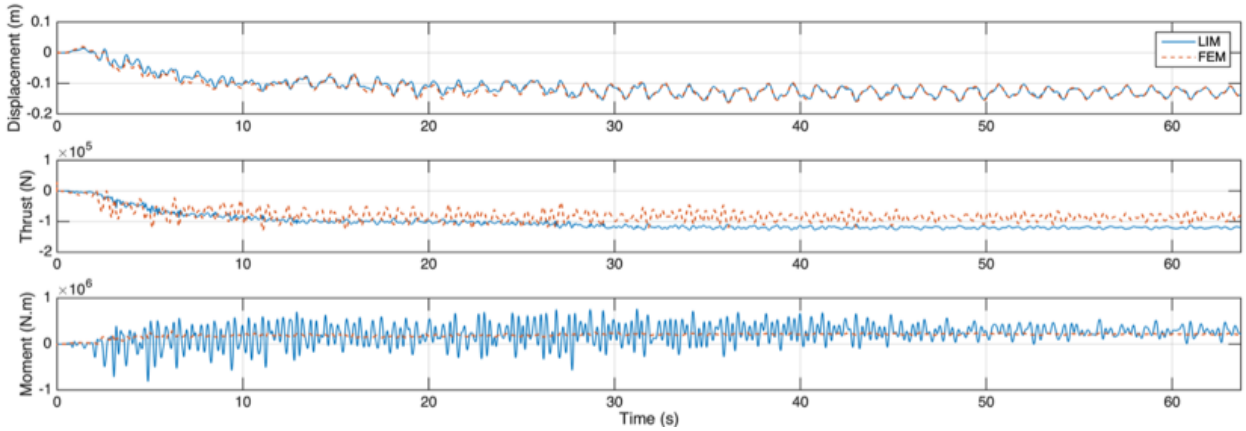

Figure 3.26: The displacement, thrust and moment time-histories obtained by LIM versus FEM simulations.

3.3 LIM for Performance-Based Assessment

The concept of Performance-Based Seismic Design (PBSD) is developed to mitigate consequences designs per of prescriptive building codes. The orthodox building design procedure involves satisfying certain criteria that are intended to protect human life under a design seismic incident. Such perspective criteria fail to account for the cost of repair and indirect economic losses due to the downtime of the building. On the other hand, in PBSD prospective the design is not only intended to guarantee the safety but also to assure that direct and indirect costs due to an earthquake incident, is rationally proportional to the intensity and return period of an earthquake.

FEMA (2012) in Seismic Performance Assessment of Buildings, proposed a PBSD procedure that includes two preliminary steps and several design/assessment iterations (Figure 3.27). It begins with setting a performance level in terms of some performance criteria (like residual drift, etc.) and determining potential seismic scenarios based on the geotechnical characteristics of the site. Subsequently, the performance of the initial design is assessed under potential seismic scenarios, and the design is modified until it reaches the pre-set performance level. The performance assessment step includes enormous time-history analyses.

In establishing the concept of PBSD for retaining walls and embedded structures, a cru-

cial step is to develop a computationally inexpensive robust analysis method. Although FEM fosters such robustness, its significant computational cost makes iterations of Performance-Based Assessment (PBA) practically impossible. In contrast to FEM, LIM reduces the computational cost by limiting the plastic behavior strategically. Its reliance on the fundamental principles of elasticity and also its simple physical interpretation facilitates its robust expansions.

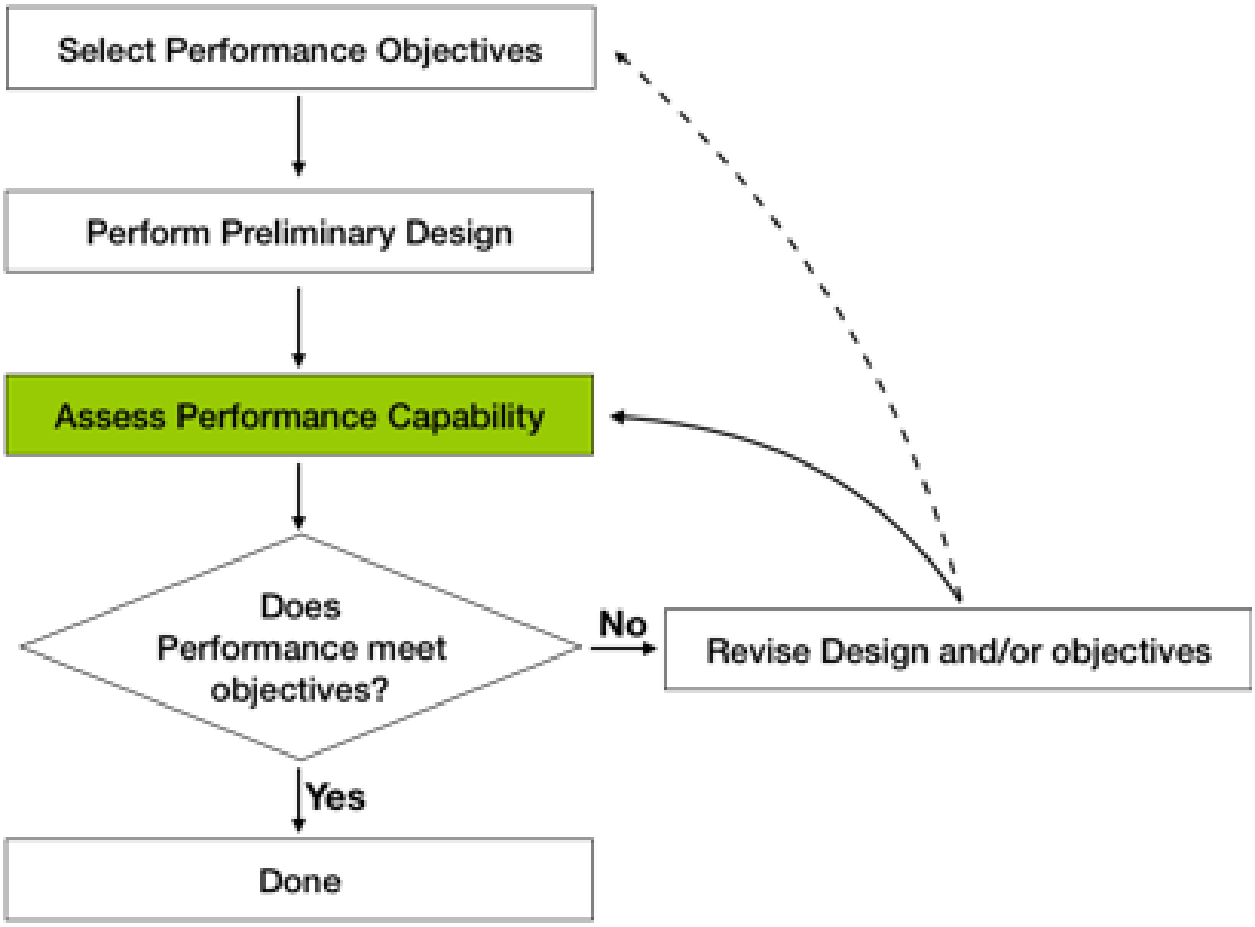

Figure 3.27: The flowchart of PBSD proposed by FEMA (2012).

In this chapter, the capability of LIM as a performance-based assessment toolbox is demonstrated. Since decisions on the performance criteria and performance levels are beyond the scope of this study, permanent wall drift is chosen as the performance criteria, and an arbitrary value is chosen to represent the objective performance level. Also, determining the appropriate intensity measure requires additional parametric study which is beyond this study. The employed intensity measure in this study is Peak Ground Acceleration (PGA).

Ground motions used in this study are all recorded ground motions in California earthquakes and are obtained from PEER database.

3.3.1 Problem Definition

To demonstrate capability of LIM for performance-based assessment of a retaining wall preliminary design. The wall mass and backfill soil, the foundation soil material properties are shown in Figure 3.28. In the preliminary design, the embedment is 5 meter and it may subject to change through the design iterations. The wall height is 7 meters, and it is unchangeable as imposed by the constructions in the vicinity of the wall.

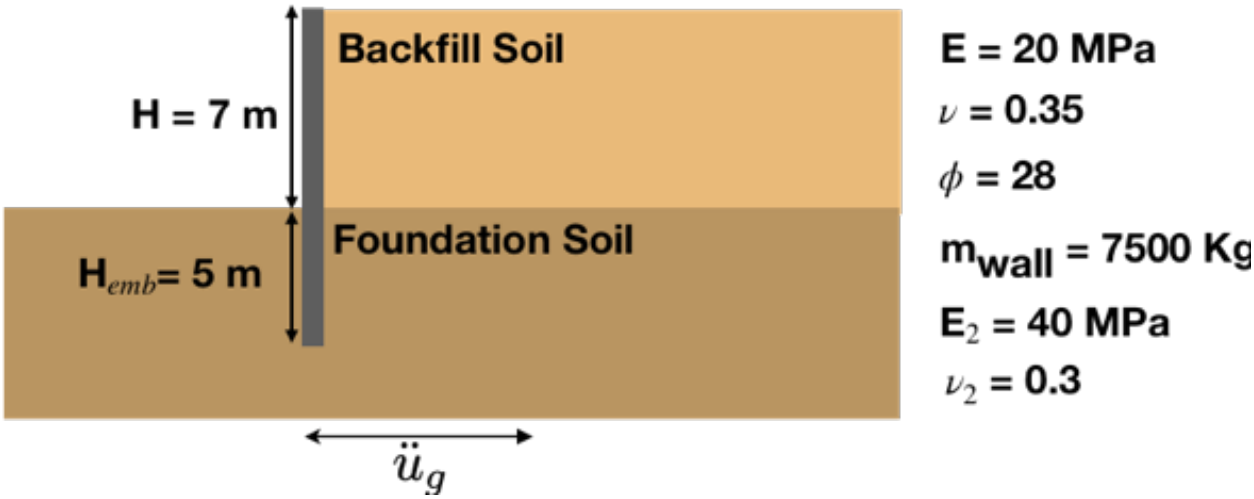

Figure 3.28: The preliminary design of the case-study wall.

The potential earthquakes in the wall are assumed to have frequency content similar to the records listed in Table 3.7. In this table component angle is the angle that the recorded time-history makes with north and 'V' means the vertical component. The records serve only as a broadband excitation, and their orientations are not important for the simulations. In other words, excitations are imposed as a ground motion perpendicular to the wall as shown in Figure 3.28 These records are not necessarily the accurate choice of ground motions and are utilized just for the purpose of demonstration.

The acceleration time-histories of these records are plotted in Figure 3.29. In a few of

the ground motions found to have base drift. To obtain input displacement time-histories baseline correction is performed and the corrected displacements are plotted in Figure 3.30. The intensity of the ground motions are normalized based on their Peak Ground Acceleration (PGA) from 0.05g to 0.3g. The frequency contents of the normalized displacement time-histories are shown in Figure 3.31.

Table 3.7: The earthquake used in the performance-based seismic assessment of the sample retaining wall.

	Earthquake Name	Date	Station	Component Angle	DT (Sec)	Duration (Sec)
1	**Imperial Valley**	5/19/40	El Centro Array #9	180	0.01	53.72
2	**Northwest California**	2/9/41	Ferndale City Hall	45	0.005	40
3	**Kern County**	7/21/52	LA - Hollywood	180	0.005	70
4	**Kern County**	7/21/52	Pasadena - CIT Athenaeum	V	0.01	77.27
5	**Kern County**	7/21/52	Pasadena - CIT Athenaeum	270	0.01	77.35
6	**Kern County**	7/21/52	Taft Lincoln School	V	0.01	54.24
7	**Kern County**	7/21/52	Taft Lincoln School	21	0.01	54.35
8	**Kern County**	7/21/52	Taft Lincoln School	180	0.01	79.99
9	**Borrego**	4/9/68	El Centro Array #9	270	0.01	79.99
10	**Northridge**	1/17/94	Harbor & California	90	0.02	65

3.3.2 Sample Performance-Based Assessment Post-Processing

In this example study, permanent wall drift assumed to be a sufficiently accurate indicator of the structural performance (performance criteria) and in the acceptable performance level the is assumed to be permanent drift less than 2% height of the wall (in this case 14 cm). Wall displacement time-histories for ground motions with frequency content similar to listed ground motions in Table 3.7, are shown in Figure 3.32 to Figure 3.33. The dashed line in these figures represent the 14 cm threshold defining the acceptable performance.

Summary of permanent wall drift (residual drift) of all 60 earthquake scenarios is shown in Figure 3.38. By defining failure as exceedance of the residual drift from the prescribed

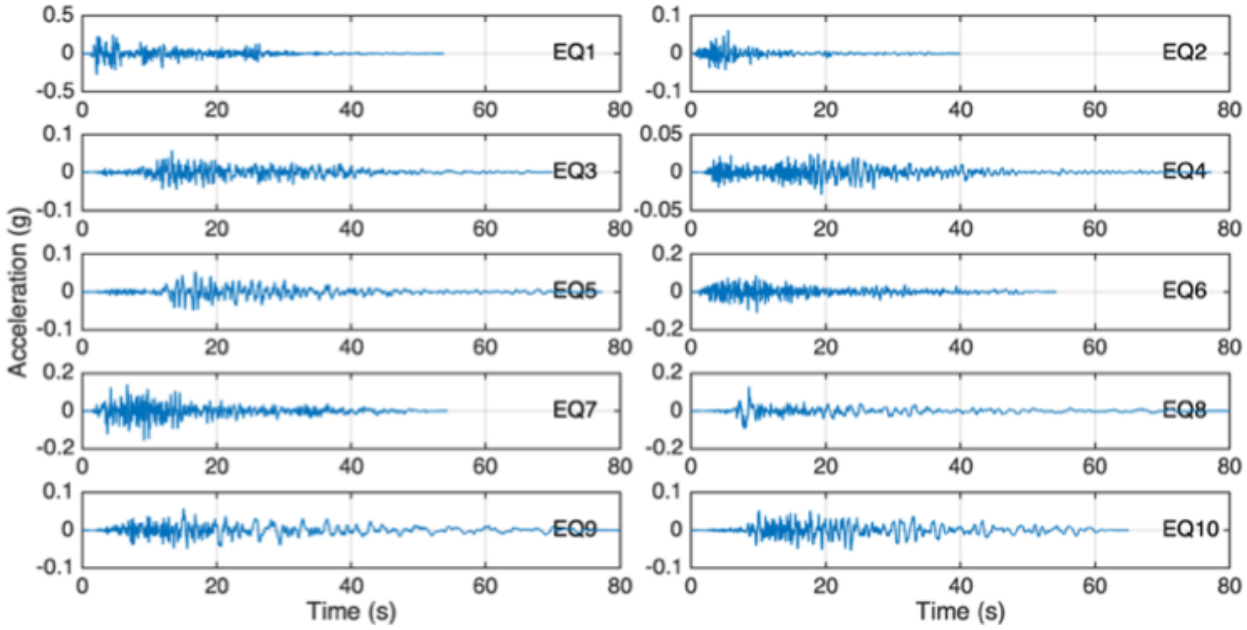

Figure 3.29: Time-history records used for performance-based assessment of the sample retaining wall.

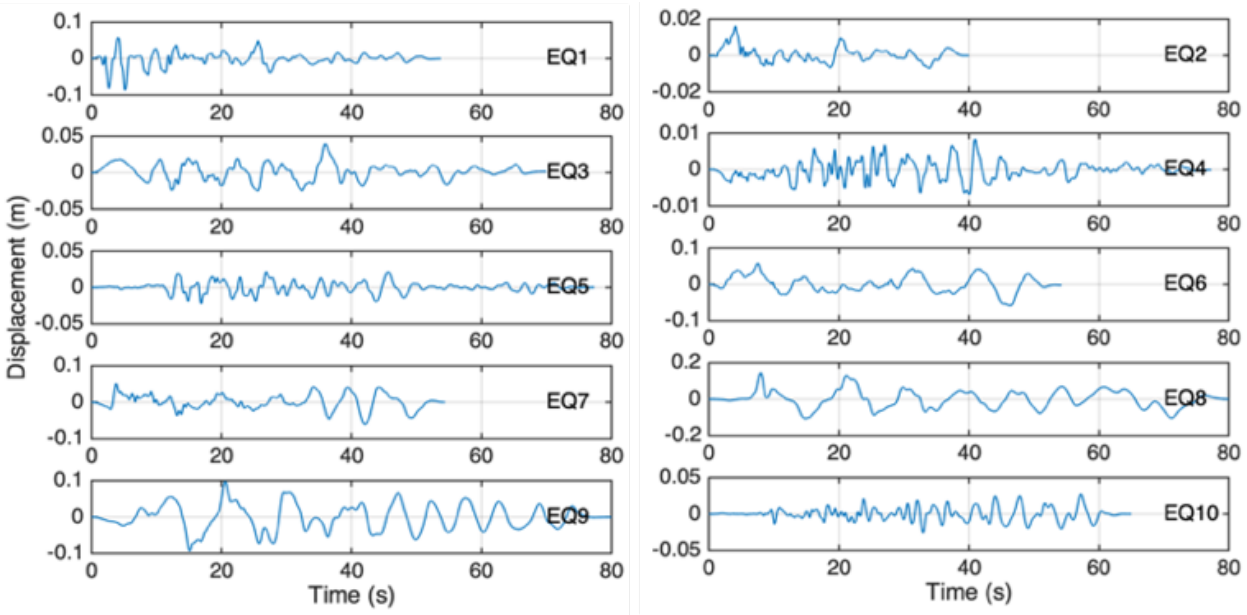

Figure 3.30: Corrected displacement time-history records used as input motions in LIM models.

threshold $u_r < u_t = -0.14m$, the failure/success matrix of these simulation are summarized in Figure 3.39.

The probability of failure for a given PGA can be quantified based on this failure-success

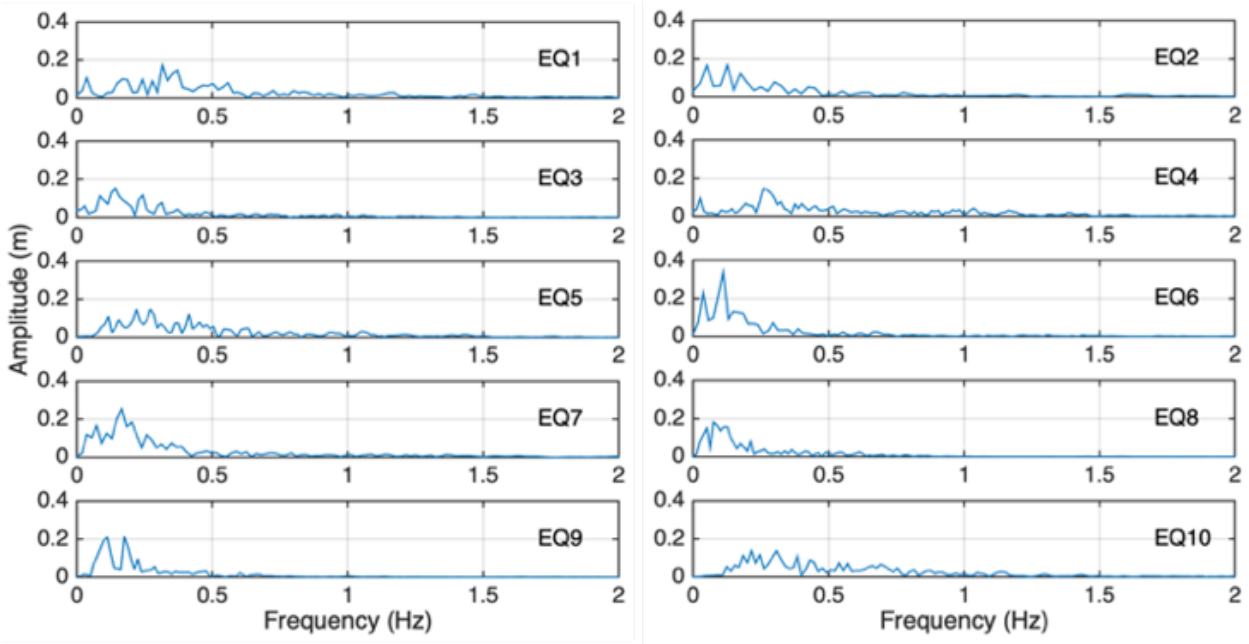

Figure 3.31: The frequency content of normalized displacement time-histories.

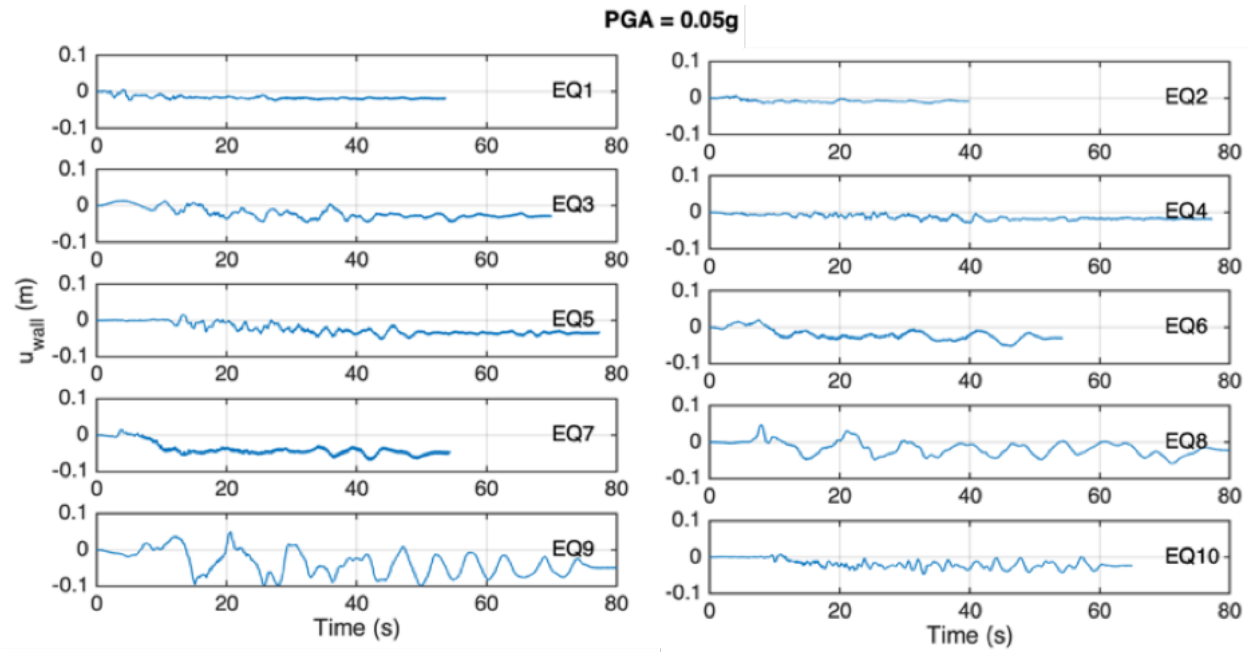

Figure 3.32: Wall displacement time-history for the potential earthquake scenarios, normalized PGA = $0.05g$.

matrix. Assuming the failure for a given PGA follows a binomial distribution, one can estimate a probability of failure and its corresponding confidence interval for a certain level confidence using elementary statistical operations. The estimated probabilities of failure for

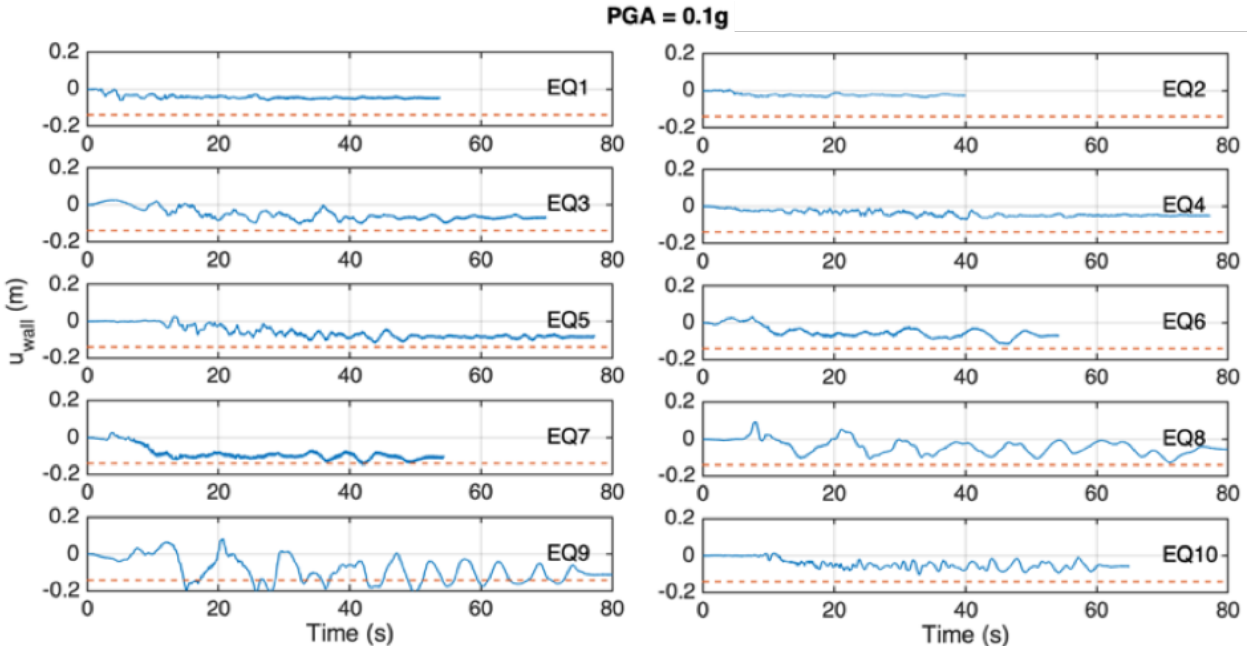

Figure 3.33: Wall displacement time-history for the potential earthquake scenarios, normalized PGA = $0.10g$.

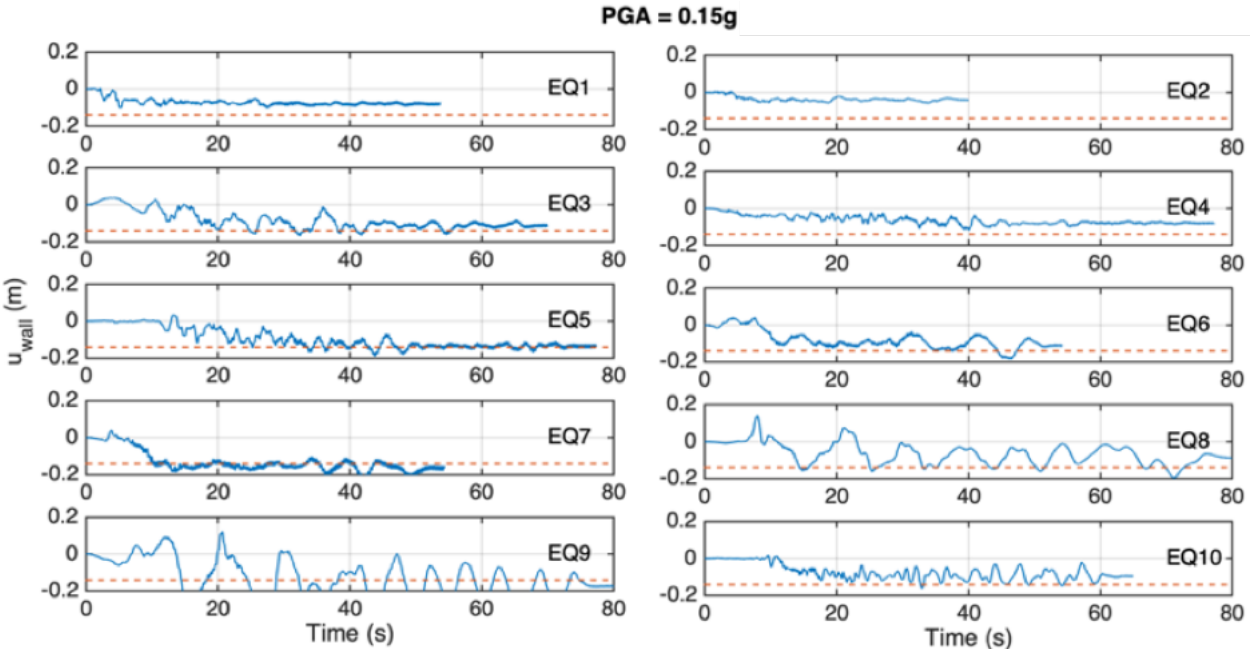

Figure 3.34: Wall displacement time-history for the potential earthquake scenarios, normalized PGA = $0.15g$.

this study and their corresponding 95% confidence interval are listed in Table 3.8. After fitting an erf function to the obtained probabilities, the probability of failure as a function

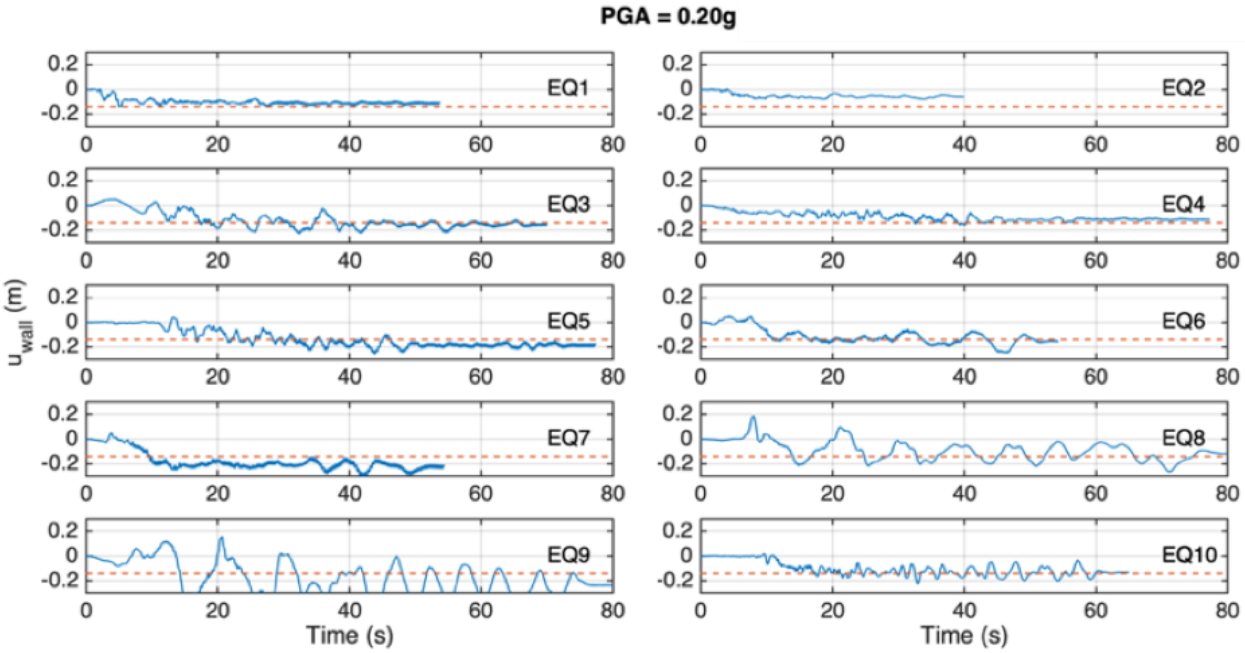

Figure 3.35: Wall displacement time-history for the potential earthquake scenarios, normalized PGA = $0.20g$.

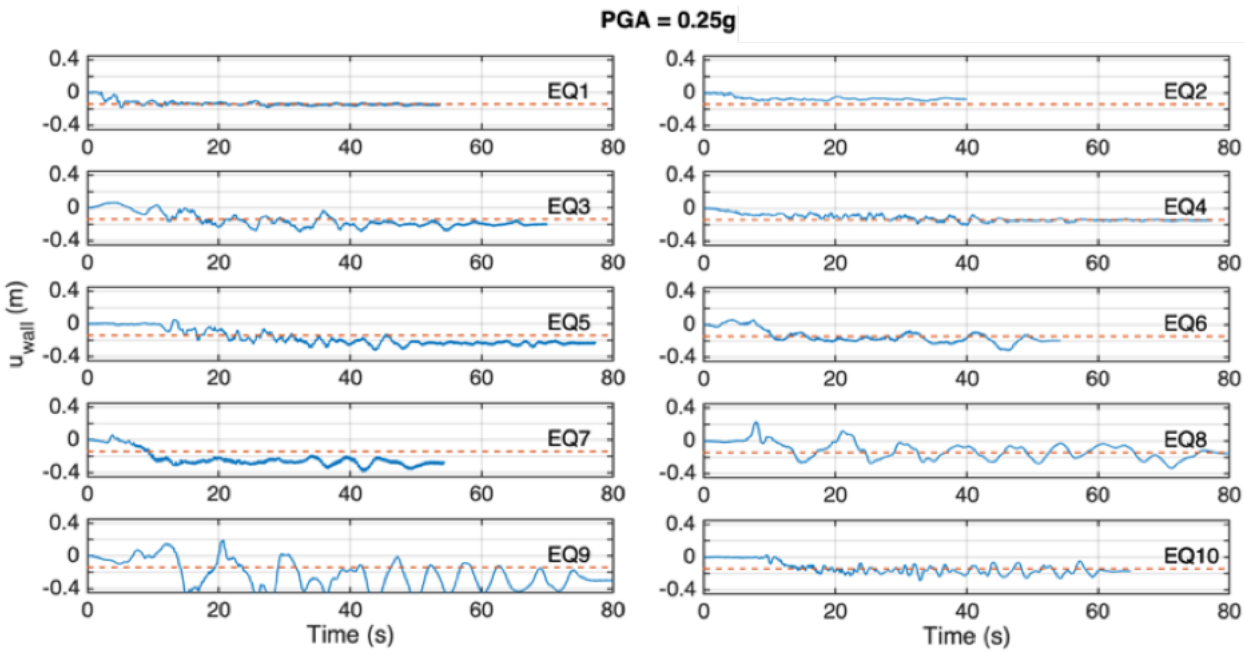

Figure 3.36: Wall displacement time-history for the potential earthquake scenarios, normalized PGA = $0.25g$.

of PGA is shown in Figure 3.40. The probabilities directly calculated by simulations are scattered around the curve. The filled region in this figure shows the 95% confidence interval

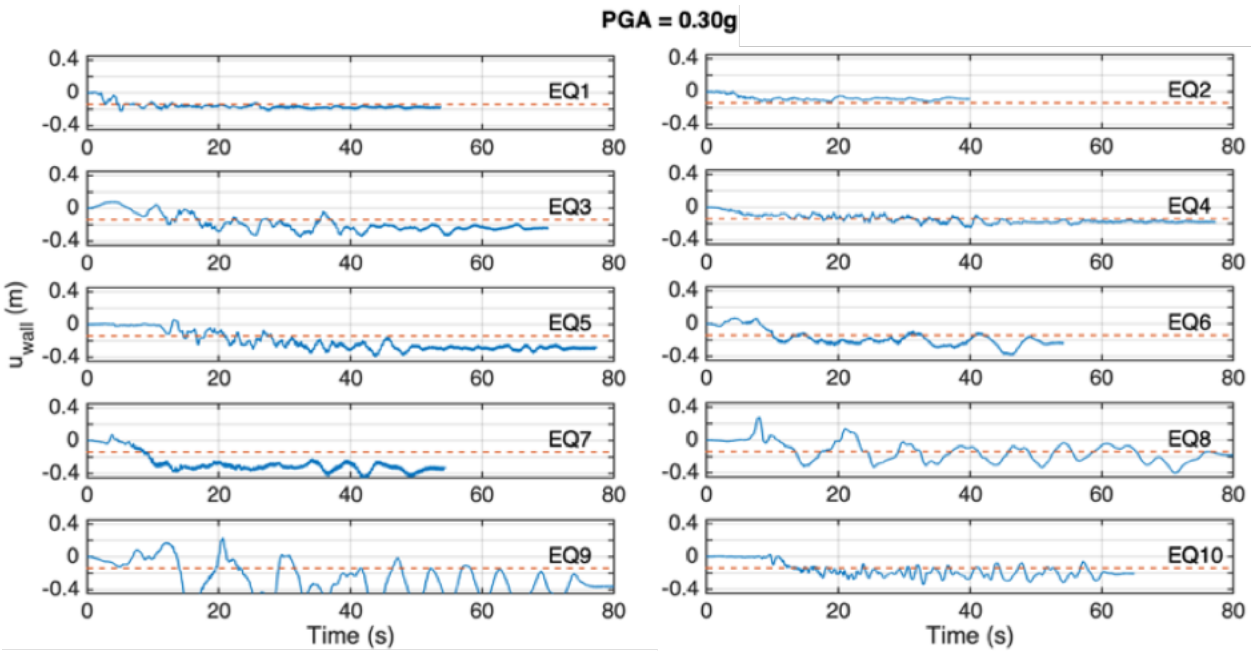

Figure 3.37: Wall displacement time-history for the potential earthquake scenarios, normalized PGA = 0.30g.

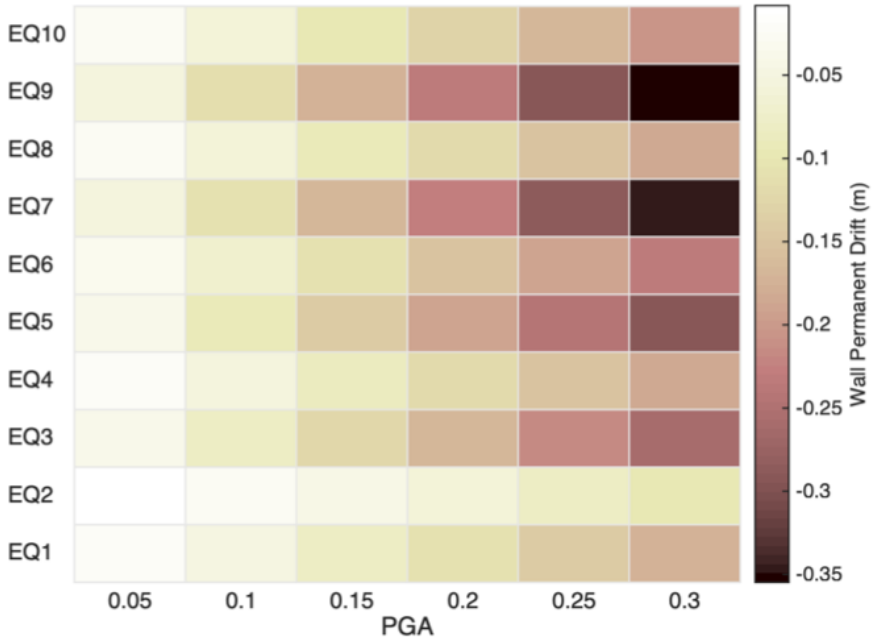

Figure 3.38: Summary of residual drifts for all 60 earthquake scenarios.

of the estimated probability. The confidence interval becomes narrower by increasing the number of potential earthquake scenarios.

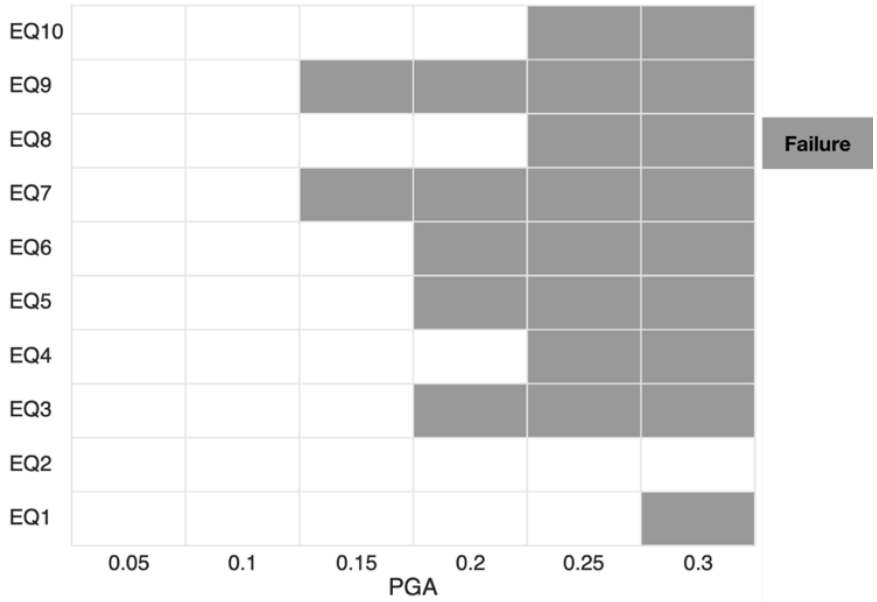

Figure 3.39: The failure/success matrix of the preliminary design under the given 60 earthquake scenarios.

3.4 Summary and Conclusions

The details of the LIM are described and verification studies were provided earlier in section 2 of this chapter and LIM's application in performance-based assessment was discussed in section 3. In what follows, a brief summary of the model is provided in an effort to articulate is current capabilities followed by a short section wherein potential future extensions are elaborated. The extensions include the use of state-of-the-art site response analyses in the transfer function module, employment of absorbing boundaries at truncation boundaries of

Table 3.8: Estimated probability of failure for sample PGA values.

PGA (g)	Avg u_r (m)	Min u_r (m)	Max u_r (m)	$\widehat{P}(u_r > u_t)$	95% Confidence Interval
0.05	− 0.028	− 0.049	− 0.008	0	[0.00, 0.30]
0.1	− 0.067	− 0.108	− 0.024	0	[0.00, 0.30]
0.15	− 0.107	− 0.170	− 0.041	0.2	[0.02, 0.06]
0.2	− 0.149	− 0.231	− 0.057	0.5	[0.19, 0.81]
0.25	− 0.189	− 0.293	− 0.074	0.8	[0.44, 0.97]
0.3	− 0.235	− 0.355	− 0.091	0.9	[0.55, 1.00]

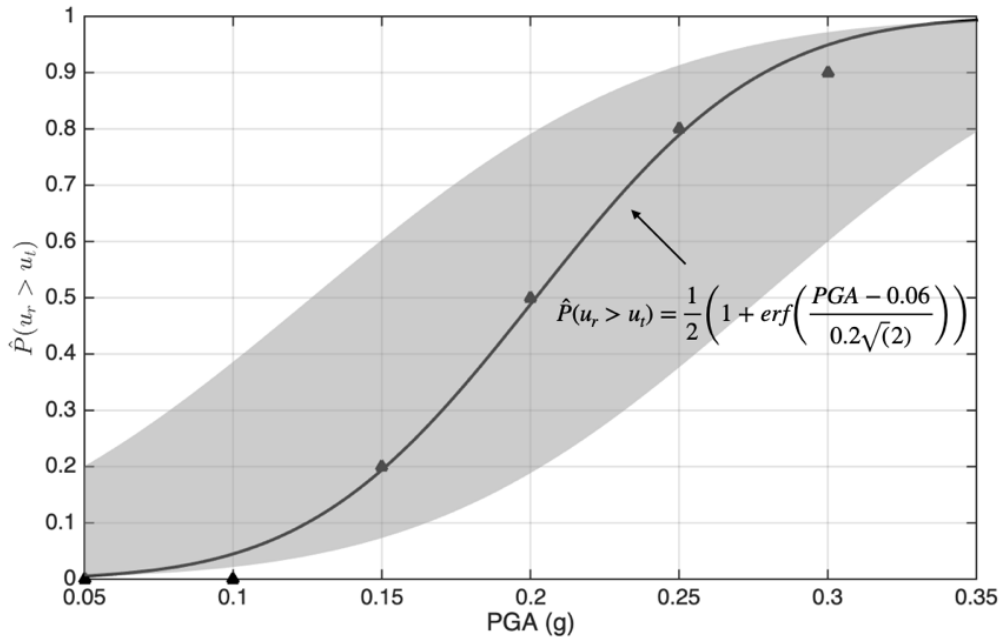

Figure 3.40: Probability of failure as a function PGA in units of gravity accelerations. The filled region represents the 95% confidences interval.

the LIM, incorporation of wall flexibility using beam elements, and enabling soil layering. All these extensions will serve the ultimate goal of this study, which is the development of a comprehensive performance-based seismic assessment and design tool for earth retaining walls.

3.4.1 Summary of the Method

The Lumped Impedance Model (LIM) is a nonlinear lumped parameter model for simulation of retaining wall-backfill interaction. The elastic parameters of the lumped model are obtained by numerical discretization of the uncoupled equation of motion proposed by Arias et al. (1981), and elasto-plastic fuses are calibrated to imitate the failure behavior estimated by LSH proposed by Shamsabadi et al. (2013). Per Wolf?s (1994) classification of lumped models, the development of LIM is categorized under the systematic approach of developing lumped models since it uses analytical equations for determining parameters rather than optimization.

Figure 3.41 shows a generic form of the LIM. In the magnified part (b) of the figure details of connectivity of a lumped mass on the failure surface is shown. The bottom shear spring and the top fuse has the same shear stiffness $K_s = G\Delta x/\Delta y$, and the left fuse and the right spring has the same horizontal stiffness $K_h = E/(1-\nu^2)\Delta y/\Delta x$. The yielding force of the horizontal fuses f_{yh} are calculated by the capacity calculated by LSH divided by the number of elements on the failure surface and yielding strength of shear fuses f_{ys} are negligible.

The vertical boundary far from the wall is truncated in a sufficiently distant location to imitate a far-field boundary. The motion is inputted to a transfer function which transfers bedrock motion to the wall level motion. Translational and rocking stiffness values (K_t and K_r) are calibrated values to account for the resistance force and moment provided by the embedment. In future expansions of the LIM, latter features will be modified to provide a more accurate representation of the wall-backfill interaction.

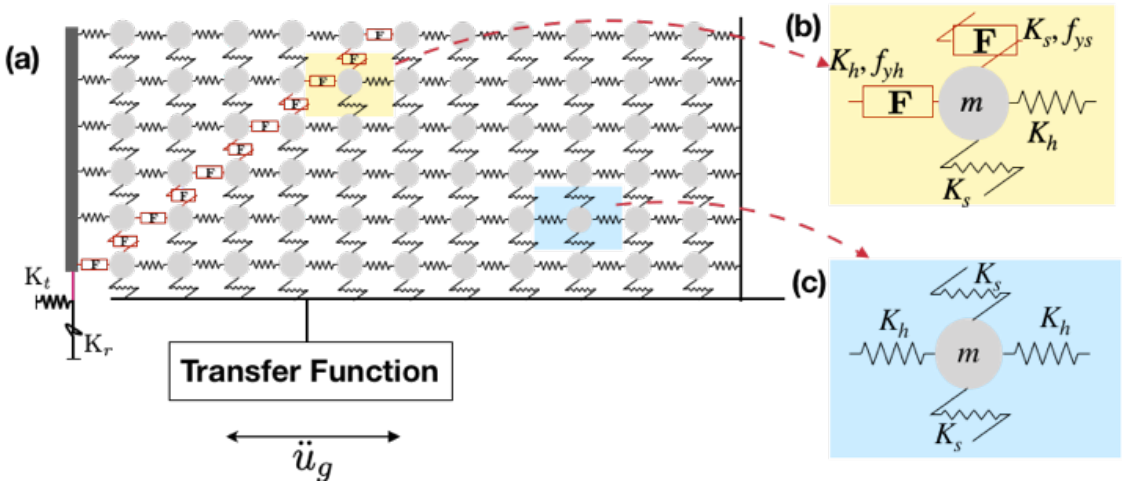

Figure 3.41: (a) Generic form of the LIM, (b) connectivity of a lumped mass on the failure surface, (c) connectivity of a typical lumped mass.

3.4.2 Future Extensions

Although verifications show the LIM has a strong predictive power, there are some extensions that makes LIM a universal tool for analysis of retaining walls. It?s particularly important

for LIM to handle retaining wall with layered backfills while in the current study the backfill assumed to be homogenous. Also, in the current study the base stiffness values are frequency independent calibrated values, while the interaction of the wall embedment with the foundation soil is frequency dependent. Effects of the trapped energy due to fixed boundary conditions can be alleviated by utilizing absorbing boundary conditions like Lysmer (1969), PML, and etc. More realistic moment estimations can be obtained by using beam-elements to account for the wall flexibility.

3.4.2.1 Soil Layering and Site Response Analysis

The current study focused on development of the LIM model for homogenous backfill material. However, soil layering can be conveniently implanted in the LIM model using the physical interpretation of the lumped parameters. A generic form of the LIM with layered soil is depicted in Figure 3.42. Different density of layers translates into lumps with different masses, elastic parameters changes with the elastic property of layers, strength parameters of soil layers define the yielding force of the fuse elements.

A potential obstacle in the implementation of LIM for layered backfill is the internal layers interface behavior especially in the case of passive/active limit conditions. In a comparative study of current site response analysis methods by Bolisseti and Whittaker (2015), the high-frequency response is reported as a common problem with the available time-domain analysis methods. The observed high-frequency response is due to inability of internal soil layer boundaries to transmit waves with certain frequency content.

It is reasonable to assume that within each layer elastic properties are conserved. Therefore, stiffness values of shear springs and horizontal springs are calculated using the same formulations in LIM for homogenous backfill. Previous studies for formulating the contact behavior of elastic bodies including Simons and Bergan (1986), and Wu et al. (2016) serve as the basis for formulating the interface shear springs in layered LIM.

Most studies in the area of limit conditions of retaining walls, consider a homogenous backfill material. Shamsabadi et al. (2013) (the method used for determining the strength of fuse elements) employs methods commonly used in slope stability analysis, to determine the failure surface shape and the limit condition force for a retaining wall. Slopes with layered soil are investigated in Ji and Low (2012), and Xue and Gavin (2007). A preliminary study for developing layered LIM should include modification of Shamsabadi et al. (2013) to account for soil layering.

The transfer function connected to the ground degree of freedom in LIM provides the opportunity of fostering state-of-the-art in site response analysis for transferring motions in bedrock to the simulation depth. The LIM is capable of performing a linear site-response analysis similar to well-known software SHAKE, use of nonlinear site response analysis models like DEEPSOIL increases the credibility of simulations with an insignificant amount of computational cost.

3.4.2.2 Wall Flexibility

The idealization of the wall as rigid plate causes in overestimation of moment and elimination of some shape modes. One can employ beam elements available in the literature to account for the flexibility of the wall. It is common sense that a reinforced concrete wall rarely experiences nonlinearity or inelasticity and a linear elastic beam element formulation should provide a satisfactory estimation of its behavior. Although, one can use the inelastic beam

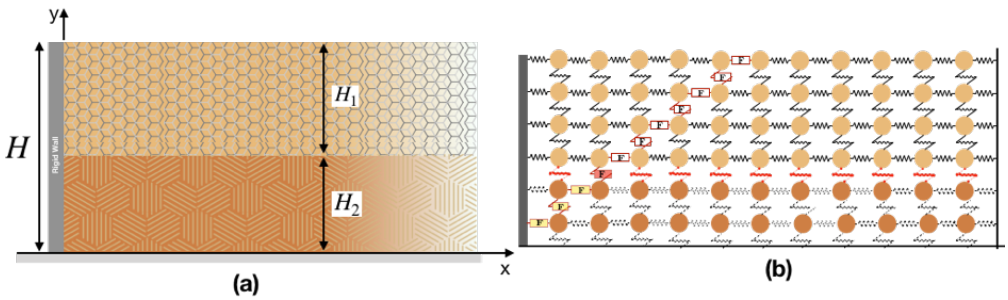

Figure 3.42: (a) Schematic presentation of a rigid wall on a rigid base retaining layered soil backfill material. (b) Generic concept of LIM with layered soil.

element formulation proposed by Spacone et al. (1992) to account for inelastic behavior of the wall under extreme conditions like extreme vertical dynamic surcharge.

3.4.2.3 The Truncation Boundary

In verification of the model against FEM simulations, effect of the trapped energy due to truncation of the bottom boundary has been alleviated using some artificial numerical damping. In the FEM model, the simulated soil is 70 meters deep, and the effects of reelections are less because the energy is redistributed all over the soil medium. While in the LIM simulation only the 7 meters depth of backfill is simulated and the energy injected in through the fixed bottom boundary is trapped in this limited medium.

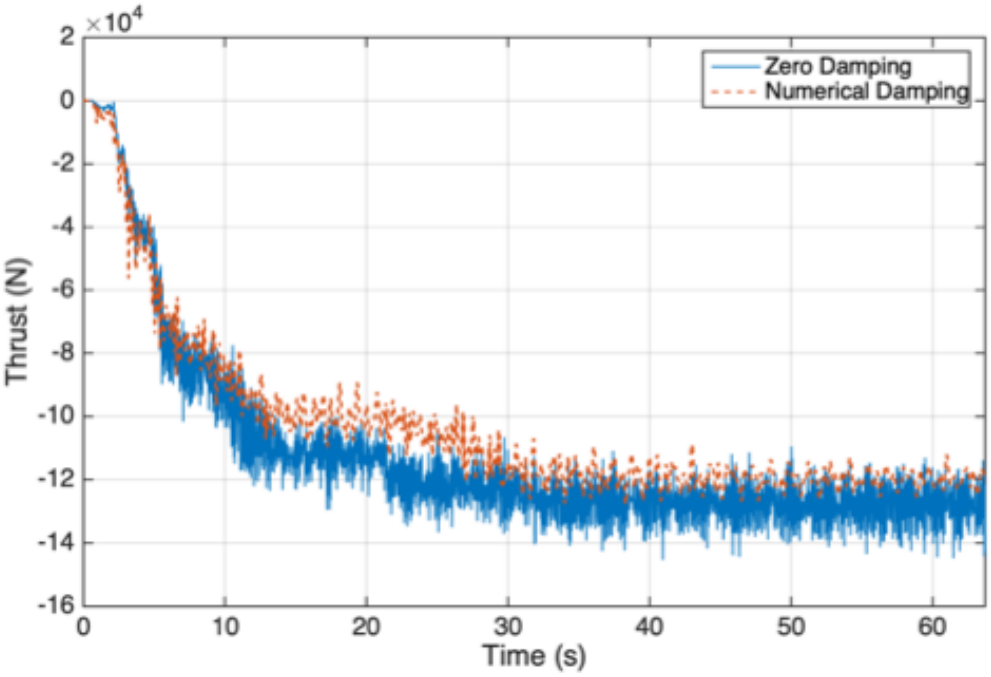

Figure 3.43: Effect of the trapped energy due to fixed bottom boundary is observable in the LIM time-history response under the El Centro excitation.

This trapped energy is seen in high-frequency fluctuations in the time-history response of the LIM under the El Centro excitation in Figure 3.43. Although the numerical damping added to the model eliminates the effects of such trapped energy, it inevitably suppresses the effects of some of the real vibration modes. The existence of an absorbing boundary condition

at the bottom boundary can significantly reduce the necessity of numerical damping. Placing such boundary condition on the far vertical boundary can also help to account for the dissipation of energy in the far-field. The concept of employing the absorbing boundary condition is illustrated in Figure 3.44.

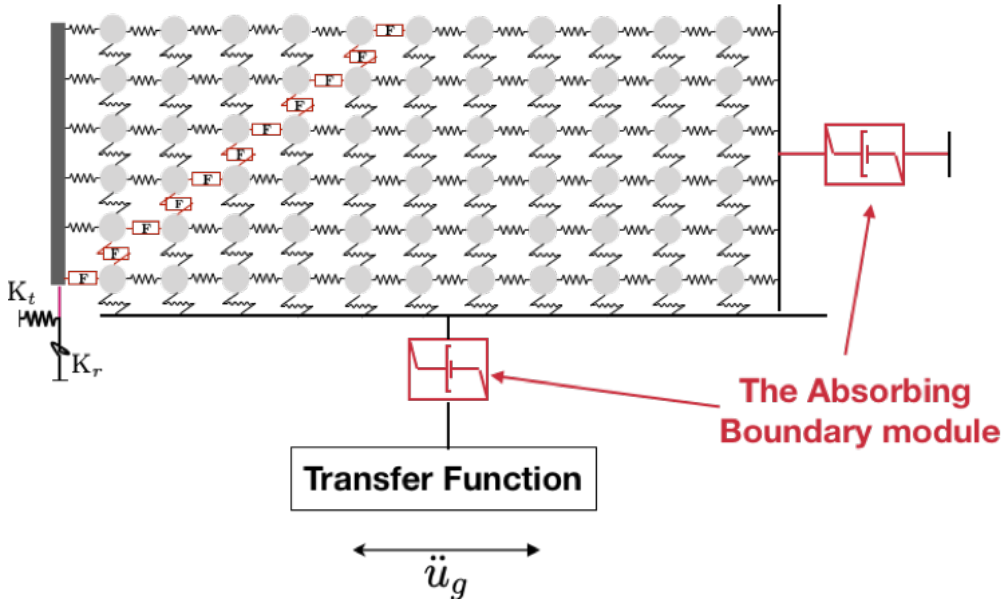

Figure 3.44: LIM with concept of absorbing boundary conditions.

3.4.2.4 Full Geometry Simulations

In the above verification studies, the base stiffness values are calibrated in order to capture the objective response calculated by FEM. Such calibration presumes that the embedment?s interaction with the foundation soil is frequency independent and linear elastic. However, similar to the wall-backfill interaction which is a frequency dependent behavior, the embedment-soil interaction is also frequency dependent. Furthermore, the passive wedge mobilized behind the embedment implies the nonlinearity of such interaction.

Both these issues can be addressed using a simple expansion of the simulated soil domain in the LIM to include the foundation soil as well. A concept of such extension is illustrated below.

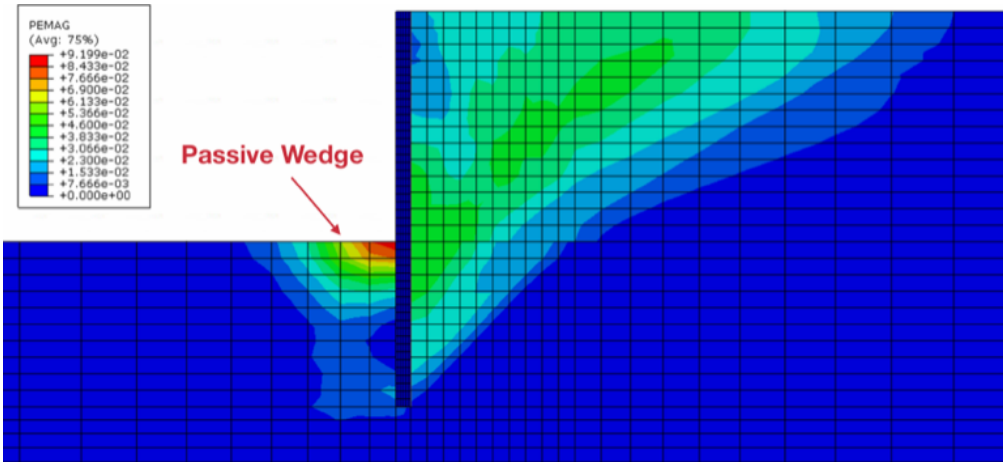

Figure 3.45: Mobilized plastic strains magnitude in rest state after the El Centro excitation.

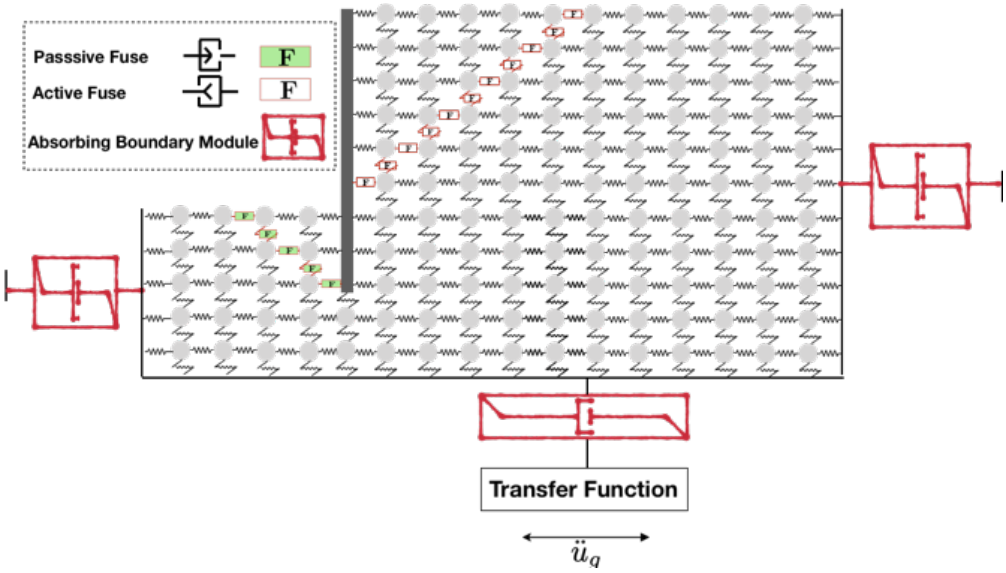

Figure 3.46: Concept of the LIM with full geometry that accounts for frequency dependency and nonlinearity of the embedment behavior.

REFERENCES

AASHTO - American Association of State Highway and Transportation Officials (2012). *AASHTO LRFD Bridge Design Specifications, Customary U.S. Units.*

Al Atik L, Sitar N (2010). Seismic earth pressures on cantilever retaining structures, *J. Geotech. & Geoenv. Eng.*, 136(10), 1324-1333.

Al-Homoud AS, Tahtamoni W (2000). Comparison between predictions using different simplified Newmarks' block-on-plane models and field values of earthquake induced displacements. *Soil Dynamics and Earthquake Engineering*, 19(2), 73-90.

Ambraseys N. N., and Menu, J. M. (1988). Earthquake-induced ground displacements. *Earthquake Engineering and Structural Dynamics*, 17, 1-105.

Anderson DG, Martin GM, Lam IP, Wang JN (2008). Seismic Analysis and Design of Retaining Walls, Buried Structures, Slopes, and Embankments. *NCHRP Report 611, Transportation Research Board, Washington DC.*

Arias A, Sanchez-Sesma F.J, Ovando-Shelley E (1981). A simplified elastic model for seismic analysis of earth- retaining structures with limited displacements, *Proceedings of 1st International Conference on Recent Advances in Geotechnical Earthquake Engineering and Soil Dynamics*, 26 April - 3 May, Missouri, USA.

Bolisetti, C., Wittaker, A.S. (2015). Site response, soil-structure interaction and structure-soil-structure interaction for performance assessment of buildings. *Technical Report MCEER-15-0002, University at Buffalo, State University of New York*

Bolton, M.D., Steedman, R.S. (1982). Centrifugal testing of microconcrete retaining walls subjected to base shaking, *Soil dynamics and Eq. Eng. Conf.*, Southampton, 311-329.

Brandenberg, SJ, G Mylonakis, and JP Stewart (2015). Kinematic framework for evaluating seismic earth pressures on retaining walls, *J. Geotech. & Geoenv. Engrg.*, 141(7), 04015031.

Brandenberg, SJ, JP Stewart, and G Mylonakis (2017). Influence of Wall Flexibility on Seismic Earth Pressures in Vertically Homogeneous Soil. *Proceedings Geotechnical Risk Assessment and Management.*

Cai Z, Bathurst RJ (1996). Deterministic sliding block methods for estimating seismic displacements of earth structures. *Soil Dynamics & Eq. Engineering*, 15(4), 255-268.

Candia AG, Sitar N (2013).Seismic Earth Pressures on Retaining Structures in Cohesive Soils., *Caltrans, Report No. UCB GT 13-02*, August 2013, pp. 161.

Chlimintzas, G. (2003). Seismic displacements of slopes using multi-block sliding technique. *PhD Thesis*. Imperial College, London.

Dennis, J.E., Welsch, R.E. (1978), Techniques for nonlinear least squares and robust regression. *Journal of Communications in Statistics- Simulation and Computation*, 345-359.

Elms, D.G. (2000). Refinements to the Newmark Sliding Block Model. *Proceedings 12th World Conference on Earthquake Engineering*, Auckland NZ.

Fang YS, Yang YC, Chen TJ (2003). Retaining walls damaged in the Chi-Chi earthquake. *Canadian Geotechnical Journal. 40(6), pp 1142-1153.*

Franklin, A.G., and Chang F.K., Earthquake resistance of rock fill dams: Report 5. Permanent displacements of earth embankments by Newmark Sliding Block Analysis, *Misc Paper: S-71-17, Soils and Pavements Laboratory, US Army Engineers Waterways Experiment Station, Vicksburg, Mississippi. 1977*

FEMA P-58-1 (2012). Seismic Performance Assessment of Buildings. Volume 1- Methodology, Federal Emergency Management Agency, Washington D.C.

FHWA (2011) LRFD Seismic Analysis and Design of Transportation Geotechnical Features and Structural Foundations, *Ref. Manual, Pub. No. FHWA-NHI-11-032.*

Gaudio D, Masini L, Rampello S (2018). A performance-based approach to design reinforced-earth retaining walls. *Geotextiles and Geomembranes*, 46, 470-485.

Gazetas G, JM Rosset (1979). Vertical vibration of machine foundations. *J. Geotech. & Geoenv. Engrg.* , 105, 1435-1454.

Jibson, R. (1994). Predicting earthquake-induced landslide displacements using Newmark's Sliding block analysis. *Transportation Research Record 1411,* Transportation Research Board, Washington, D.C. pp. 9-17.

Ji J, Low BK (2012). Stratified Response Surfaces for System Probabilistic Evaluation of Slopes, *J. Geotech. & Geoenv. Engrg.*, 138(11), 1398-1406.

Kloukinas P, Langoussis M, Mylonakis G (2012). Simple wave solution for seismic earth pressures on non-yielding walls. *J Geotech & Geoenvir. Eng.*, 138 (12), 1514-1519.

Kramer SL (1996). *Geotechnical Earthquake Engineering.* Prentice Hall, NJ.

Lew M, Sitar N, Al Atik L (2010). Seismic earth pressures: Fact or fiction. In: *Earth Retention Conference 3, ASCE Geotechnical Special Publication 208, R Finno, YMA Hashash, and P Arduino (editors).*

Lysmer J, Kuhlemeyer RL (1969). Finite dynamic model for infinite media. *Journal of the Engineering Mechanics Division, ASCE, 95(EM4), 859 876.*

Madabhushi G, Zeng X (2007). Simulating seismic response of cantilever retaining walls, *Journal of Geotechnical and Geoenvironmental Engineering, 133(5)*

Miyata M, Sugano T (2000). Experimental and Analytical Study on the effect of input motion on the behaviour of a caisson quay wall. *12th World Conference on Earthquake Engineering*, Auckland, NZ.

Morrison EE, Ebeling RM. (1995). Limit equilibrium computation of dynamic passive earth-pressure. *Canadian Geotechnical Journal;32:4817.*

Mononobe N, Matsuo M (1929). On the determination of earth pressures during earthquakes. *Proc. World Engrg. Congress, 9, 179187.*

Mylonakis GE, Kloukinas P, Papantonopoulos C (2007). An alternative to the Mononobe-Okabe equations for seismic earth pressures. *Soil Dynamics & Earthquake Engineering, 27(10), 957-969.*

Nadim F, Whitman R (1983). Seismically Induced Movement of Retaining Walls. *ASCE Journal of Geotechnical Engineering, 109(7), 915-931.*

Nakai T (1981), Finite element computations for active and passive earth pressure problems of retaining walls. *Soils and Foundations*, 25(3), 98-112.

NCHRP—National Cooperative Highway Research Program (2008). *Seismic Analysis and Design of Retaining Walls, Buried Structures, Slopes, and Embankments. Report 611, Prepared by D.G. Anderson, G.R. Martin, I.P. Lam, and J.N. Wang. Transportation Research Board, National Academies, Washington DC.*

Newmark NM (1965). Effects of earthquakes on dams and embankments. *Geotechnique*, 15(2), 139-160.

Okabe S (1926). General theory of earth pressure and seismic stability of retaining wall and dam. *J. Japanese Society of Civil Engineering*, 12(4), 34-41.

Ortiz, LA (1982). *Dynamic centrifuge testing of cantilever retaining walls. Technical Report: CaltechEERL:1982, SML-82-02, California Institute of Technology.*

Ostadan F (2005). Seismic soil pressure for building walls an updated approach. *Soil Dynamics & Earthquake Engineering, 25, 785-793.*

Richards R, Shi X (1994). Seismic lateral pressures in soils with cohesion. *Journal of Geotechnical Engineering. 120(7), 1230-1251.*

Richards R, Elms DG (1979). Seismic behavior of gravity retaining walls*Journal of the Geotechnical Engineering Division, ASCE*, 105(GT4): 449-464.

Saran, S. and Prakash, S. (1968). Dimensionless parameters for static and dynamic earth pressures behind retaining walls. *Indian Geotechnical Journal*, 7(3), 295-310.

Scott, R. F. (1973). Earthquake-induced pressures on retaining walls. *Proc. 5th World Conf. on Earthquake Eng.*, Rome, Italy, II, 1611-1620.

Shamsabadi A, Xu SY, Taciroglu E (2013). A generalized log-spiral-Rankine limit equilibrium model for seismic earth pressure analysis, *Soil Dynamics & Earthquake Engineering*, 49, 197-209.

Shields DH, Tolunay AZ (1973). Passive pressure coefficients by method of slices. *Journal of the Soil Mechanics and Foundations Division, ASCE*, 99(12), 1043-1053.

Sherig MA, Ishibashi I, Lee CD (1982). Earth pressure against rigid retaining walls, *Journal of Geotechnical Engineering Division, ASCE*, 108(5), 679-695.

Shukla S, Gupta S, Sivakugan N (2009). Active earth pressure on retaining wall for $c-\phi$ soil backfill under seismic loading condition *ASCE Journal of Geotechnical & Geoenvironmental Engineering*, May, 690-696.

Simonelli, A.L., Penna, A. (2009).Performance-based design of gravity retaining walls under seismic actions. *Eurocode 8 Perspectives from the Italian Standpoint Workshop,* 277-289.

Simons JW, Bergan PG (1986). A finite element formulation of three-dimensional contact problems with slip and friction. *Computational Mechanics*, 1, 153-164.

Spacone E, Ciampi V, Filippou FC (1992). A beam element for seismic damage analysis. *Earthquake Engineering Research Center,* Rep. UCB/EERC92-07, University of Berkeley.

Stadler AT (1996). Dynamic Centrifuge Testing of Cantilever Retaining Walls, *PhD Thesis, University of Colorado at Boulder.*

Steedman RS, Zeng X (1990). The Seismic Response of Waterfront Retaining Walls, *Proc. Design and Performance of Earth Retaining Structures Conference*, Cornell University, Ithaca, NY.

Steedman RS, Zeng X (2000). Rotating Block Method for Seismic Displacement of Gravity Walls. *ASCE Journal of Geotechnical & Geoenv. Engineering.* . 126(8), 709717.

Taylor M, Kontoe S, Sarma S (2007). A review of performance based design procedures for gravity retaining structures under seismic loading. *Forth International Conference on Earthquake Geotechnical Engineering*, Paper no. 1520.

Veletsos AS, Younan AH (1994). Dynamic soil pressures on rigid retaining walls. *Earthquake Engineering & Structural Dynamics*, 23(3), 275-301.

Watanbe K, et al. (2003). Behaviors of several types of model retaining walls subjected to irregular excitation.*Soils and Foundations,* 43(5): 13-27.

Whitman RV, Liao S (1985). Seismic design of retaining walls, *Misc. Paper GL-85-1, US Army Engineer Waterways Experiment Station, Vicksburg, Mississippi.*

Wolf JP (1994). *Foundation Vibration Analysis using Simple Physical Models.* Prentice-Hall, Englewood Cliffs, NJ.

Wolf JP (1997). Spring-dashpot-mass models for foundation vibrations. *Earthquake Eng.* & *Structural Dynamics*, 26, 931-949.

Wood J (1973). Earthquake-induced soil pressure on structures, *Caltech Report EERL 73-05.*

Wood JH, Elms DG (1990) Seismic Design of Bridge Abutments and Retaining Walls, RRU Bulletin 84 Vol 2, *Bridge Design and Research Seminar,* New Zealand, Wellington NZ.

Wu Y, Prakash S (2001). Seismic displacement of rigid retaining walls—State of the Art. *Proceedings: Fourth International Conference on Recent Advances in Geotechnical Earthquake Engineering and Soil Dynamics and Symposium in Honor of Professor W.D. Liam Finn,* San Diego, California, USA.

Wu JJ, Li Y, Cheng QG, Wen H, Liang X (2016). A simplified method for determination of vertically loaded pile-soil interface parameters in layered soil based on FLAC3D. *Front. Struct. Civ. Eng.*, 10(1): 103-111.

Xu S-Y, Shamsabadi A, Taciroglu E (2015). Evaluation of active and passive seismic earth pressures considering internal friction and cohesion, *Soil Dynamics* & *Earthquake Engineering*, 70, 30-47.

Xue JF, Gavin K (2007). Simultaneous Determination of Critical Slip Surface and Reliability Index for Slopes. *ASCE J. Geotech. & Geoenv. Engrg.*, 133(7), 878-886.

Zarrabi K (1979). Sliding of Gravity Retaining Walls During Earthquakes Considering Vertical Acceleration and Changing Inclination of Failure Surface, *MS Thesis*, Massachusetts Institute of Technology, Boston, MA.

Zhang J, Qu H, Liao Y, Ma Y (2012). Seismic damage of earth structures of road engineering in the 2008 Wenchuan Earthquake, *Environmental Earth Sciences*, 65(4), 987-993.